UNDERSTANDING THE PAUL SCHERRER INSTITUTE'S PIM1 BEAMLINE FOR MUSE

By

ETHAN CLINE

A dissertation submitted to the

School of Graduate Studies

Rutgers, The State University of New Jersey

in partial fulfillment of the requirements

for the degree of

Doctor of Philosophy

Graduate Program in Physics and Astronomy

written under the direction of

Ronald Gilman

and approved by

_____

_____

_____

_____

_____

New Brunswick, New Jersey

October, 2019

ABSTRACT OF THE DISSERTATION

Understanding the Paul Scherrer Institute's PiM1 Beamline for MUSE

By ETHAN CLINE

Dissertation Director:

Ronald Gilman

In this thesis the proton radius puzzle will be described and used to motivated the MUSE experiment. An overview of the requirements for the systematic uncertainties for the experiment will then be presented, specifically the critically important understanding of the PiM1 magnetic channel. We will show that MUSE understands its systematic uncertainties well enough to have a competitive measurement of ep and μp elastic scattering. We will also show that the momentum of the μ's and π's can be measured to within 0.3% relative uncertainty for all MUSE momenta. By demonstrating our understanding of the source sizes and properties of the magnetic channel we also conclusively show that we understand the e momentum. The magnetic channel is simulated by two independent codes and it will be shown that MUSE understands how all particle types traverse the channel.

Acknowledgments

To my friends and family, thank you for your love and support. To my mentors, thank you for your never ending patience and understanding. This work would not have happened without all of you.

I would especially like to mention my adviser, Prof Ronald Gilman, for years of helpful advice and thoughtful discussions ranging from how to run an experiment to how to properly make coffee. Thank you for taking the time to help me grow and learn as a physicist and providing a welcoming environment in which I could succeed.

Of course much thanks goes to my colleagues on MUSE. Together we built an experiment of which we can all be proud. The experiences we had together, although sometimes stressful, are not something I would ever give up. Thanks especially to the Rutgers group.

Ievgen Lavrukhin, we have been here since the beginning, and it isn't quite over yet! While graduation seems like the end of an era our time on MUSE was some of the best I have ever had. Here's to late nights turning into early mornings in the counting room, too much coffee, and bad lasagna.

I also must thank all of my friends and fellow students at Rutgers, you've made my time here unforgettable in the best possible way. Thank you all for the laughs, advice, and adventures. To Daniel Brennan, Ian Laflotte, Caitlin Carpenter, Pouya Asadi, Conan Huang, and everyone else, your friendship has been invaluable. I would especially like to thank Dan for his scholarship.

I would like to thank my parents for teaching me to be inquisitive and push myself outside of my comfort zone. I never would have gotten this far without you. Thank you Mala for putting up with my brotherly antics, I cannot wait to see where your path leads you.

Finally to Andrea. You are my rock. Your kindness and patience has kept me grounded over the years. While the distance was long, I always looked forward to our time together in the sun. The future is bright and I am overjoyed to take this next journey with you.

Dedication

To my parents

Never let your sense of morals get in the way of doing what is right.

- Isaac Asimov, Foundation

Table of Contents

List of Tables

List of Figures

Chapter 1
Introduction

The study of fundamental quantities in nuclear physics has long been driven by particle accelerators. These large facilities accelerate a variety of sub-atomic particles up to large fractions of the speed of light and collide them into carefully constructed targets, allowing nuclear physicists access to the structure of the fundamental constituents of matter. In the decades since the construction of the first accelerator by Cockcroft and Walton [11, 12] the push for higher precision measurements has gained momentum, as the more precise results allow for a more fine-grained understanding of the structure being probed.

One of the particles of particular interest to the nuclear physics community is the proton, which along with the neutron, is a building block of the nucleus. The physical extent of the proton has been an area of study for decades. The first look into the internal structure of the proton was by Hoftsadter in 1956 [20], when the first measurement of the proton charge radius was performed. The *ep* elastic scattering cross section is related, in the one-photon exchange approximation, to the structure of the nucleon by

$$\frac{d\sigma}{d\Omega} = \frac{\alpha^2 \cot^2(\frac{\theta}{2})(1 + 2\tau \tan^2(\frac{\theta}{2}))}{Q^2(1+\tau)} \frac{E'}{E} [G_E^2(Q^2) + \frac{\tau}{\epsilon} G_M^2(Q^2)] \tag{1.1}$$

where $Q^2 = -4EE' \sin^2 \frac{\theta}{2}$ is the exchanged four-momentum, E and E' being the incident and scattered electron energy respectively, θ is the scattering angle. $\tau = \frac{Q^2}{4M^2}$ where M is the proton mass, and $\epsilon = [1 + 2(1+\tau)\tan^2(\frac{\theta_e}{2})]^{-1}$, which is called the virtual photon polarization. G_E and G_M are known as the Sachs electric and magnetic form factors respectively. In the standard non-relativistic textbook quantum mechanics derivation, the form factors are the Fourier transform of the charge and magnetic distribution of an infinitely massive charged particle in its rest frame. For a recoiling particle like the proton, the identification of electric and magnetic structure becomes obvious in the Breit frame. In the Breit frame the proton goes into the scattering vertex with momentum $\frac{\vec{q}}{2}$ and scatters with momentum $\frac{-\vec{q}}{2}$ and transfers no energy. The Breit frame is reached from the lab frame by boosting in the $\vec{q}$ direction; the transformation depends on scattering angle. In this frame a general proton form factor can be represented as

$$F(Q^2) = \int e^{-i\mathbf{qr}} \rho(r) d\tau. \tag{1.2}$$

Here $F(Q^2)$ is either G_E or G_M, $\mathbf{q} = -Q$, and $\rho(r)$ represents either a charge or magnetic distribution inside the proton. Making the assumption that **qr** is small, and recalling no energy is transferred in the Breit frame, it can be shown that $G_E(Q^2) = 1 + \frac{1}{6}\frac{q^2\langle r^2\rangle}{\hbar^2} + \ldots$ From this the proton charge radius $\langle r^2\rangle$ is defined as

$$\langle r^2\rangle \equiv -6\frac{dG_E(Q^2)}{dQ^2}\bigg|_{Q^2=0}. \tag{1.3}$$

The traditional method of extracting the radius is via elastic lepton-proton scattering, extracting the radius from the electric form factor as described above. Electrons bombard a liquid hydrogen target and the angle of scattering is measured in order to determine a cross section. From this cross section, the nucleon form factors can be extracted, allowing for a measurement of the proton radius. These experiments have been carried out over several decades and the CODATA average of such experiments is 0.8751(61) fm [35].

With the advent of high precision lasers it became possible to perform spectroscopic measurements of hydrogen. The spectral lines of hydrogen are perturbed by a variety of quantum effects, e.g. spin-orbit coupling, the relativistic energy correction effect, etc. In addition to these often discussed effects, there is a much smaller perturbation to the s-states caused by the finite size of the proton,

$$E(ns) \approx -\frac{R_\infty}{n^2} + \frac{L_{1S}}{n^3}, \tag{1.4}$$

where $E(ns)$ is the energy level, R_∞ is the Rydberg constant, n is the principal quantum number, and L_{1S} is the Lamb shift. It can be shown that $L_{1S} = (8172 + 1.56r_p^2)$ MHz. This finite-size effect perturbs only the S states as these are the only states of the hydrogen atom that have a non-zero wavefunction at the origin of the atomic system. States with higher angular momentum have a node at the origin and are not affected by the size of the proton.

By measuring the Lamb shift in atomic hydrogen the proton radius can be extracted. It is worth mentioning that spectroscopy measurements, in the framework of bound state QED, are measuring the electromagnetic form factors at $Q^2 \approx 10^{-4} - 10^{-5}$. This is 1 to 2 orders of magnitude lower in Q^2 than is accessible by scattering experiments. The values of the charge radius extracted via spectroscopy on average agree with the radius determined from scattering measurements.

While electron proton scattering and electronic hydrogen spectroscopy were the standard methods of measuring the radius for many years, higher precision experimental methods were investigated. The next choice would be to measure hydrogen spectroscopy with muonic atoms. Due to the unstable nature of muons it took several decades after the advent of hydrogen spectroscopy before such a measurement could be performed. If the proton to atom volume ratio is considered,

$$(\frac{r_p}{a_B})^3 = (\alpha m_r r_p)^3, \tag{1.5}$$

where a_B is the Bohr radius, m_r is the reduced mass of the system, and α is the fine structure constant, we see that the a heavy lepton orbits closer to the proton than a light lepton. This closer orbit leads to a larger perturbation to the energy levels, which have an energy shift given by [21]

$$\Delta E = \frac{2}{3}\pi\alpha|\Psi_S(0)|^2 r_p^2, \tag{1.6}$$

where $\Psi(0)$ is the lepton wave function evaluated at the origin of the atom. The heavier lepton, which orbits closer to the proton, has a larger wave function and therefore a larger and more easily measurable ΔE . This leads to the conclusion that using muonic spectroscopy can provide a more sensitive measurement of the proton charge radius.

In 2010 Randolf Pohl *et al.* [37] performed a measurement of the proton charge radius using muonic hydrogen spectroscopy. The result obtained, 0.841 84(67) fm, is 5.4σ from the accepted CODATA proton charge radius. This discrepancy between electronic and muonic measurements is known as the proton radius puzzle. The muonic hydrogen measurement was confirmed in 2013 by Antognini *et al.* [2]. The puzzle deepened with new *ep* scattering results of 0.879(8) [7] and 0.875(10) [49], along with two new electronic hydrogen spectroscopy measurements of 0.8335(95) [8] and 0.877(13) [14]. Possible explanations of the puzzle are wide ranging, some of the more compelling explanations are listed below. Comprehensive overviews by J. Krauth *et al.* and R. Pohl *et al.* go into detail on the state of the puzzle [26, 36]. Explanations broadly fall into three classes: potential beyond standard model physics, novel conventional physics, and experimental errors, which we discuss below.

There are many competing beyond-standard-model theoretical explanations of the puzzle. Generally, new physical models attempt to understand the radius puzzle using interactions between muons and protons. Electron scattering has been well studied for decades, so the phase space for new physics is severely constrained. There are also constraints in the muon sector as muons appear in particle decays, either as real or virtual particles, and some constraints due to muon scattering data, although the constraints are not as stringent as in the electron sector. Y. Liu and G. Miller propose a new electrophobic spin 0 force carrier, which is exchanged between a muon and proton [29, 28]. It is shown in their work that not only would this explain the proton radius puzzle but also the muon $g-2$ anomaly [5], while not introducing additional hyperfine interactions. Several other MeV mass force carriers, one by V. Barger *et al.* [3], and one by Tucker-Smith & Yavin [47] have been investigated. Barger *et al.* finds that spin 0, 1, and 2 are generally disfavored if the coupling between nucleons and mesons are universal. Although Barger does show that specific parity-violating muonic forces could explain the puzzle [4]. Tucker-Smith & Yavin claim that a new force carrier could explain the radius puzzle and the anomalous magnetic moment if the force carrier

couples differently between nucleons and mesons. If any of these particles exist and couple to muons but not electrons then they will be seen in the muon form factor at $Q^2 \approx M^2$. If the mass is large enough this effect would not be seen in spectroscopy measurements but could be seen in scattering measurements.

Now we turn to novel conventional physics. The two photon exchange, the largest uncertainty in [37], is also often cited as a possible explanation to the proton radius puzzle. In the Feynman picture of scattering, virtual photons are exchanged between charged particles. For $e^- p$ scattering the amplitude is proportional to $q_{proton} \times q_{electron} = -e^2$. For the two photon exchange this becomes $q^2_{proton} \times q^2_{electron} = e^4$ which has the opposite sign. In the case of $e^+ p$ scattering both diagrams have the same sign. As a result there is destructive (constructive) interference for electrons (positrons) making the cross section smaller (larger). Calculations and measurements of the two-photon effect do not have excellent agreement but generally say that the effect is small. The one and two photon diagrams can be seen in Fig. 1.1

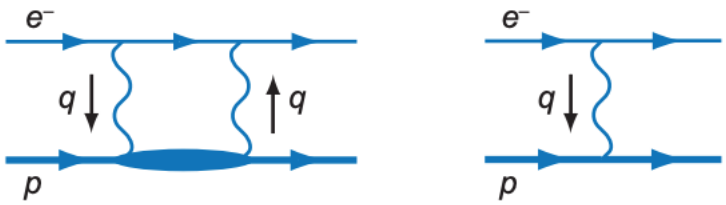

Figure 1.1: ***Left:*** A two photon exchange box diagram for $e^- p$ scattering. ***Right:*** One photon exchange diagram for $e^- p$ scattering [10].

Certain virtual photon exchanges are significantly more probable than others. These are known as "on shell" virtual particles, where $Q^2 = m^2$; the exchanged momentum is equal to the mass of the virtual particle. Due to the mass difference between the electron and muon, it is possible that some of these on shell exchanges are more likely for the muon. The largest uncertainty in the two-photon exchange calculation are intermediate hadronic states, where one photon is exchanged and excites the proton into an intermediate state which then decays via the emission of a second photon. As shown in [34] it is possible for the proton polarizability, which enters into the two-photon exchange, to be larger than predicted for muonic atoms and explain the puzzle. However such a calculation was ruled out soon after its inception, as it requires a Lamb shift of 4.8 meV in ^{4}He, much larger than is observed.

There are also potential issues in the electron scattering experiments. The proton radius is defined at $Q^2 = 0$, however it is not possible to measure scattering at that Q^2 by definition. Experiments

instead measure as low as possible in Q^2, while also including higher Q^2 data to not bias the fits. Truncating the range over which the radius is extracted can change the extracted radius value by an amount similar to the size of the puzzle [25]. The data then spans a range of Q^2 which can be fit with any number of models, but the fit must extrapolate past the end of the data to $Q^2 = 0$. Due to the inherently unstable nature of such fits and the variety of fitting functions, it is possible to fit the same data and extract different radii depending on your fitting function, as seen in [7, 27, 18]. Disagreement over which model to use is wide ranging and the community has not yet settled on the proper treatment for extracting the radius.

Currently there is no widely accepted explanation for the discrepancy between these two values of the radius. In order to shed light on the proton radius puzzle the MUon proton Scattering Experiment (MUSE) has been proposed [16]. There have been measurements of electronic and muonic hydrogen spectroscopy and electron proton scattering; however prior to MUSE there has been no measurement of μp scattering with precision sufficient to address the radius puzzle. MUSE aims to provide a simultaneous measurement of the proton charge radius via elastic electron proton and muon proton scattering [17].

A high precision muon proton scattering measurement could provide the cornerstone to understanding the radius puzzle as it exists today. The ability of MUSE to simultaneously measure electron proton and muon proton scattering allows for a precise determination of the *difference* between the charge radii extracted. Some systematic uncertainties cancel when measuring a ratio, or difference, of cross sections. MUSE therefore is uniquely suited to shed light on this puzzle by not only measuring the charge radius via electron and muon scattering, but any differences between the radii can be measured even more precisely than the individual radii [17].

Additionally, MUSE will measure alternately in both positive and negative polarities, thereby allowing direct measurement of two-photon effects at the sub-percent level. This is achieved by measuring at 3 separate momenta, 115, 155, and 210 MeV/c, and for both charge polarities. The two photon exchange is defined as the ratio of the difference of positive and negative cross sections divided by the sum of those cross sections.

Fig. 1.2 provides a demonstration of the minimum required sensitivity of the experiment. The left panel shows that the cross section anticipated for the 0.88 fm radius falls 6% faster than the anticipate cross section of the 0.84 fm radius over the MUSE kinematic range. As a result, for a 5σ measurement of the radius, MUSE needs total cross section uncertainties on the order of 1%. The right panel shows parameterizations of $G_E^p(Q^2)$ compared to the Mainz data [7], extracted from cross sections with both spline and polynomial fit functions, and plotted relative to a linear fit function with a radius fixed at 0.842 fm. The Mainz data points at the lowest Q^2 are consistent with a larger

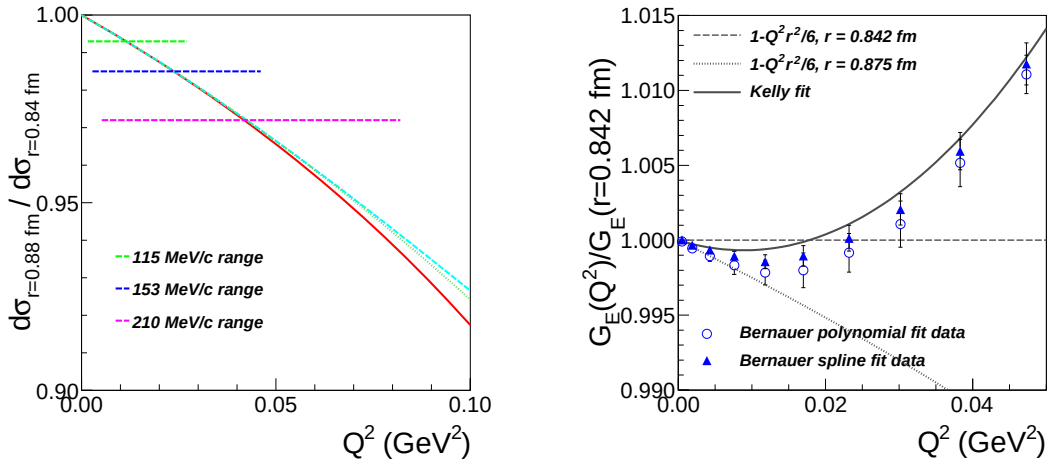

Figure 1.2: ***Left***: Effect on the cross section from the proton radius being 0.88 fm vs. 0.84 fm. The solid red line uses a linear approximation, $G_E = 1 - Q^2 r^2/6$. The cyan dashed and green dotted curves include Q^4 and Q^6 terms taken from the Kelly parameterization, respectively. The horizontal green, blue, and magenta dashed lines indicate the kinematic range of the proposed MUSE data. ***Right***: The Kelly parameterization and a linear fit assuming the radius determined by ep measurements, all relative to expectations from a linear fit using the radius determined from μp atoms [17].

radius but nonlinearities appear in the data below $Q^2 = 0.02$, which emphasizes the fact that high precision, low Q^2 measurements are necessary to precisely extract the radius. That measurement must also cover a large range of Q^2 in order to be sensitive to higher order terms. This panel also shows that a linear description of G_E^p is *not* sufficient to extract the radius. MUSE has access to a Q^2 range of $\approx 0.0016 - 0.08$ GeV^2, with slight differences for muons and electrons due to their mass.

MUSE will measure an elastic scattering cross section, experimentally determined by

$$\frac{d\sigma}{d\Omega} = \frac{N_{counts}}{N_{beam} \times (x\rho)_{target} \times \Delta\Omega \times \epsilon} \tag{1.7}$$

where N_{counts} is the number of elastic events counted, N_{beam} is the number of beam particles, $(x\rho)_{target}$ is the area density of the target, $\Delta\Omega$ is the solid angle covered by the detectors, and ϵ is the total efficiency accounting for detector, geometric efficiency, DAQ, electronic, and radiative correction effects. The difficulty in high precision electromagnetic scattering is that the cross section vary sharply with Q^2 and energy, due to kinematic factors in the cross section. Experimental background and radiative corrections vary strongly with scattering angle. Small offsets can warp the shape of the angular distribution and cause large errors when extracting the radius. Many of

these difficulties have been studied in the community extensively for several decades [40, 43].

In the PiM1 target area the beam has a large physical extent, so MUSE requires high precision vertex reconstruction for its angle determination. Precise time of flight (TOF) is required for beam particle and reaction identification. As a result, the decision was made to measure each incoming beam particle in every event. Typical ep scattering measurements do not measure the incoming beam, as most beams at electron accelerators are highly focused with almost no dispersion. This added difficulty comes as an intrinsic part of the secondary PiM1 beam line, but the benefit of such a beam is that it provides e's and μ's simultaneously and allows easy access to both charge states. When measuring a relative difference between ep and μp scattering, having both particle species in the beam allows for the cancellation of many uncertainties, as seen in Table 1.1. Any uncertainty that is the same for both electrons and muons will cancel in a ratio of their cross sections. The solid angle covered by the scattering chambers is the same for both species to leading order. The uncertainty in how well we measure the solid angle then drops out of the ratio of cross sections. However an uncertainty that is independent for each particle type, like the momentum determination, does not cancel when comparing the ratio of cross sections.

In order to perform a high precision measurement, MUSE must have control over its systematic and statistical errors. To provide statistical uncertainties of less than 0.1% MUSE has suggested a comprehensive data taking program of two 6-month beam times, one beam time per year, in order to assure full coverage of all momenta and charge polarities. An estimate of systematic uncertainties is also provided [17] and tabulated in Table 1.1. From this table it is clear that many systematic uncertainties become small when comparing relative cross sections, however some uncertainties remain. The detector inefficiencies are minimized geometrically as much as possible during design and construction, but some inefficiencies due to electronic dead time and hardware thresholds remain. Muons and pions may decay in flight and be misidentified in our analysis. In order to minimize the uncertainty in particle identification a variety of machine learning techniques can be employed to properly identify scattered particle type.

It is also worth noting that the radiative corrections for electrons, although large, have only small theoretical uncertainties in the well established theoretical approaches used in the field [46, 31]. The limitation here is intrinsic to the MUSE energy scales, and detector resolution. The radiative corrections, and two-photon-exchange corrections are an area of active research, as elastic μp scattering has not been attempted at this level of precision [24, 44].

The final persistent systematic uncertainty is the beam momentum, which must be known to 0.2% for muons and $0.3\% - 0.8\%$ for electrons in order to achieve a contribution of 0.1% (0.05%) to the total relative uncertainty on the cross section (G_E^p) [17]. The energy loss due to particles passing

Uncertainty	angular distribution (%)	μ/e (%)	$+/-$ (%)
Detector efficiencies	0.1	0.1	0.1
Solid angle	0.1	small	small
Luminosity	small	small	small
Scattering angle offset	0.2	small	small
Multiple scattering correction	0.15	small	small
Beam momentum offset	0.1	0.1	0.1
Radiative correction	0.1 (μ), 0.5 (e)	0.5	1γ small
Magnetic contribution	0.15	small	small
Subtraction of μ decay from μp	0.1	0.1	small
Subtraction of target walls	0.3	small	small
Subtraction of pion-induced events	small	small	small
Beam PID / reaction misidentification	0.1	0.1	0.1
Subtraction of μ decay from ep	small	small	small
Subtraction of ee from ep	small	small	small
TOTAL	0.5 (μ), 0.7 (e)	0.5	0.2

Table 1.1: Estimated MUSE relative systematic cross section uncertainties for the shape of angular distributions, the ratio of muon and electron scattering cross sections, and the ratio of + charge to − charge cross sections.

through material in the beam line contributes to our uncertainty in the momentum extraction. The full simulation of MUSE will include energy loss measurements to extract the momentum to the precision necessary for the experiment. It is clear that the cross section shown in 1.1 varies with beam momentum. Any offset in momentum can lead to warping the angular distribution of the cross section. Offsets in beam momentum can offset Q^2 and lead to the form factor being determined at the wrong Q^2. Figure 1.3 shows the effect on the cross section of momentum offsets, and of averaging over the beam momentum acceptance [17]. We will renormalize our data so the angle to angle variation in the figure is the important quantity.

The focus of this work will be the understanding of the PiM1 magnetic channel, in particular to demonstrate MUSE can measure the momentum to the precision necessary to produce a competitive measurement of the charge radius.

Measuring the TOF of each particle species allows for a high precision momentum measurement,

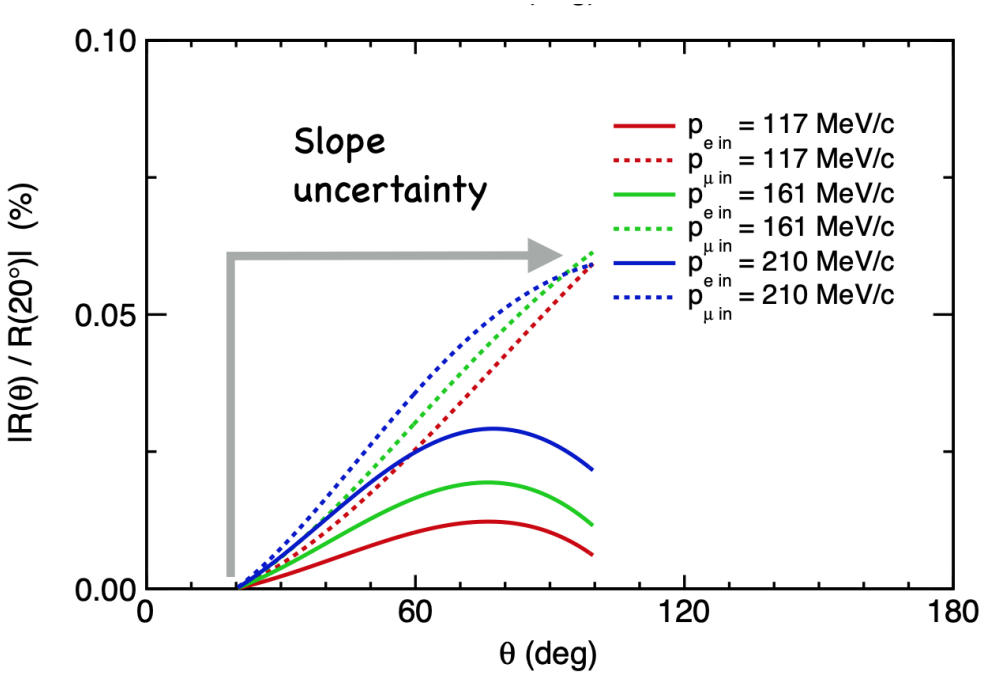

Figure 1.3: Change in cross section in percent for a 0.1% change in the beam momentum over the MUSE angle range. Using the Kelly form factor parameterization [22]. Courtesy of Steffen Strauch.

indeed this is a traditional method of measuring momentum, as the relation between momentum and time can be derived easily. For a given particle the TOF is:

$$\Delta t = \Delta L \sqrt{1 + \frac{m^2}{p^2}} \tag{1.8}$$

where Δt is the time elapsed, ΔL is the distance traveled, m is the mass, and p is the momentum. Here we use units where $c = 1$. TOF measurements cannot be used to determine electron momentum; at all three MUSE moment settings the electrons have a velocity indistinguishable from that of light, or in the context of Eq. 1.8 electrons have $m/p \simeq 0$ for MUSE detectors. As a result, the electron momentum can only be measured by its trajectory through magnetic fields, especially if in comparison to other particles of known momentum. Comprehensively studying the magnetic channel will allow us to determine the beam properties of all particles in the beam line. As magnetic channels select on particle momentum, a detailed understanding of the channel physics provides an understanding of the relative momentum of particles in the beam.

We will show that carefully modeling the production source of all of our beam particles is crucial for understanding the properties of the magnetic channel. It will be demonstrated that the difference in source production mechanism does not matter in order to make the claim that e's have the same momentum as other beam particles. By performing a simulation of the entire PiM1 beam line

and comparing it to experimental data then it can be shown that the beam line is well understood. Our simulations can tell us correlations between position, angle and momentum of beam particles, including dispersion along the beam line. This information is particularly important for determining beam properties and claiming MUSE understands PiM1 well enough to run a high precision measurement.

We will show later the measured and simulated effects of the magnets on the beam, and how the beam line can be used as a spectrometer to determine particle momenta. Using the beam as a spectrometer to extract the relative electron momentum is a key measurement that MUSE must make if it is to measure any interesting physics using ep scattering.

The beam flux in PiM1 is shown in 1.2 and Fig. 1.4. Unfortunately it can been seen that muons have a very small flux at all momenta, which increases the difficulty of obtaining a statistically significant measurement. PiM1 has a relatively low flux of electrons and muons as it was originally constructed as a pion beam line. Muons have a larger source size and consequently a wider momentum distribution and a lower acceptance than the pions. Similarly electrons have slightly different source physics than the pions and their acceptance is reduced.

Momentum (MeV/c)	Polarity	Total Flux (MHz)	e Flux (MHz)	μ Flux (MHz)	π Flux (MHz)
115	+	8.3	8.05 (3.20)	0.17 (0.07)	0.08 (0.02)
153	+	16.9	10.65 (2.08)	2.03 (0.40)	4.23 (0.83)
210	+	79.2	9.50 (0.40)	6.34 (0.26)	63.36 (2.64)
115	−	7.4	7.29 (3.25)	0.07 (0.03)	0.04 (0.02)
153	−	11.9	10.71 (2.97)	0.38 (0.11)	0.81 (0.22)
210	−	24.0	11.28 (1.55)	0.96 (0.13)	11.76 (1.62)

Table 1.2: Beam flux at the target for full PiM1 channel acceptance with 2.2 mA primary proton current. The total flux is based on previous measurements, while the relative fluxes of each particle types are based on MUSE measurements. Also shown in parentheses is the flux of each particle type when the combined flux is limited to the MUSE planned total flux of 3.3 MHz.

The properties of the PiM1 beam line will discussed at length and it will be demonstrated that MUSE understands the momentum and spatial distributions of the e's and μ's. MUSE has extracted the momentum to within the required uncertainty for the experiment to make a measurement of the precision necessary to address the proton radius puzzle.

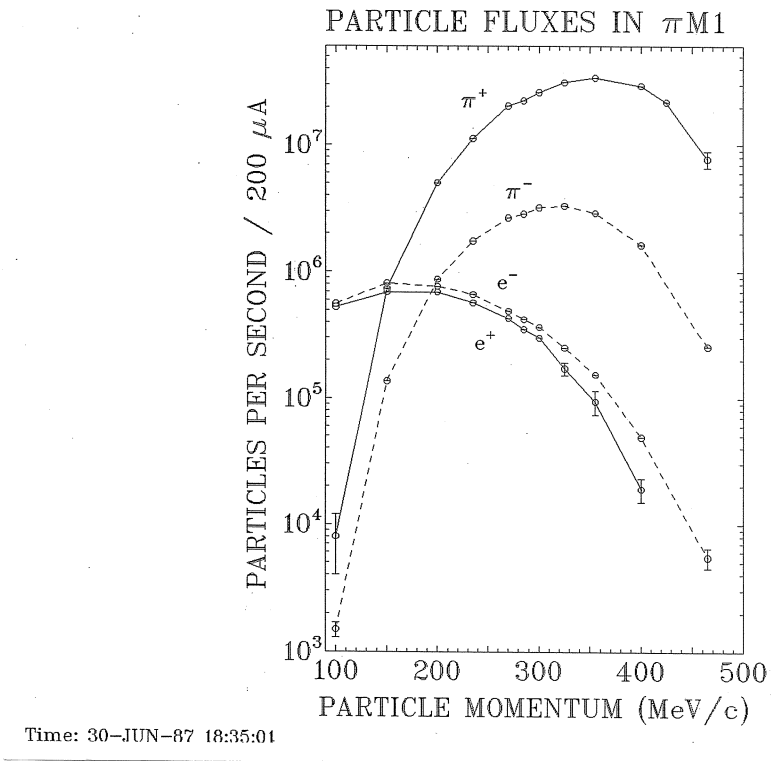

Figure 1.4: The absolute flux of π and e at both charge polarities plotted against momentum. [42]

Chapter 2 will describe in detail the magnetic elements of PiM1. The production target construction and properties of the M secondary production target will be reviewed as well.

Chapter 3 will discuss the experimental setup of the PiM1 area used to measure the properties of the PiM1 beam line. The measurement procedures will also be documented here.

Chapter 4 provides an overview of the simulation efforts using TURTLE, and the improvements over the existing codebase. It also details the G4beamline simulation and its relation to Geant4, and how it was modified to accurately represent the PiM1 beam line. The simulation results will be presented.

Chapter 5 discuss the analysis procedures for the data taken, and compares simulation and data.

Chapter 6 will provide an interpretation for the results presented and discuss the future use of the PiM1 beam and MUSE.

Chapter 2
The PiM1 Channel

MUSE takes place in the PiM1 experimental area of the Paul Scherrer Institute (PSI). The PiM1 beam is a secondary beam line at PSI High Intensity Proton Accelerator (HIPA) [13]. This high resolution pion beam line with momentum range of 100 to 500 MeV/c can achieve a momentum resolution of 0.1%, which in principle is sufficient for MUSE. The PiM1 beam line observes the point at which the primary HIPA beam crosses the carbon "M target", at an angle of 22° to the proton beam, as seen in Fig. 2.1.

The beam line was originally designed for a pion beam, with pions being generated by the $pC \rightarrow \pi X$ reaction. Historically, several pion factories were constructed in the 1970s to explore pion-nucleon interactions, to better understand the nuclear force and nuclear properties. At the same time, QCD as the theory of the strong interaction was being developed, but it would take some time before effective field theories based on QCD were applied to pion-nucleon interactions and the nuclear force. Two cyclotrons were developed at Triumf and PSI, and a linear accelerator at Los Alamos. These accelerators were all designed primarily to provide high π flux beam lines in order to provide a more fundamental understanding of the strong force over a range of energies. As pions scatter off targets via the strong interaction, electron and muon contamination of the beams and scattering interactions via electromagnetic scattering was generally a minor issue for scattering measurements, and could be suppressed by a variety of techniques. Furthermore, the pion beam lines were generally unsuitable for muon studies due to an overwhelming pion background, so the properties of the background muons and electrons in pion beam lines were generally not well established.

MUSE, however, is not intended to measure a π cross section. The MUSE experiment uses the decay products of the π's generated by the primary proton beam, namely, the μ's and e's, which are created by charged and neutral pion decay. While the known specifications of the pion beam satisfy MUSE experimental requirements, it is necessary to verify, both in principle and in practice, that the requirements are also met for beams of μ's and e's. It must be demonstrated that the beam spots and beam momenta, and beam line resolution, match the experimental requirements. The size of the beam spot in position and angle can be determined directly by position sensitive

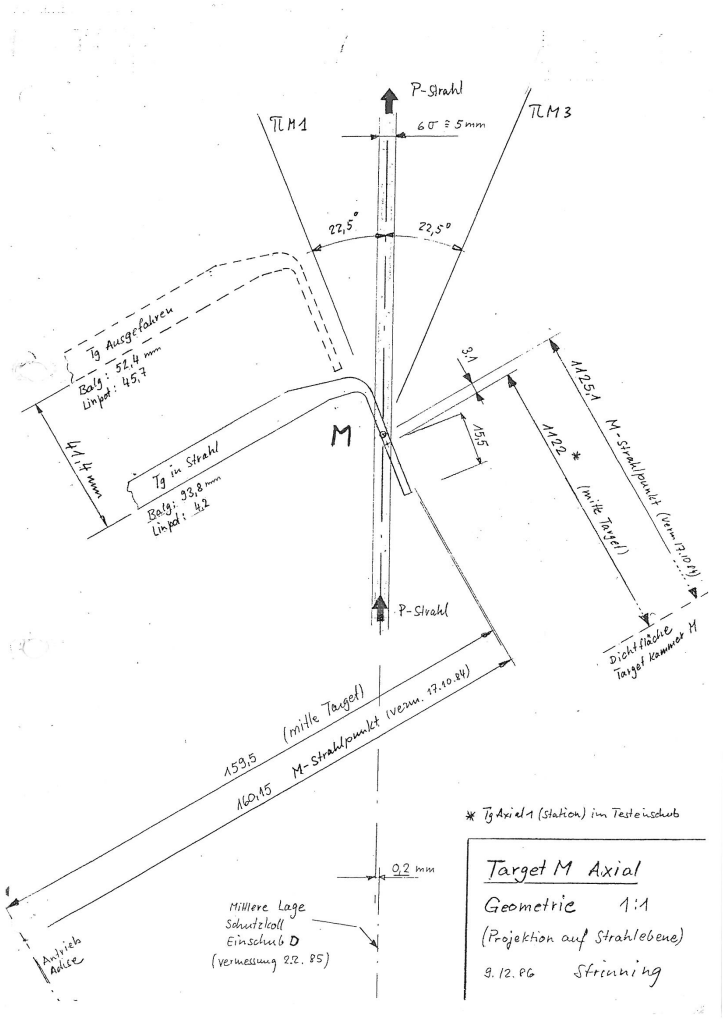

Figure 2.1: M Target Geometry, PiM1 production location. The primary proton beam points in the direction of the arrow labeled "P-Strahl". The angled arm labeled "M" is the carbon production target.

detectors, along with precise timing detectors that allow selection of particle type. Determining the beam momentum and its resolution is a much more difficult task.

The PiM1 beam line also provides an Intermediate Focal Point (IFP) where the properties of the beam can be measured before the beam enters the final dipole. The IFP is a 1 meter long section of the beam line that is open to air. A copper collimator at the IFP is used to select a user-specified momentum bite of the beam. On either end of the IFP there are vacuum entrance windows that the beam must pass through to enter and exit the IFP. The location of the IFP and the magnetic elements of PiM1 can be seen in Fig. 2.2. The magnetic channel is set up so that the 7cm/% dispersion is measurable at the IFP, as will be discussed in the next chapter.

The combination of measurements at the PiM1 target and IFP, compared with simulations of the PiM1 channel, provide the best insights and strongest constraints on the source distributions and properties of the e's, μ's, and pi's that make up the beam. The source distributions are of particular interest since, to the extent that they are the same, the resulting beam properties must also be the same. Differences between the sources must be modeled and understood. The source distributions can be modeled in simulation using standard Geant4 and ROOT physics packages, as the $pC \to \pi X$ reaction is moderately well understood, and pion decays are very well understood.

2.1 The Primary HIPA Beam Line

The primary beam line at PSI is a 590 MeV proton beam provided by HIPA. This proton beam is pulsed at an RF frequency of 50.6 MHz; every 19.75 ns a proton bunch is produced by the accelerator and passes down the beam line. An overview of the primary beam line is in Fig. 2.3. The HIPA is capable of providing up to 2.2 mA of proton current. The beam is accelerated in several stages. First a Cockcroft-Walton electrostatic column is used to produce protons at 870 keV/c. The protons are then passed to the Injector 2 cyclotron. The Injector 2 is a 4 stage cyclotron which brings the protons up to 72 MeV/c and then feeds the protons to HIPA. HIPA is an 8 stage cyclotron with an operational momentum of 590 MeV. From here the beam is transported to the primary beam line and on to the M target.

PSI constructed HIPA and the M target to provide high π flux to two beam lines, PiM1 and PiM3. However much of the proton beam passes through the M target and continues to the E target where several more secondary beam lines, PiE1, PiE3, and PiE5 were constructed to provide π beams, and later MuE1 and MuE4 were designed to provide μ beams for surface μ production studies, muonic spectroscopy, and tests of the standard model. Finally the HIPA beam encounters the beam dump which serves as a spallation source for a neutron beam. Every 330 seconds, the main proton beam is diverted for an 8 s cycle to the ultra cold neutron source, to provide a source of neutrons for lifetime and electric dipole moment studies.

2.2 The M Target

The M target is a rotating graphite wheel positioned such that protons transit a flange aligned to the PiM1 beam line at an angle of 22 degrees. The π production cross sections on carbon as a function of kinetic energy can be seen in Fig. 2.4 for two lab angles.

From the primary proton energy of 590 MeV, pions of the momenta of interest to MUSE are generated with a kinetic energy between ~ 40 and ~ 112 MeV. For the production of muons that

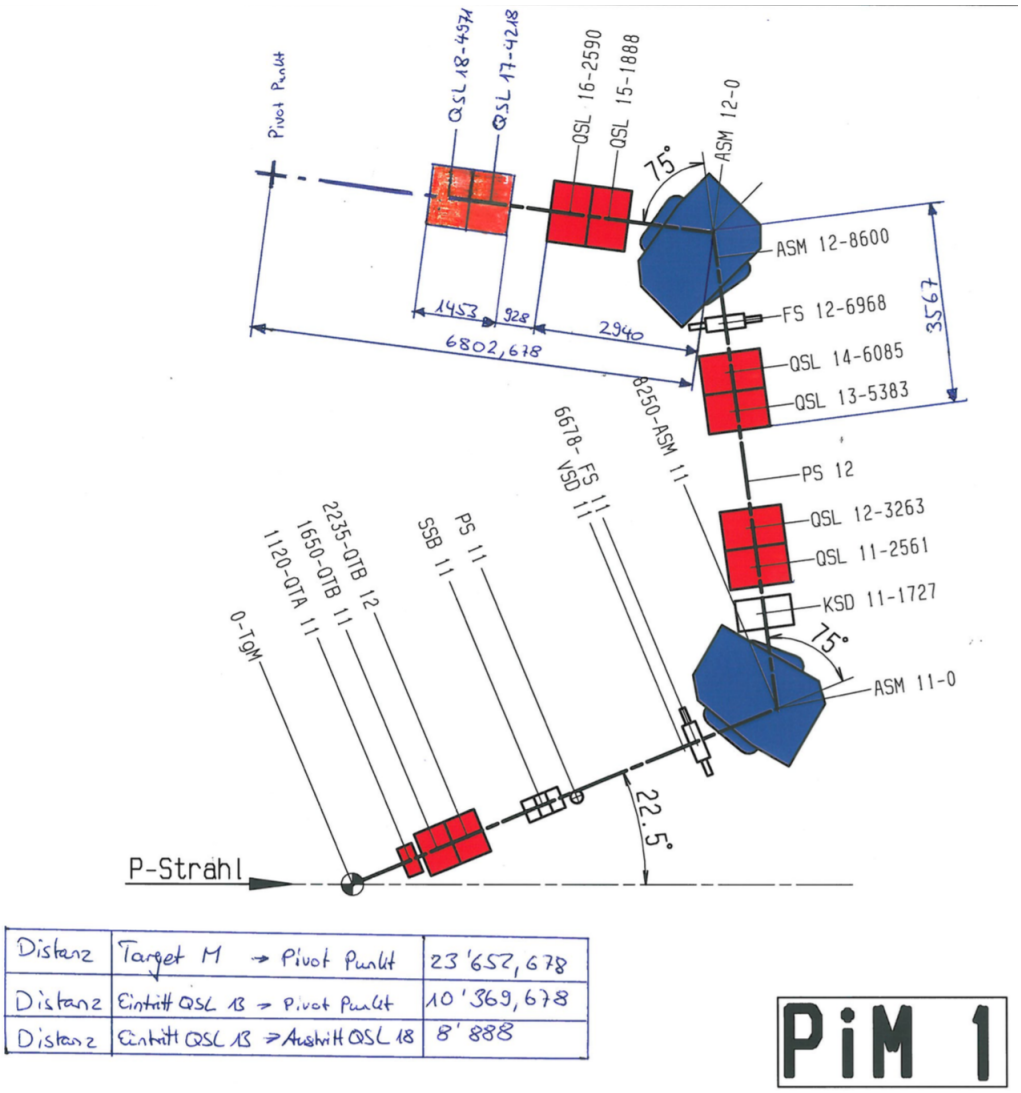

Figure 2.2: Elements of the PiM1 channel with the IFP labeled as "PS 12". The primary proton beam is represented by the arrow labeled "P-Strahl". The final focus of the PiM1 beam line is represented by the cross labeled "Pivot Punkt". In this figure, blue magnets are bending dipoles and red magnets are focusing quadrupoles. "FS 11" and "FS 12" are jaws for controlling beam flux. "KSD 11" is a plug to stop the beam to provide safe access to the hall. "SSB 11" is a steering magnet to raise the beam in y. The numbers prepended to the magnet distances are straight line distances measured relative to each bend in the beam line. They do not take into account curves through the magnets.

go into PiM1, we are interested in pions that decay within ~ 20 degrees of the PiM1 channel for the lowest MUSE momentum and within ~ 10 degrees for the highest momentum. It will be shown that this is the appropriate kinematic range in Sec. 4.1. From Fig. 2.4 we see the pion production

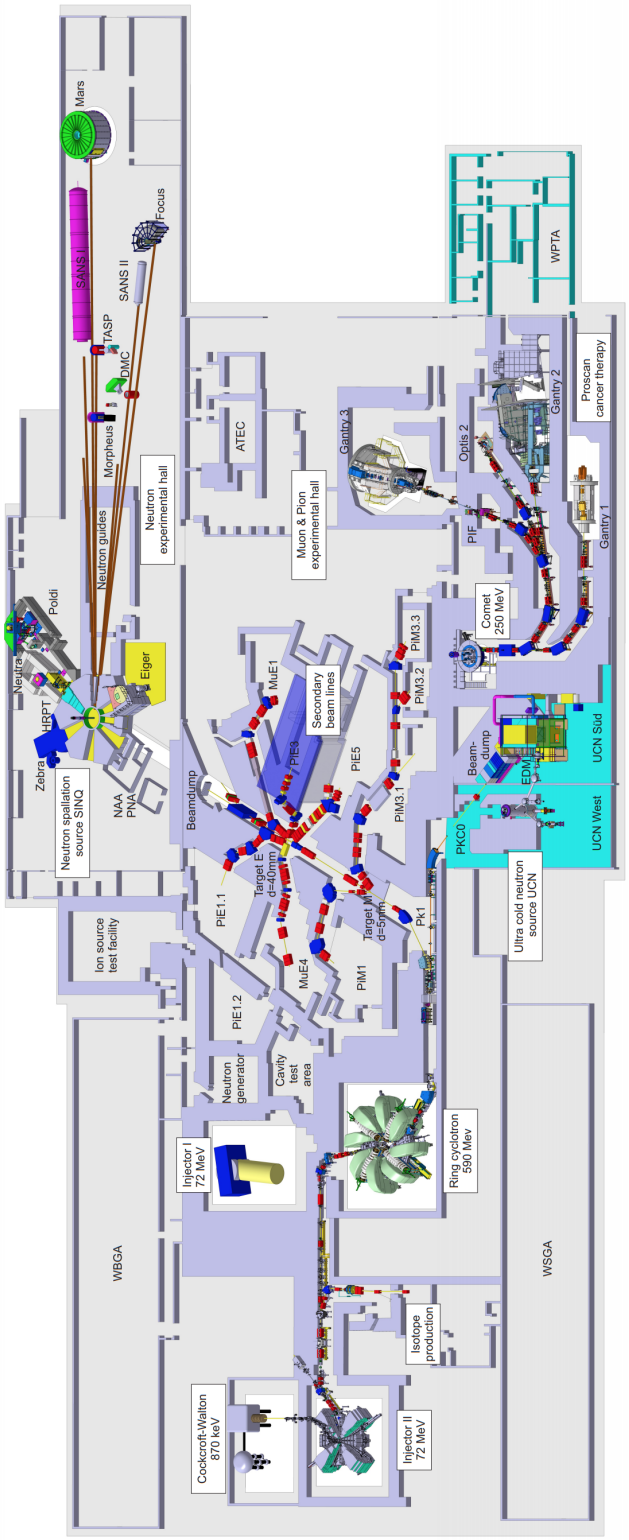

Figure 2.3: A schematic overview of the HIPA beam line at PSI.

cross section only weakly depends on kinetic energy and angle, for pions in the energy and angle ranges to generate muons in PiM1 in our momentum range [23]. We assume this trend continues to 0 degrees. The same is generally true for π^- except the magnitude of the production cross section is $4-5$ times smaller [6].

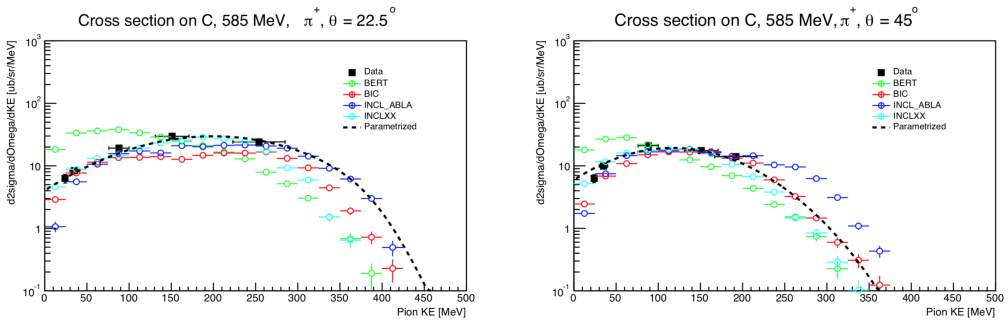

Figure 2.4: Positive pion production for p^+C. The two plots show that the π production cross section is relatively independent of kinetic energy, until the highest and lowest allowed energies [23].

As mentioned in Chap. 1, e's, μ's, and π's are produced through several mechanisms. The pions in the beam line are produced via direct strong interactions $pC \to \pi X$ in the target wheel, where X can can include excited nucleon or nuclear states as well as states in which the C has been broken up into smaller nuclei. The size of the pion source is therefore of the same size as the proton beam spot, a full width of 2 mm horizontal, a 2σ vertical width of 2.9 mm, and a 6σ z width of 13 mm [13]. The properties of the M target are shown in Table 2.1.

Electrons come from two types of pion decays, the first (and largest branching ratio, $\approx 98.8\%$) is from $\pi^0 \to \gamma\gamma$, followed by a γ converting in the target carbon, $\gamma C \to e^+e^-X$. The second source of electrons is from the Dalitz decay $\pi^0 \to e^+e^-\gamma$, $\approx 1.2\%$. A good first approximation, validated by simulation, is that the electron source size is the same size as the pion source, this will be expanded upon further in Sec. 4.1.

The muons come from charged pion decays, $\pi^\pm \to \mu^\pm\nu_\mu$. Here the ν is either a ν_μ or $\bar{\nu}_\mu$ depending on the charge of the pion. This source is decidedly not point-like, as the charged π does not have to decay within the M target. This decay is mediated by the weak interaction which accounts for the longer charged pion half life.

The source size differences will be investigated further in Section 4.1. Differences in source sizes can manifest as differences in beam spots and beam momenta, and must be well understood for a high precision measurement.

M Target Property	Value
Mean Diameter	320 mm
Target Thickness	5.2 mm
Target Width	20 mm
Graphite Density	1.9 g/cm^3
Beam Loss	1.6%
Power Deposition	2.4 kW/mA
Operating Temperature	1100 k
Irradiation Damage Rate	0.12 dpa/Ah
Rotation Speed	60 rpm

Table 2.1: Properties of the M target [19].

2.3 The Magnetic Channel

The PiM1 channel is a secondary channel designed to provide high-momentum resolution π beams. The magnetic elements were shown in Fig. 2.2. The channel bends the beam horizontally, so the standard transport coordinates have $+z$ along the beam line, $+x$ to beam right, and $+y$ is vertically downward. Typically we label angles that particles make with the beam axis as x' and y'. Referring to the elements along the path of the beam we start at the production target M, and then have the red quadrupoles QTA 1 and QTB 1 which focus in y and defocus in x. QTB 2 then focuses in the orthogonal direction. SSB 11 is a "kicker" magnet which shifts the beam in y and feeds into the FS 11 jaws which control the beam flux. Then ASM 11, the first dipole in blue is used for momentum selection. ASM 11 has a central bend angle of 75° and together with QTA 11 and 12, produces the 7cm/% dispersion that can be observed at the IFP. QSL 13 and QSL 14 along with ASM 12 are set to oppose the dispersion at the IFP such that the resulting magnification at the PiM1 target is about 1 with a 1 cm/% dispersion. Finally the QSL 15, 16 and QSL 17, 18 quad pairs provide the focusing for the PiM1 target. The overall channel properties can be found in Table 2.2. A transport diagram detailing the focusing of the beam as it traverses the channel is shown in Fig. 2.5. In the transport diagram the vertical line in the center represents the z axis, and the black line to the right shows the 2σ beam distribution in x and the black line to the left shows the 2σ beam distribution in y. The red lines are the quadrupoles and the light blue lines are the bending dipoles. The faint green line near the middle of the diagram is the dispersion present at the IFP, 7 cm/% in the x direction. The IFP has a full width of 21 cm, leading to a total momentum acceptance of ±1.5%.

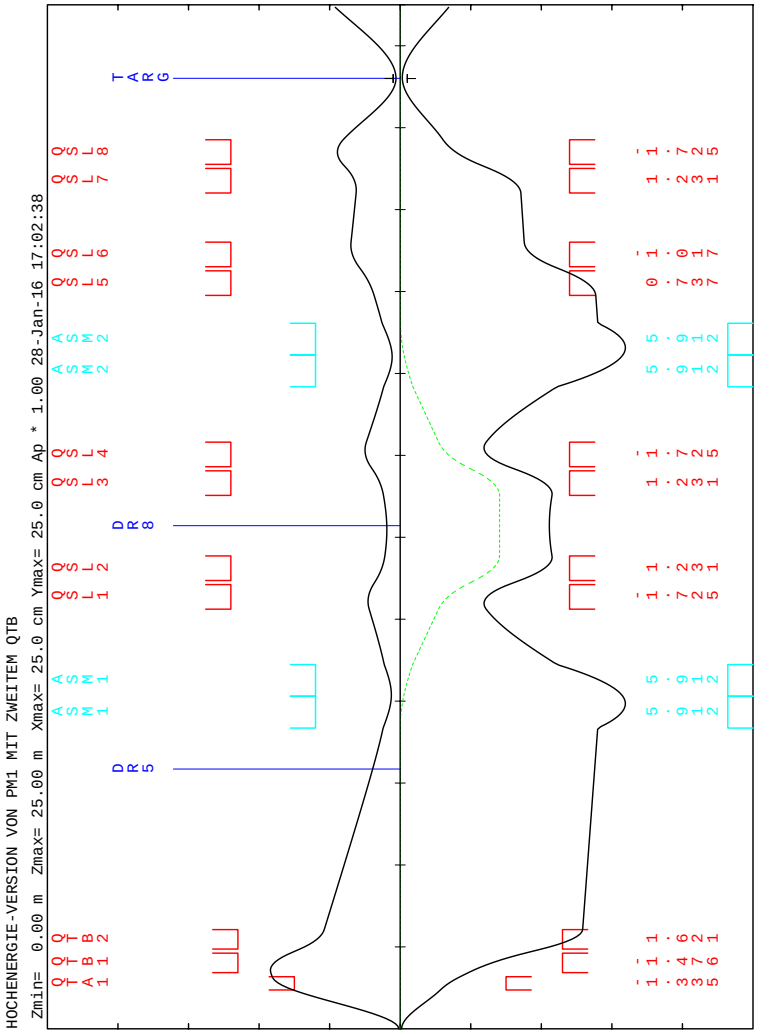

Figure 2.5: A transport diagram of the PiM1 channel. The red open rectangles represent the quadrupoles, and the teal open rectangles represent the dipoles. In the diagram "DR8" is the IFP and "TARG" is the PiM1 target. "DR5" represents the position of the FS-11 jaws. The bottom of the figure shows the M target location. The two black lines show the 2σ beam envelope, the right line is the extent of the beam in the x coordinate and the left line is the extent of the beam in y and the green line near the IFP shows the total dispersion of the beam.

2.3.1 Channel Acceptance

The magnetic channel has a limited acceptance; while beam particles are produced with a continuous spectrum of angles and energies, only the particles pointing in the direction of the channel and in

PiM1 Channel Property	Value
Total Path Length	23.12 m
Momentum Range	$100 - 500$ MeV/c
Solid Angle	6 msr
Momentum Acceptance (FWHM)	3%
Momentum Resolution	0.1%
Dispersion at Focal Plane	7 cm/%
Spot Size on Target (FWHM)	15 mm horizontal by 10 mm vertical
Angular Divergence on Target(FWHM)	35 mrad horizontal by 75 mrad vertical

Table 2.2: PiM1 channel values from [13]. The difference between the path length listed here and the source comes from more accurate survey distances that are shown in fig. 2.2

the momentum range selected by the magnets are accepted. To demonstrate the acceptance of the channel we show the distributions that enter the QTA1 magnet, as calculated by our TURTLE simulation. We will describe all of our simulations in more detail in Chap. 4. A description of the particles entering the beam line, at the front face of QTA1, can be seen in Fig. 2.6. The ± 4 cm wide x distribution is narrower than the ± 9 cm wide y distribution, reflecting the fact that the initial beam line quadrupoles focus in the y direction and defocus in the x distribution. The x distribution width also allows the momentum range that enters the channel to expand from $\pm 1.5\%$ to $\pm 2\%$. The correlations between these particles is shown in Fig. 2.7. These figures are produced by our simulation package, which will be discussed in Sec. 4.2, and require that any particle passing down the beam line passes through the position-sensitive Gas Electron Multiplier (GEM) chambers, located about 30 cm upstream of the PiM1 target. By requiring that the particles pass through the GEMs we are able to compare our simulations to data. The GEMs, and experimental setup, will be discussed in Sec. 3.1.1.

Fig. 2.7 shows how the parameters of the particles that traverse the channel are correlated at the entrance face of QTA1, we label the x, y coordinates and x', y' angles at the QTA1 magnet as x_{QTA}, y_{QTA}, x'_{QTA}, and y'_{QTA}. The top right panel shows the strong, narrow correlation in y'_{QTA} vs. y_{QTA}. As there are no magnetic elements between the source and QTA, and since the acceptance of QTA1 is ± 8 cm, there must be a strong $y'_{QTA} = y'_{prod}$ vs. y_{QTA} correlation for particles to reach large y_{QTA}. The limited acceptance in y_{prod} severely constrains the production of muons and electrons that make it through PiM1.

The correlation for x'_{QTA} vs. x_{QTA} is shown in the top left panel of Fig. 2.7. As x_{QTA} gets more positive, for example, the angle x'_{QTA} becomes more negative otherwise the defocusing of the quad would bend the particle into the side of the quad. The distribution is broadened by the range of momentum.

The momentum correlations are shown in the middle and bottom row panels of Fig. 2.7. We see a tilt of the distribution of δ vs. x_{QTA}, and some correlation of δ with x'_{QTA}. There is again no significant correlation of the momentum with y_{QTA} or y'_{QTA}.

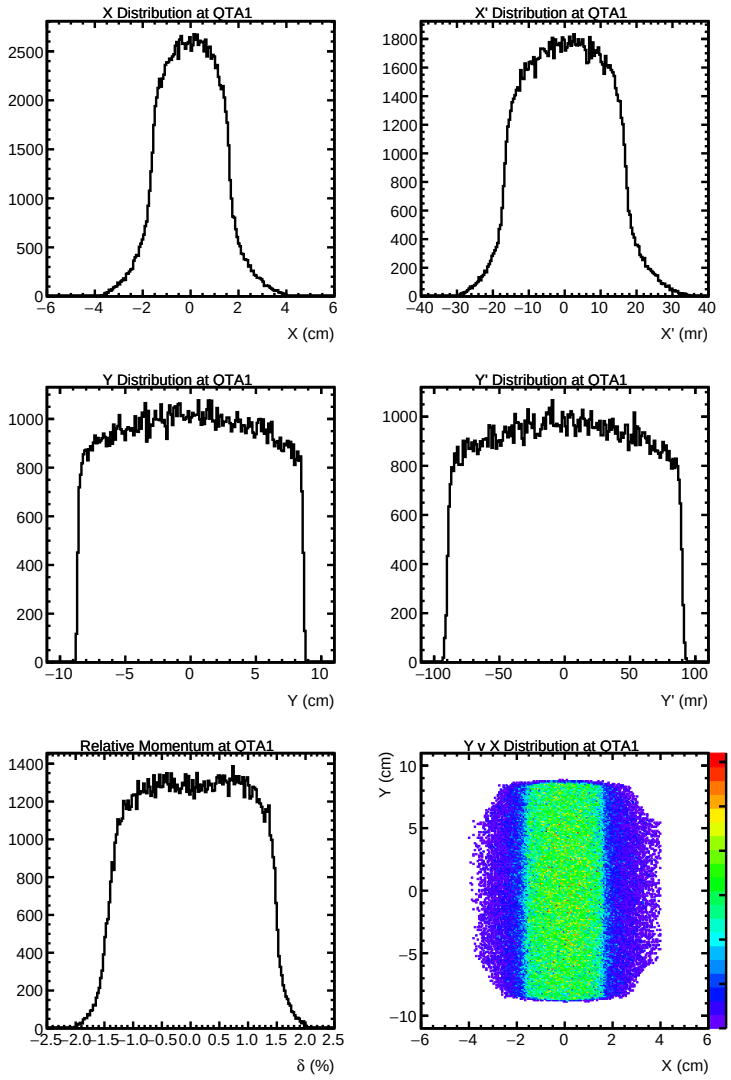

Figure 2.6: Distributions of particles at the QTA1 entrance that reach the GEM chambers after the PiM1 channel. ***Upper left***: position distribution in x. ***Upper right***: x', the angular distribution in x. ***Center left***: position distribution in y. ***Center right***: y', the angular distribution in y. ***Lower left***: momentum distribution δ in % from nominal momemtum. ***Lower right***: position distribution y vs x.

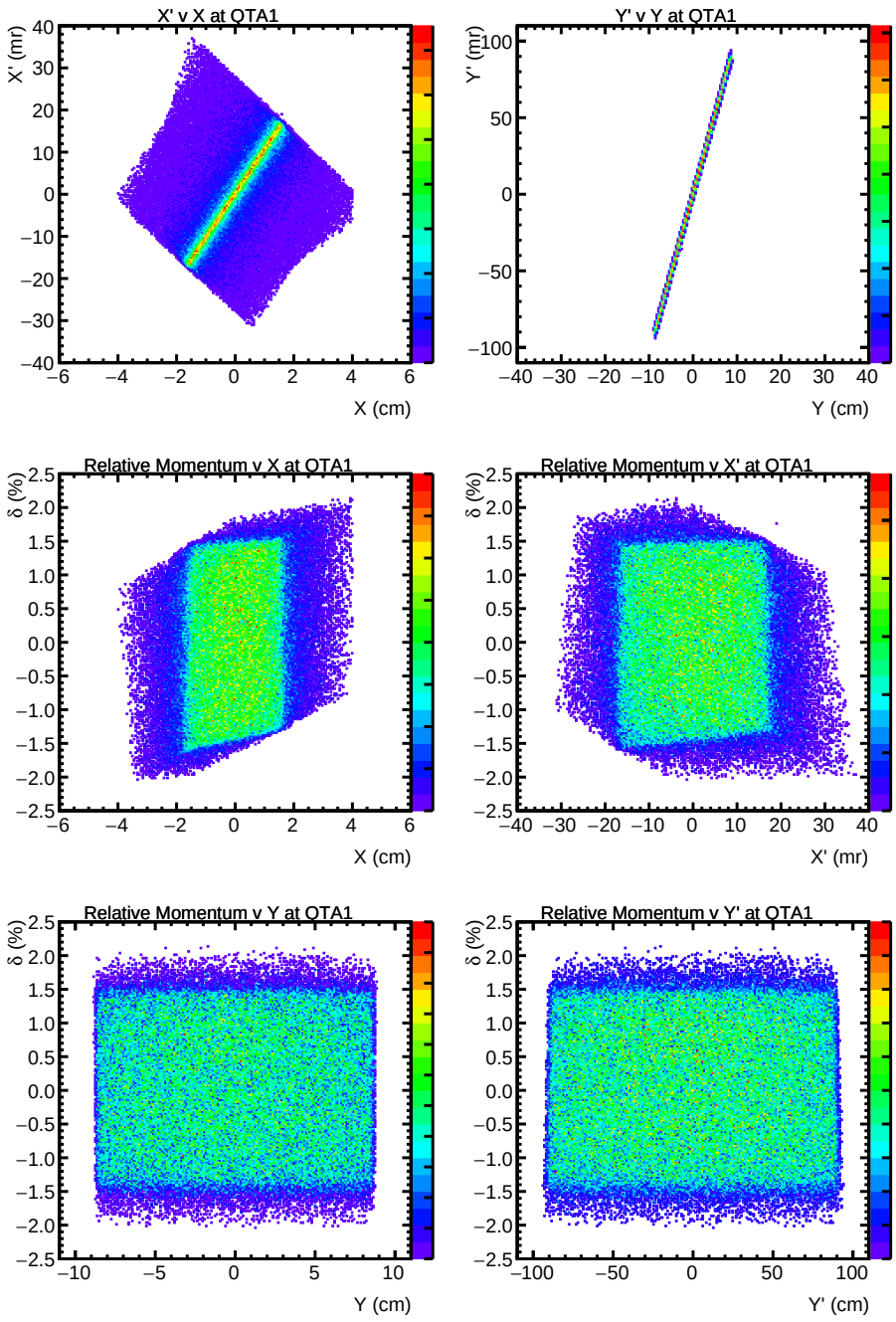

Figure 2.7: Correlations of particles at the QTA1 entrance that reach the GEM chambers after the PiM1 channel. ***Upper left***: x' vs x. ***Upper right***: y' vs y. ***Center left***: δ vs x. ***Center right***: δ vs x'. ***Lower left***: δ vs y. ***Lower right***: δ vs y'.

Chapter 3
Experimental Setup of PiM1

3.1 Experimental Overview

The full MUSE experiment is an elastic ep and μp scattering experiment. However unlike most experiments such as those performed at electron accelerator facilities, the PiM1 beam line is a secondary beam with multiple particle species in the beam. The beam has a large physical extent and comes to a focus at the PiM1 target due to focusing quadrupoles at the end of the beam line. Since MUSE needs to reconstruct vertices to high precision and determine TOF to perform a momentum measurement, MUSE has several beam line detectors before the target, in order to provide information about the incoming beam with the necessary precision. The experiment has access to 2 regions of PiM1, the IFP and the scattering target region, in addition to control of the channel elements, magnets, and jaws.

As can be seen in Fig. 3.1, the incoming beam first encounters the Beam Hodoscope (BH), which has two to four planes, depending on momentum, of BC-404 scintillator bars read out at both ends with Hamamatsu S13360- 3075PE SiPMs. The planes are organized in an array of 16 bars per plane. The central 6 bars, or paddles, measure 10 cm long $\times$ 4 mm wide $\times$ 2 mm thick and the outer 5 bars on either side measure 10 cm long $\times$ 8 mm wide $\times$ 2 mm thick. Aluminum foil is used to position each bar 6 μm apart to provide an air gap, which results in total internal reflection of scintillation light within the bar. Bars alternate in orientation, such that the first plane is oriented in y, the second plane in x, the third plane in y, and the fourth plane in x. To minimize geometric inefficiencies from particles passing between bars and not being detected, the second vertical (horizontal) plane is offset upwards (sideways) by 2 mm from the first plane. The BH assembly can be seen in Fig. 3.2. The BH measures incoming particle timing and the beam flux. The BH is read out by VME electronics for the charge measurement performed by a Mesytec MQDC 32 channel charge-to-digital converter (QDC) [33]. TRB3 boards [45], which are time-to-digital converters (TDC) with inputs from Mesytec MCFD constant fraction discriminators are used for the timing measurement [32]. The electronic components of the experiment will be discussed in Sec. 3.2. From extensive test beams it has been determined that the BH is 99.8% efficient and has a timing resolution of 80 ps/plane. A full

Parameter	Performance Requirement	Achieved
Time Resolution	<100 ps / plane	✓ 80 ps
Efficiency	99%	✓ 99.8%
Positioning	≈1 mm, ≈1 mr	not attempted; easy – calibrated by data
Rate Capability	3.3 MHz / plane	✓ >10 MHz / plane

Table 3.1: Beam hodoscope detector requirements

description of the BH status is given in Table 3.1. Development and design of the Beam Hodoscope was performed by Rutgers and Tel Aviv University.

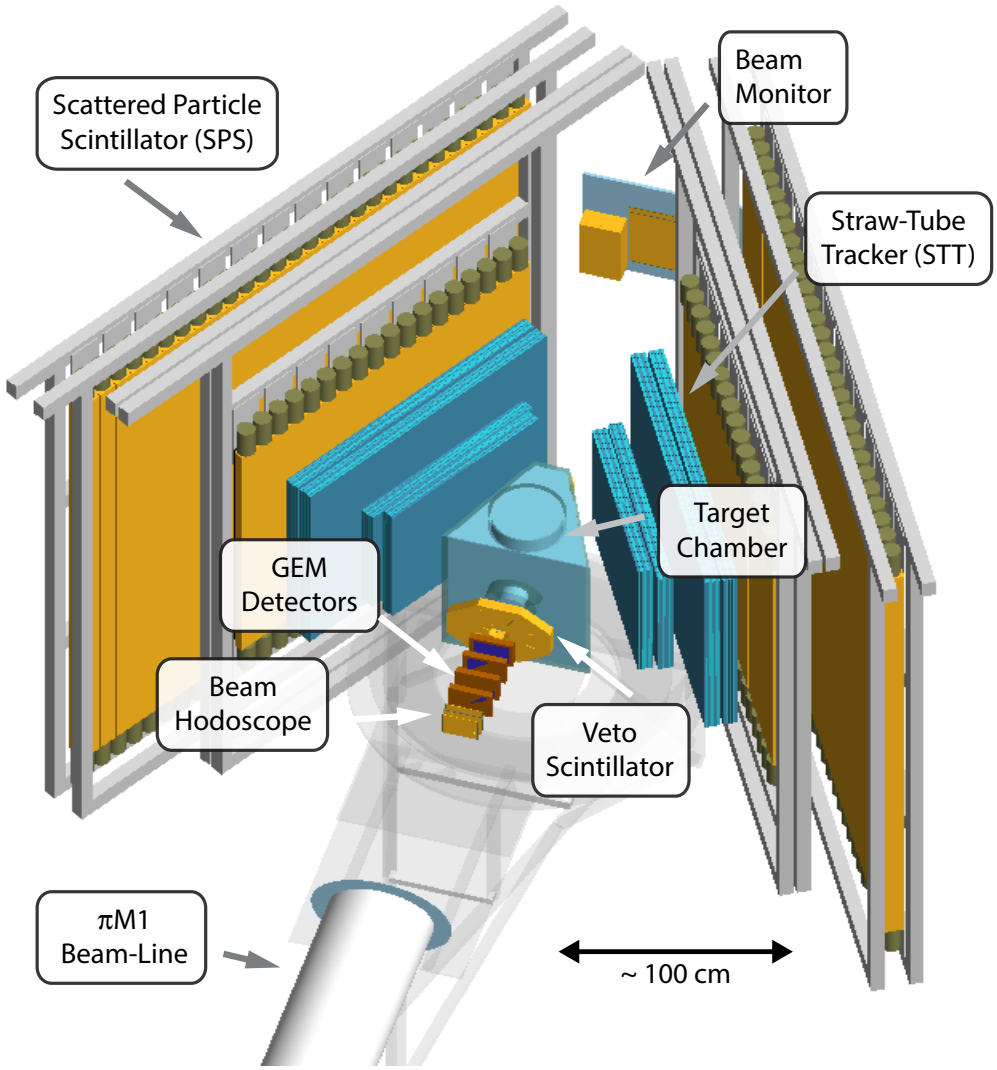

Figure 3.1: Geant4 sketch of the MUSE setup. Courtesy of Steffen Strauch.

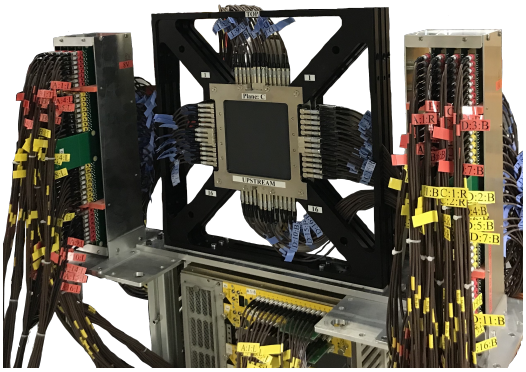

(a) 2 BH planes fully assembled, looking downstream to beam left. Readout electronics are to the sides of and below the BH.

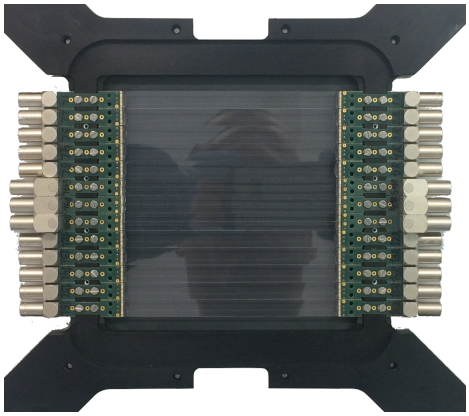

(b) A plane of BH scintillators and SiPMs without the covering.

Figure 3.2: The BH assembly

Parameter	Performance Requirement	Achieved
Resolution	100 μm / element	✓ 70 μm
Efficiency	98%	✓ 98%
Positioning	≈0.1 mm, ≈0.2 mr	planned
Rate Capability	3.3 MHz / plane	✓ 5 MHz
Readout Speed	2 kHz / 20% deadtime	1.5 kHz / 100% deadtime

Table 3.2: GEM detector requirements

The detector the beam encounters next is the Gas Electron Multiplier (GEM), developed and built by a group at Hampton University. Fig. 3.3 shows the GEMs. This position sensitive detector is placed between the BH and the target vacuum chamber in order to provide high precision tracks with a minimum of multiple scattering. The GEM material is approximately 0.5% of a radiation length per plane. Each GEM plane contains 4 Analogue Pipeline Voltage mode (APV) integrated circuits [15], two to measure in the x coordinate and two to measure in y. Every APV has 128 read-out strips 0.4 mm wide, with an overall tracking resolution of 70 μm and an efficiency of 98%. The active area of each GEM is 10×10 cm^2, which covers the 6σ width of the beam. The GEMs are read out by nonstandard VME electronics [30]. The current status of the GEM detector is given in Table 3.2.

The final detector before the target is a donut shaped veto detector, constructed by the group at South Carolina. While the PiM1 beam is extended it still fits through the 6 cm hole in the

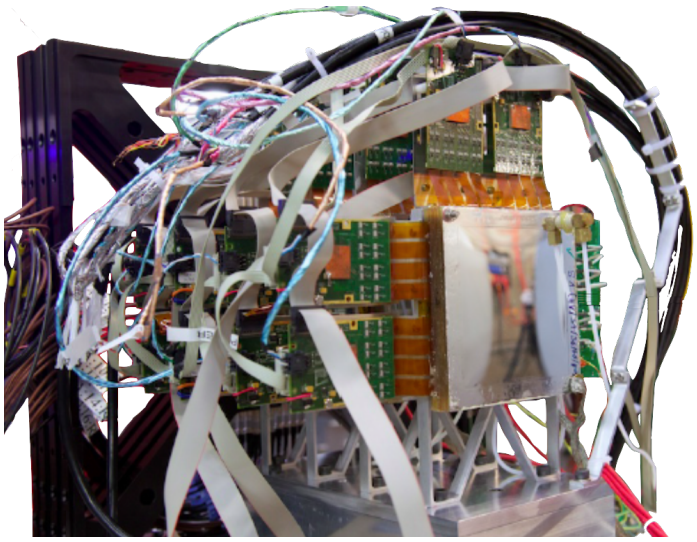

Figure 3.3: A view of the GEMs from beam right, looking up stream to beam left.

veto, which can be seen in Fig. 3.4. The purpose of the veto is to detect particles from decays in flight between the final dipole and the scattering target as well as particles that scatter in the BH or GEMs and might hit the thick metal of the cryotarget vacuum chamber. These decay particles, either $\pi^{\pm} \rightarrow \mu^{\pm}\nu_{\mu}$ or $\mu^{\pm} \rightarrow e^{\pm}\nu_{\mu}\nu_{e}$ have an unknown momentum and as such they cannot be used for MUSE. Many of these decays also decay at an angle that can be mistaken for a track in the scattered particle detectors. The veto prevents the upstream decay and scattering events from triggering the data acquisition system and being recorded to disk, reducing the system dead time and allowing more scattering events of interest to be recorded. Note that those decaying after that can still be removed from the event sample in offline analysis, to be described later.

After the veto is the LH_2 scattering chamber, built by the University of Michigan in conjunction with a private company, CREARE [41]. A design schematic can be seen in Fig. 3.5. Similar to many LH_2 targets constructed for other experiments, MUSE requires a vacuum scattering chamber with an internal, multi-stage target ladder. There are 4 stages to the ladder as depicted in Fig. 3.6, in descending order:

1. The first stage is the LH_2 target cell used for scattering.

2. The second stage is an identical target cell without any LH_2. This is used for background studies and subtraction.

3. The third stage is a 1mm thick segmented carbon and CH_2 target with a gap between the two materials. By having two solid targets we can perform calibration and tracking studies and verify the difference in cross section between each material.

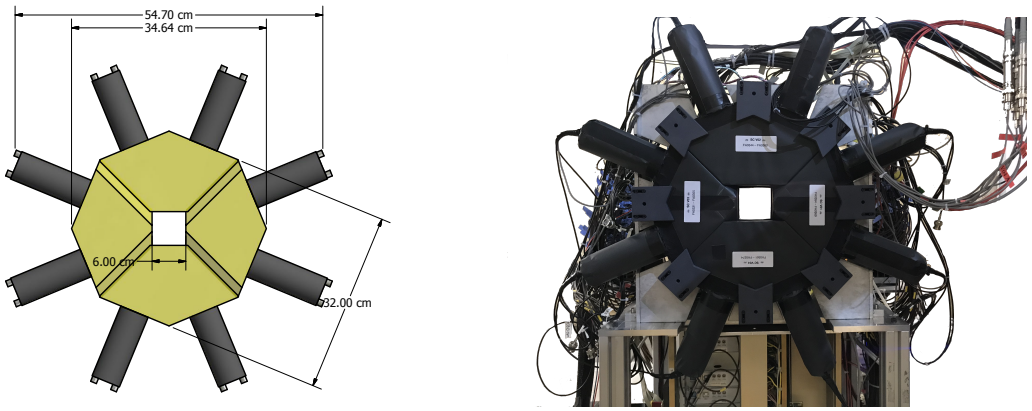

(a) A design schematic of the veto detector.

(b) A view of the veto looking upstream.

Figure 3.4: The VETO assembly

4. And the fourth stage is an empty space. This stage is used for TOF and dispersion measurements.

The entrance window to the scattering chamber nearly matches the size of the hole in the VETO. The beam entrance and exit windows are constructed with aluminized Kapton; both windows are 0.125 mm thick [41]. The scattering windows are 337 mm wide and 356 mm high and constructed from laminated Mylar.

On either side of the scattering chamber are the Straw Tube Trackers (STTs), which were developed by the group at Hebrew University. The STTs are single-ended position-sensitive drift chambers, which are designed to measure trajectories while inducing minimal multiple scattering in scattered particles. The STT is capable of determining tracks with 150 μm resolution. The STTs are centered at $\theta = 60°$ and cover an angular range of $20° - 100°$ in θ and $\pm 45°$ in ϕ. This allows for an angular coverage of $\approx 30\%$ of the typical 2π azimuthal range [17], and allows MUSE access to the desired Q^2 range. On both the left and the right side there are 2 STT chambers, a 60 cm chamber and a 90 cm chamber. The smaller 60 cm chamber is positioned closest to the scattering chamber and is divided into 10 planes. The 5 planes closest to the chamber are oriented vertically, which approximately gives a measurement of θ, the next 5 planes are oriented horizontally to approximately measure ϕ. This orientation was chosen to provide a more precise measurement of the scattering angle θ which is necessary for the Q^2 determination. The STT wire construction and one 60 cm plane cane be seen in Fig. 3.7. The 90 cm planes are oriented in a similar fashion. The STTs are read out by their analog signals being digitized by PASTTREC [38] discriminators, with the resulting digital signals input to the TRB3 TDCs. The STT status is given in Table 3.3.

Behind the STT on each side of the chamber are the Scattered Particle Scintillators (SPSs).

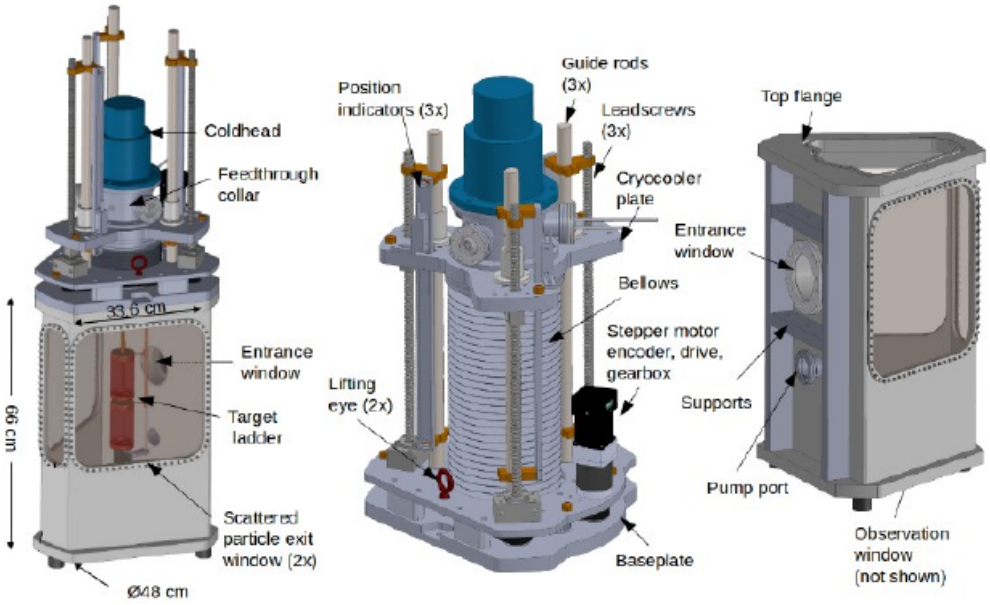

Figure 3.5: A design schematic of the scattering chamber.

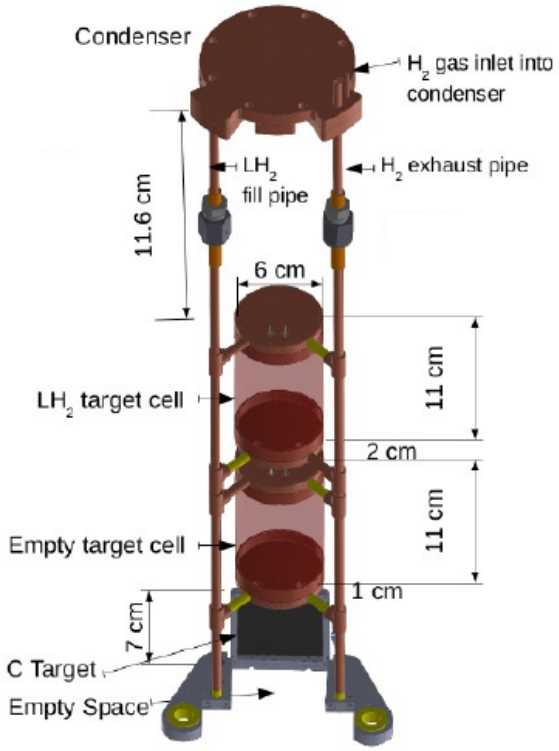

Figure 3.6: A design schematic of the target ladder.

Parameter	Performance Requirement	Achieved
Position Resolution	150 μm	✓ <120 μm
Efficiency	99.8% tracking	≈ 99% in prototype; moderate
Positioning	≈0.1 mm, 0.2 mr in θ	not attempted; moderate
Positioning	≈0.5 mr pitch, yaw, roll	not attempted; moderate
Positioning	50 μm wire spacing	✓ 35μm achieved in dress rehearsal
Rate Capability	0.5 MHz	not attempted; easy

Table 3.3: Straw Tube Tracker requirements

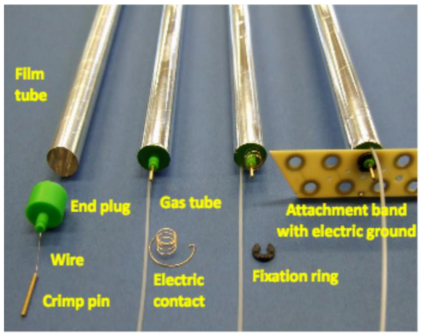

(a) The components of an individual straw.

(b) An edge-on view of a 60 cm straw plane.

Figure 3.7: The STT straws and assembled plane.

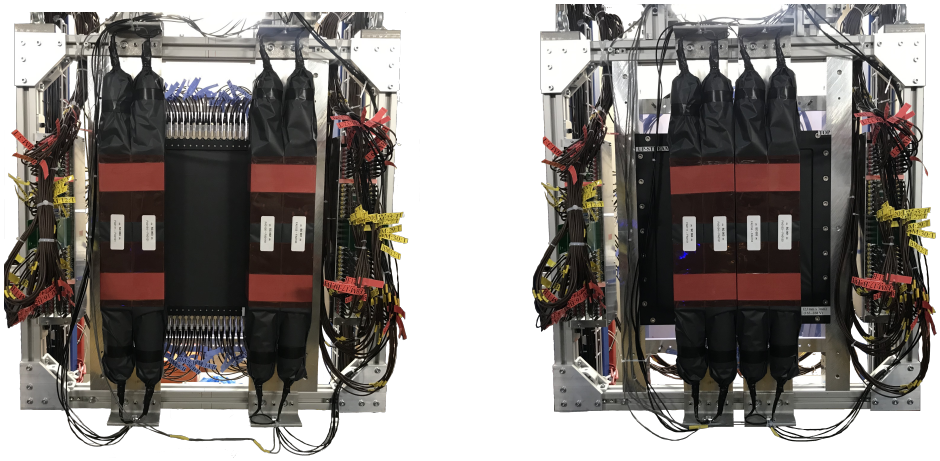

(a) The BM in the production data taking configuration.

(b) The BM in the TOF configuration. The larger scintillators are moved to the center of the assembly to provide a better time resolution of the beam.

Figure 3.8: The BM assembly

These are large scintillator bars used for the TOF measurement for scattered particles and for triggering. Each Eljen Technology EJ-204 plastic scintillator bar has a double ended Hamamatsu R13435 PMT readout with a total timing resolution of 55 ps. The South Carolina group that built the SPS previously developed the FToF12 for the CLAS12 JLab upgrade. The design was easily adapted to MUSE. There are two planes of scintillators on each side of the detector. For triggering purposes it is required to have a hit in the front and back wall of the SPS, as this reduces noise hits. The SPS has its pulse height information read out by Mesytec MQDCs in our VME electronics crates. The analog timing signals are discriminated by PaDiWa leading edge discriminators [48]. The digitized timing signals are read out by our one TRB3 board on each arm of the detector.

Downstream from the scattering chamber is the Beam Monitor (BM) which can be seen in Fig. 3.8. The Beam Monitor consists of 4 thick double-ended scintillator bars, and 2 planes each of 16 thin scintillator paddles attached to SiPMs. The large scintillator bars were constructed by South Carolina, and the thin scintillator paddles were constructed by Rutgers and Tel Aviv University. The BM is used to monitor the stability and flux of the beam and performs a TOF measurement when calibrating the beam and changing momentum. Similarly to the BH the BM has its energy deposition measured by our Mesytek 32 channel MQDCs. The analog timing signals are sent to Mesytek MCFD constant fraction discriminators and then fed to our TRB3 timing electronics.

The overall resolution of our DAQ is given in Table 3.4.

Parameter	Performance Requirement	Achieved?
TDC Resolution	$\leq$ 40 ps	✓ $<$ 30 ps
QDC Resolution	$>$ 10 bit	✓ 12 bit
Readout Rate	100 μs per event	400 μs per event to date, moderate

Table 3.4: Data acquisition system hardware requirements.

3.1.1 The IFP

The IFP is a region of air between the two bending dipoles of PiM1. A copper collimator at the IFP was developed for MUSE by Manuel Schwarz of PSI. The collimator is used to select the momentum bite of the beam. For the MUSE experiment production data the IFP will have the collimator set open such that the beam provides a flux of $\approx$ 3.3 MHz. The experiment expects to adjust the collimator opening up to approximately $\pm$8 cm to provide this flux; the exact openings will depend on the details of the beam tune and the opening of the FS11 jaws. There will be no additional material at the IFP. For TOF and dispersion measurements taken during 2018 two GEM planes were placed at the IFP, in order to make a measurement of the beam distribution for comparison to simulation. The GEMs at the IFP were not surveyed so their exact positions and angle offsets are unknown, with offsets of several mm and several degrees possible.

Matrix elements were computed that show the coupling between IFP position and angle and the target position and angle. These matrix elements can be compared to data which can verify the simulation. If the simulation can be verified between IFP and target region then it gives confidence in the full channel simulation.

3.2 DAQ

The Data Acquisition System (DAQ) reads out the fast event data, detector signal times and pulse sizes, for event analysis and detector calibration and slow controls. Our DAQ control software is MIDAS, developed by Stefan Ritt at PSI in collaboration with TRIUMF. MIDAS was designed specifically for flexibility and use in medium scale experiments. MIDAS controls all of our frontends (seen in Fig. 3.9), and writes data out event-by-event in a binary data format known as a MIDAS file. This file then is converted to a ROOT tree [9] and analyzed using the MUSEcooker, a fork of the DESY OLYMPUS analysis framework, designed by Jan Bernauer of Stony Brook University. The MUSEcooker is a flexible plugin based analysis framework ideal for easily scaling an experiment's

analysis from initial detector prototyping stages to a full cross section measurement. The analysis software is stored on GitHub to provide for flexible and distributed analysis development between multiple institutions.

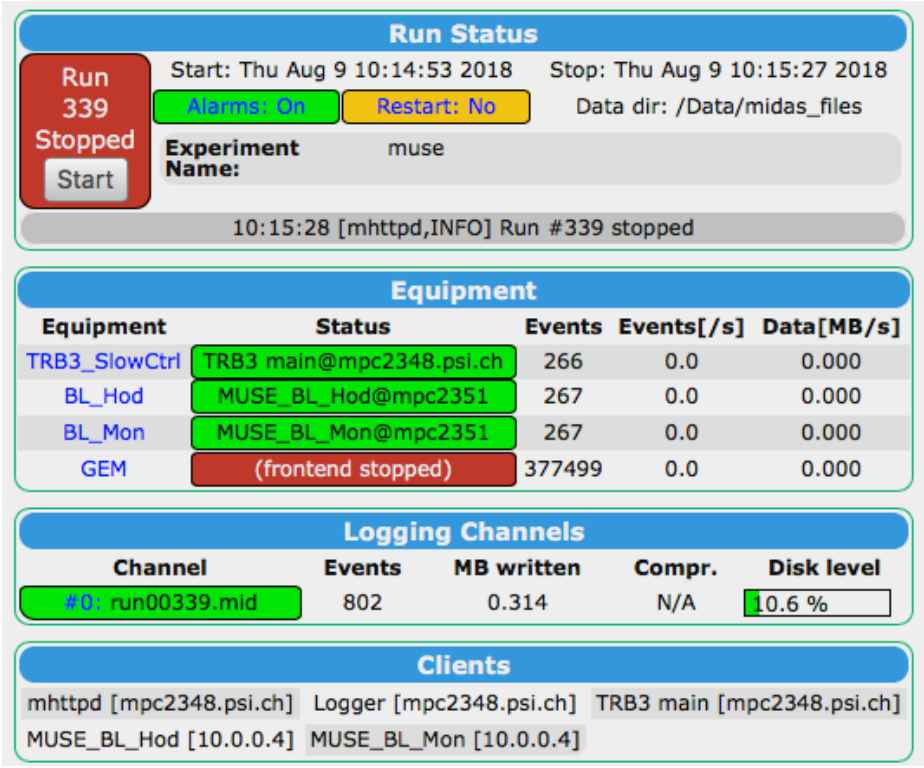

Figure 3.9: A screenshot of the central DAQ system control GUI. Displayed are the beam line frontends being used for the TOF measurements.

The DAQ hardware has a TDC resolution of less than 30 ps, and 12-bit QDC resolution. The readout rate in 2018 was $\sim 300 - 400$ Hz at 100% dead time, completely dominated by the GEMs. This read out rate is significantly slower than the MUSE requirement of 2.2 kHz at 20% dead time, but sufficient for the purposes of the measurements presented here, where we are not concerned with dead time corrections to determine an absolute normalization. Simulations will be normalized to the experimental data, Since this data was taken, the read out speed of MUSE has increased four-fold, achieving our 20% dead time requirement.

The timing electronics are comprised of several components. All SiPM electronic signals are sent to amplifier boards, with outputs sent to Mesytec MCFDs [17]. MCFDs are constant fraction discriminators that provide reliable high precision timing. The MCFDs provide two outputs, an LVDS digital discriminator output that is sent to the TRB3 TDC [32], and an analog copy of the input signal that is sent to the QDC. The MCFD also provides an OR output that can serve as a

QDC gate [33].

The TRB3 timing read-out board is a multi-purpose, high-precision, TDC [45]. Each board has 5 FPGAs, with one central FPGA used for triggering and communication with the other 4 and the rest of the DAQ system. The 4 peripheral FPGAs are used as high-precision TDCs, with a channel to channel resolution of 11 ps. Each peripheral FPGA can read-out 3 sets of 16 channels. Three MCFDs can be read out by a single FPGA. TRB3s are standalone electronics which do not follow VME standards. One TRB3 is set as a master control that communicates and reads out all other TRB3s. This master also communicates with the DAQ computers via gigabit ethernet [45]. Each TRB3 communicates via UDP packets with the DAQ and the read out following a streaming model. The TRB3 does not become busy when it receives a trigger; instead a UDP packet is created and sent along the pipeline to the master board which performs the event synchronization [17]. This is in direct contrast to the common-stop VME readout in which electronics become busy when a trigger is received and a data package is constructed.

VME readout is provided by standard VME crates and a CAEN v2718 VME-PCI bridge in each crate, that is connected by an optical bridge to our DAQ computer. To synchronize the VME and TRB3 electronic system an event number is generated by the master TRB3 and sent to each VME crate via a VULOM 4b module. This event number is folded into the VME data stream and into the TRB3 data stream so synchronization can be performed offline by the analysis software.

The Mesytec MQDC-32 is a 32 input-channel VME module which provides QDC information for the scintillators [33]. This QDC information is used to monitor the gain of our detectors and provides particle identification. For the SPS, where pulse sizes are needed for every event, the analog signals are delayed and the MQDCs are gated by the event trigger. For other detectors, the MQDCs are gated by the MCFD OR output, leading to a dead time for the signals; QDC information is not available for these detectors for all events. The MQDCs have an internal read-back delay that matches the MCFDs timing signal with the charge read-out. This mode of operation removes the need for delay cables but causes slight inefficiencies in readout resulting in a fraction of the events being lost.

3.2.1 The Trigger and BUSY Logic

The MUSE trigger is designed to record events of interest for our DAQ and ignore noise and various background processes. The trigger is a two-level trigger, with several first-level triggers fed into a second-level master trigger which makes the final trigger decision. The first-level and second-level triggers, along with the BUSY logic, are listed below. Each resides on spare TRB3 FPGAs unless otherwise noted and the BUSY logic comes from our VME crates:

1. PID: The particle identification trigger takes input signals from each BH bar and the accelerator RF signal. The particles in the beam are well separated in RF at the 3 MUSE momenta. This trigger allows MUSE to veto π's and trigger on e's and μ's on a bar by bar basis. The output of all the bars is then ORed together. This trigger was used for the TOF and dispersion measurements but was set up to not veto the π?s, so that all particle types could be measured.

2. VETO: The VETO takes input signals from the VETO detector. The veto detector has 2 PMTs that look at each of 4 scintillator paddles. We use coincidences of the 2 PMTs of a single paddle to inhibit the master trigger, to prevent noise in a single PMT from inhibiting real events. This trigger was not used for the TOF and dispersion measurements, but was included in the data stream so it could be included in offline analysis.

3. LUT: The Look Up Table (LUT) takes its input from the SPS detector. This trigger looks for hits in the front and back SPS walls that could come from scattered particles. This suppresses particle decays that tend to come at smaller angles, and noise in the scintillators, which is independent in each PMT. This trigger was also not used for the TOF or dispersion measurements.

4. BM: The BM trigger takes input signals from the BM detector. The BM detector identifies beam particles that do not scatter as well as forward going electrons or positrons from Moeller and Bhabha scattering events. However given the ability of this trigger to warp the shape of the angular distribution it is not anticipated that MUSE will use this trigger for production data taking. This trigger was used for the TOF and dispersion measurements. This NIM trigger ANDs the top and bottom of each BM scintillator bar and then ORs all the ANDed signals together.

5. BUSY: The busy logic is produced by VME modules, both the MQDCs and the GEMs. These VME modules operate on a common stop type logic and record data with a moving data window until they receive a trigger signal. Once a trigger is received the VME modules send a BUSY signal to the master trigger, indicating that they cannot accept more data. Once the VME data is packaged and sent to the DAQ, the BUSY is cleared and the VME modules are ready for the next event.

6. MASTER: The second level trigger is our master trigger which ANDs together first level triggers. For the TOF and dispersion measurements, the PID trigger was ANDed with the BM trigger. This type of master trigger reduces background and enforces that a particle actually travels the entire distance for the TOF measurement. Several different master triggers can be

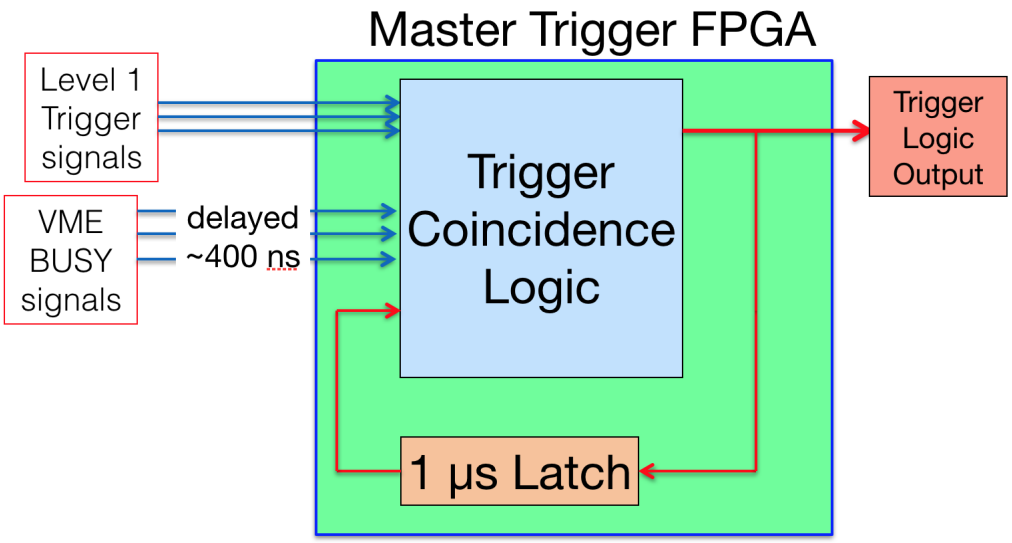

Figure 3.10: A schematic diagram of the master trigger logic.

generated in parallel, with different prescale factors for each.

3.3 Data Taking Plan

All data was taken during the August 2018 beam time. This beam time was held exclusively for measurements aimed at better understanding the π, μ, and e beams in PiM1. It was found after the beam time that the last quadrupoles at the end of the beam line, QSL17 and QSL18, were set to the wrong current polarities during the data taking. This means instead of focusing in x and then y as particles enter PiM1, focusing occurred in y and then x. This had no impact on the TOF measurements other than a slightly defocused beam. However for dispersion measurements and comparisons with simulation it created a potentially significant impact on the beam spot. This will be discussed in more detail in Chapter 5.

3.3.1 The TOF Measurement

For the TOF measurement only the beam line detectors (BH, GEM, VETO, and BM) were used. At the time the measurements were taken the STT was not in place, and the SPS was not connected to the DAQ. The measurements discussed here are an attempt to measure the beam particle momenta and beam distributions without scattering, and for this purpose the scattering chamber was placed in its "empty" configuration. During this data taking the vacuum chamber was offset vertically upward by 1 cm. This introduced background in our measurements which will be discussed in Sec.

5.4 The measurements were performed for all 3 MUSE momenta, 117, 161, and 210 MeV/c, and for both positive and negative charge polarities.

The upstream beam line detectors (BH, GEM, and VETO), are on a moveable sled which slots in to well defined dowel positions. The downstream BM is placed on a rail system with stops at the farthest upstream and downstream position. The BM can be clamped into place at these stops. The different BH and BM measurement locations and their distances are shown in Fig. 3.11.

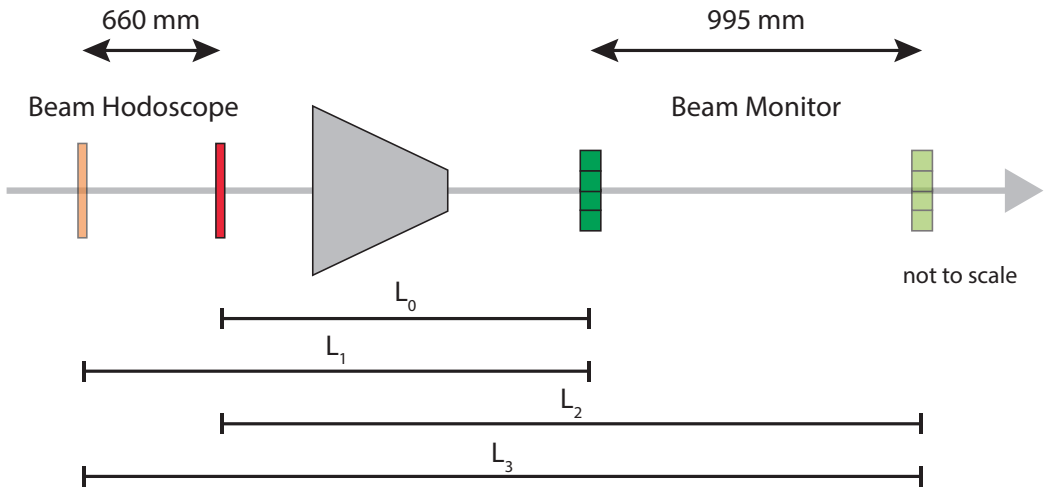

Figure 3.11: Not-to-scale bird's eye sketch of the MUSE setup during TOF measurements. The beam enters from the left. The BH and BM detectors were each positioned in two positions along the beam axis, creating four different path-lengths for the TOF measurement.

3.3.2 Dispersion Measurements

A series of measurements were taken in parallel with the TOF studies to characterize the use of the PiM1 magnetic channel as a spectrometer. Since the IFP beam spot is $\approx$ 20 cm wide, but the GEMs have only a 10 cm $\times$10 cm active area, we prepared two movable GEM detectors to be placed at the IFP for these measurements. These GEMs moved horizontally parallel to the collimator setting, thereby ensuring the IFP beam spot could be captured by the IFP GEMs. The IFP GEMs provided initial particle tracks before the final channel bending magnet, ASM12. These GEMs also allowed for a direct measurement of the matrix elements between the IFP and target region for comparison to simulation. With this experimental set-up, we performed the following types of measurements:

1. Quadrupoles between IFP and the PiM1 target ON, with and without the two GEM planes at the IFP. Data were taken for e, μ and π at various central momenta.

2. Quadrupoles between IFP and the PiM1 target OFF, with and without the two GEM planes at the IFP. Data were taken for e, μ and π at various central momenta.

The measurements with the quadrupoles ON or OFF allowed us to study the influence of focusing effects of the quadrupoles on the particles before and after the ASM12 dipole, and the beam distribution at the target. The motivation behind taking data with and without GEMs at the IFP was to study energy loss due to the GEM material, and compare its effects on momenta and beam sizes at the PiM1 target with a simple Geant4 simulation of the GEMs.

Chapter 4
Simulation of the PiM1 Secondary Beam Line

The simulation is broadly distributed in three major components. The first is a simulation of the e, μ, and π sources at the M production target. The second is a simulation of the PiM1 beam line as a whole, and the third is a more specific TOF simulation. All simulations are multi-faceted and are comprised of multiple simulation components. All of these simulations will be discussed in detail in this Chapter. The description will have the following logical flow.

1. **Source Size Simulations**: The source sizes for the e's and μ's were simulated in both Geant4 and ROOT. While Geant4 contains standard physics packages and can accurately describe particle decays as particles pass through matter, it can also be cross verified with a simple ROOT code that generates particles based off of our understanding of the distributions of π's in the beam. The simulations were written by Win Lin and Ronald Gilman of Rutgers.

2. **TURTLE Simulation**: Trace Unlimited Rays Through Lumped Elements (TURTLE) is a Fortran 77 based beam line simulation package provided by PSI. An existing TURTLE description of the PiM1 beam line was used by PSI and was provided to MUSE upon request. The MUSE implementation is based on the default PiM1 simulation of PSI, with updated geometry. We ran simulations for multiple sources with default channel settings and with settings actually used in 2018. TURTLE has several source options, including an input deck of rays which it transports through the PiM1 channel. This input deck is informed by the source size simulations above. The TURTLE input deck was modified by Ronald Gilman.

3. **G4beamline Simulation**: G4beamline is an extension of Geant4, built upon Geant physics libraries, developed by Muons, Inc. and available as a freely distributed program. G4beamline is used to model particles traversing a beam line as well as energy loss effects from any materials the particles may encounter. It is designed to be flexible and easy to read and write for anyone without a C++ programming background. This program also uses an input deck that is informed by the source size simulations. G4beamline is used as a cross check of the TURTLE simulations. The simulations were developed by Paul Remier of Argonne and Priya Roy of the University of Michigan.

4. **TOF Simulation**: The TOF simulation is part of the total MUSE simulation package describing the entire experiment. It is built wholly upon Geant4 and the FTFP_BERT physics package. This simulation was developed by Steffen Strauch of South Carolina University. This simulation has been used to simulate scattering, estimate systematic uncertainties, and investigate background subtraction. This simulation is independent of the source size simulations, it simply requires an accurate description of the beam coming out of the PiM1 channel. The simulation is informed by experimental measurements of the beam and then can be compared to experimental TOF data to extract the momentum of the beam.

The source size simulations inform the TURTLE and G4beamline simulations, which provide a description of the magnetic channel and beam dispersion. The TOF simulation independently is used to extract the momentum of the beam. Bringing all of these simulations together with data allows MUSE to claim a detailed understanding of the PiM1 beam line, and it will be shown that the momentum of the beam can be known to within the required uncertainty.

4.1 Source Size Simulations

In order to model the particle sources we need to have a model of pion production, the geometry of the target (as described in Sec. 2.2), the acceptance of the magnetic channel (included in Sec. 2.3.1), and a Geant4 simulation of π's producing e's along with a simple ROOT simulation for π's producing μ's.

From Sec. 2.3.1 we are able to implement cuts in our simulation to get a realistic description of our beam properties. The calculations shown were used to generate cuts for the muon and electron source simulations. They define limits on the maximum and minimum x_{QTA}, x'_{QTA}, y_{QTA}, y'_{QTA}, and δ_{QTA}, plus correlation cuts. These variables are the standard coordinate variables at the entrance to the QTA1 magnet. δ is the relative momentum, expressed as a percentage of the central channel momentum. The correlation of y'_{QTA} in mr vs. y_{QTA} in cm was implemented as $10.55y_{QTA}$+15 $> y'_{QTA} > 10.55y_{QTA}$-15. The correlation of x'_{QTA} in mr vs. x_{QTA} in cm is a diamond shaped region, implemented with a combination of 4 cuts, $13.5x_{QTA}+58 > x'_{QTA}$, $-7.0x_{QTA}+32 > x'_{QTA}$, $-6.5x_{QTA} - 30 < x'_{QTA}$, and $7.0x_{QTA} - 36 < x'_{QTA}$. The correlation of momentum in % with position x_{QTA} in cm used cuts $22.5x_{QTA}$+1.9 $> \delta_{QTA} > 22.5x_{QTA} - 1.8$. No cut was applied for a correlation of δ_{QTA} vs. x'_{QTA}. The cuts described are intended to be slightly oversized so that all particle making it through the channel will pass the cuts, but most particles not successfully traversing the channel will be rejected. This allows an approximate determination of the source size as well as improved efficiency in running the full channel simulation, which can require significant

CPU time.

4.1.1 Muon Source Simulations

The correlations and cuts discussed above, coupled with our knowledge that the proton beam spot is 2 mm wide, and the lever arm between the M target and the front face of the first quadrupole QTA1 being 95.8 cm allows us to begin to model the $\mu^{\pm}$ and $e^{\pm}$ source sizes. For $\mu^{\pm}$ we ran simulations in ROOT and verified the results in Geant4. Figs. 4.1, 4.2, and 4.3 show the output of the ROOT simulations. We ran 10^9 π's with a uniform distribution in kinetic energy and solid angle, for a momentum range of $100 - 400$ MeV/c, and angles up to 21° from PiM1. In all three figures the top left panel shows the π decay with distance, the top center panel shows the μ distribution at the entrance of QTA1 in the plane transverse to the aperture. Note that the acceptance of QTA1 as described in Sec. 2.3.1 is ± 4 cm in x and ± 9 cm in y, which is much smaller than the distributions shown for μ's at QTA1. The top right panel shows the relation between π momentum and angle for π's that decay to μ's and make it through QTA1 and our correlation cuts, thereby demonstrating our input distributions are sufficient. Our overall efficiency of producing μ?s into PiM1 from the source pion distribution described is of order 10^{-5}.

The bottom panels of Figs. 4.1, 4.2, and 4.3 show the effective μ source distributions for muons that make it to the PiM1 experimental area. The bottom left panel shows the y vs. x correlations at the M target for particles that go down the beamline to PiM1. The bottom middle and right panels show a one dimensional projection of these distributions along with an exponential fit, with characteristic lengths of 1.32, 1.24, and 1.25 cm for 120, 155, and 210 MeV/c respectively in x and 0.91, 0.85, and 0.82 cm in y. The total widths are ± 5 cm in x and ± 1.5 cm in y. We will see later that this is consistent with the TURTLE simulation for x but the y production region is limited to 0.5 cm. Muons at large $|y|$ pass the QTA cuts but are absorbed away later in the beam line and do not reach PiM1.

The Geant4 simulation shows exponentials with characteristic length of 1.24, 1.22, and 1.23 cm in x and 1.04, 0.80, and 0.84 cm in y. These modifications are primarily due to interactions with the graphite disk, which was not included in the ROOT simulations discussed above. For the initial TURTLE and G4beamline mom simulations, we used for simplicity a muon source with an approximately average exponential decay lengths of 1.28 cm in x and 0.87 cm in y for all beam momenta.

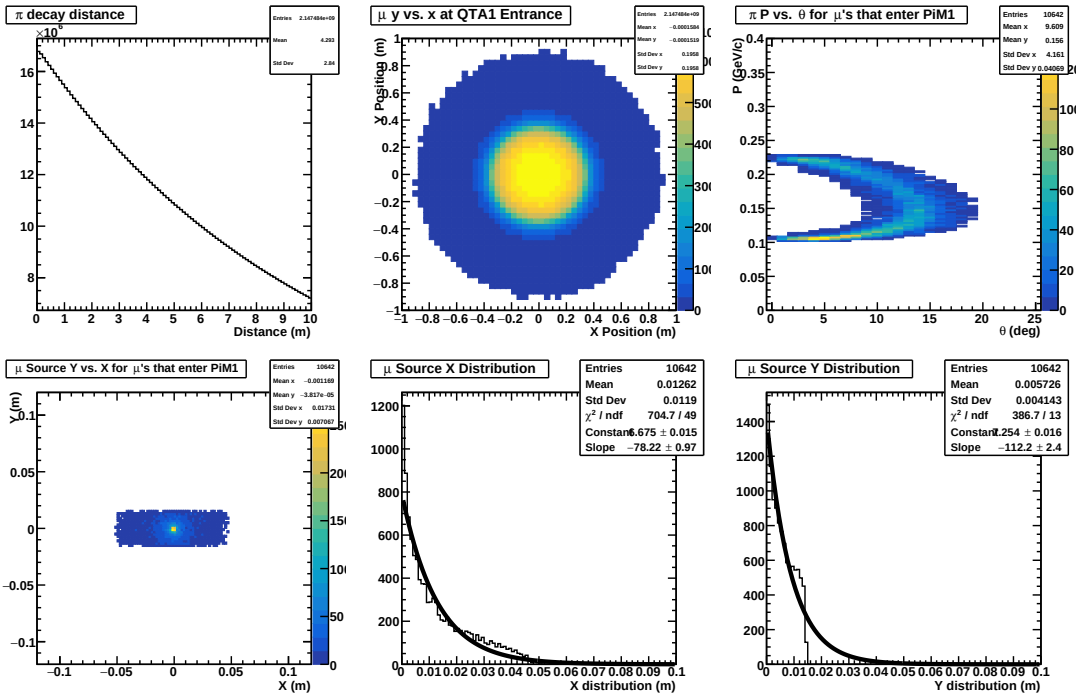

Figure 4.1: Output of root simulation of the muon source size, for 120 MeV/c channel setting. ***Upper left***: Decay distance for pions in m. ***Upper middle***: y (m) vs x (m) for muons at the entrance to the first quad. ***Upper right***: Momentum in GeV/c vs angle in degrees of pions that generate muons that pass the first quad aperture cuts. ***Lower left***: y (m) vs x (m) at the source plane of muon tracks that pass the first quad aperture cuts. ***Lower middle***: Distribution of x (m) at the source plane for muon tracks that pass the first quad aperture cuts. Also shown is an exponential fit to the distribution. ***Lower right***: Distribution of y (m) at the source plane for muon tracks that pass the first quad aperture cuts. Also shown is an exponential fit from $x = 0$ to $x = 0.1$ m to the simulated distribution.

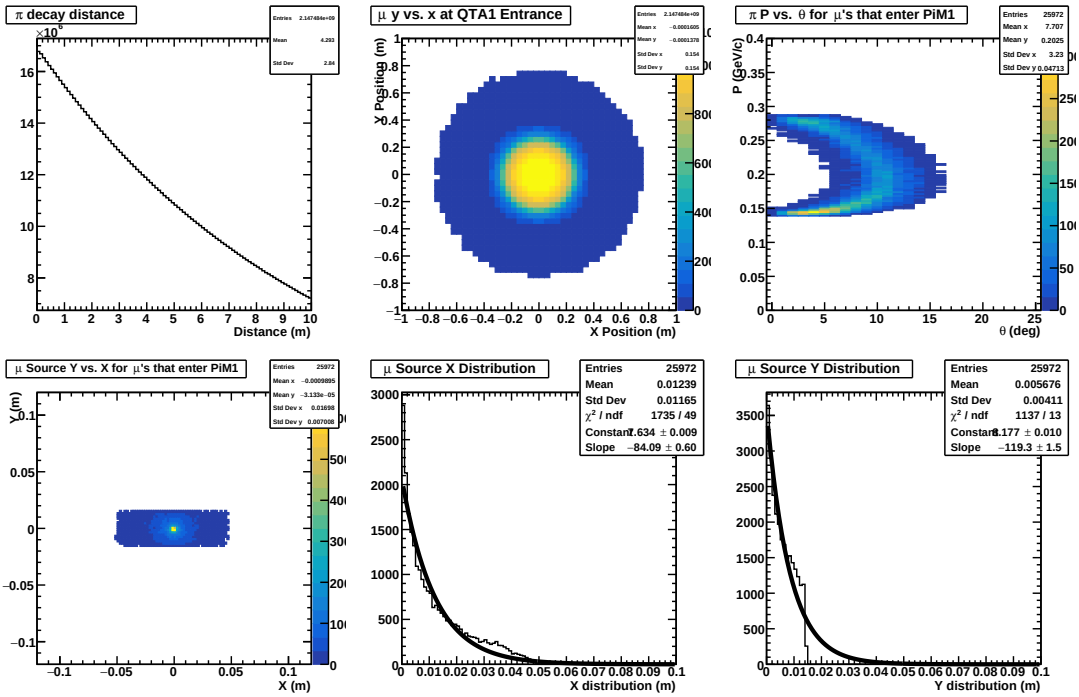

Figure 4.2: Output of root simulation of the muon source size, for 15 MeV/c channel setting. ***Upper left***: Decay distance for pions in m. ***Upper middle***: y (m) vs x (m) for muons at the entrance to the first quad. ***Upper right***: Momentum in GeV/c vs angle in degrees of pions that generate muons that pass the first quad aperture cuts. ***Lower left***: y (m) vs x (m) at the source plane of muon tracks that pass the first quad aperture cuts. ***Lower middle***: Distribution of x (m) at the source plane for muon tracks that pass the first quad aperture cuts. Also shown is an exponential fit to the distribution. ***Lower right***: Distribution of y (m) at the source plane for muon tracks that pass the first quad aperture cuts. Also shown is an exponential fit from $x = 0$ to $x = 0.1$ m to the simulated distribution.

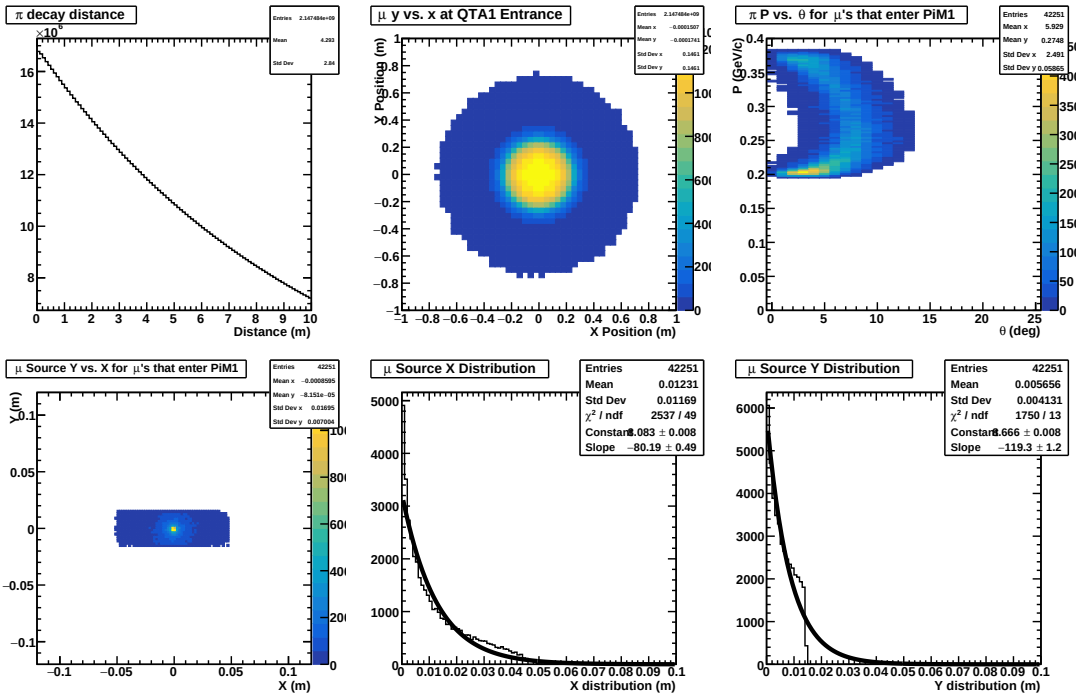

Figure 4.3: Output of root simulation of the muon source size, for 210 MeV/c channel setting. ***Upper left***: Decay distance for pions in m. ***Upper middle***: y (m) vs x (m) for muons at the entrance to the first quad. ***Upper right***: Momentum in GeV/c vs angle in degrees of pions that generate muons that pass the first quad aperture cuts. ***Lower left***: y (m) vs x (m) at the source plane of muon tracks that pass the first quad aperture cuts. ***Lower middle***: Distribution of x (m) at the source plane for muon tracks that pass the first quad aperture cuts. Also shown is an exponential fit to the distribution. ***Lower right***: Distribution of y (m) at the source plane for muon tracks that pass the first quad aperture cuts. Also shown is an exponential fit from $x = 0$ to $x = 0.1$ m to the simulated distribution.

4.1.2 Electron/Positron Source Simulations

Fig. 4.4 shows the geometry of the Geant4 simulation of the M target. Note that the Geant4 simulation uses $x = -x_{transport}$ and $y = -y_{transport}$. A simplified version of the M target is used compared to Fig. 2.1. We have the 2 mm flange perpendicular to the disk and generate π's at $z = 0$. We do not attempt to simulate π production from the proton beam on the carbon, as this is computationally impossible without thousands of processing cores performing the calculations [6]. We instead assume that the cross section for production of neutral pions, whose decays generate the electron/positron PiM1 beams, are about flat with kinetic energy and angle, as are the charged pion production cross sections we use to generate PiM1 muons. We evaluate electron distributions at 3 locations, the source at $z = 0$ cm, directly after the production target at $z = 2.55$ cm, and before the entrance to QTA1 at 94.5 cm, 1 cm before the aperture. By applying our correlation and acceptance cuts on the QTA1 evaluation plane, we can use built in Geant4 functionality to trace particles surviving our cuts to reconstruct a source distribution.

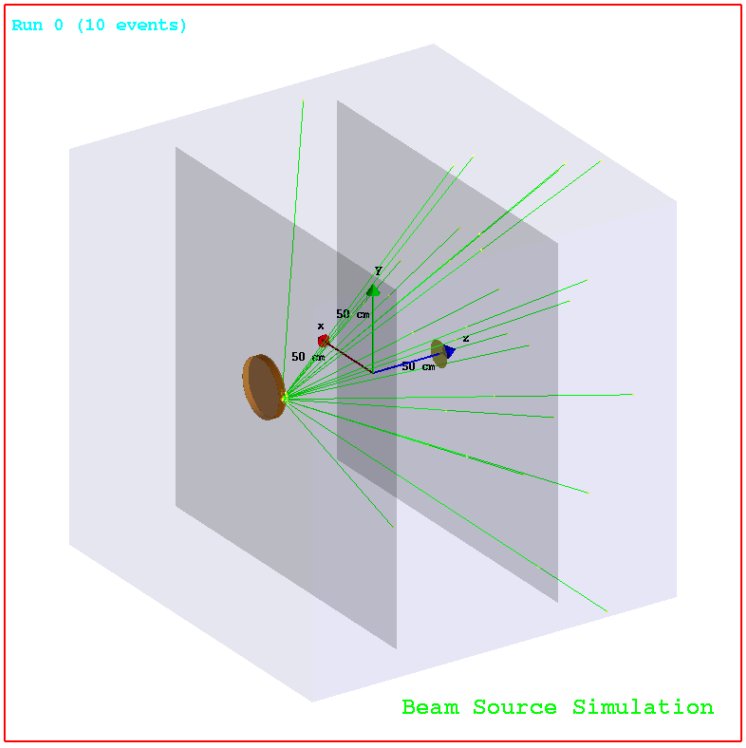

Figure 4.4: Geometry of the M target region used in the Geant4 simulations. Courtesy of Win Lin of Rutgers.

Geant4 takes into account both sources of e's from π decays: the $\pi^0 \to \gamma\gamma$ decay followed by γ conversion in the target, and the Dalitz decay $\pi^0 \to e^+e^-\gamma$. Without the graphite disk, there can be

no γ conversion so only the Dalitz decay is possible. This is seen in the left panel of Fig. 4.5. This figure shows all generated $e^{\pm}$, only the few central mms of this distribution will make it past our cuts on QTA1. The right panel of the figure includes the graphite disk, and shows a curve in the $+x$ direction and an enhancement of events on the $+x$ side, this corresponds to the orientation of the graphite disk. Notice that the number of electrons / positrons in the right panel of Fig. 4.5including the gamma gamma decay channel and conversion is about 10 times greater than the number in the left panel, which only includes Dalitz decays.

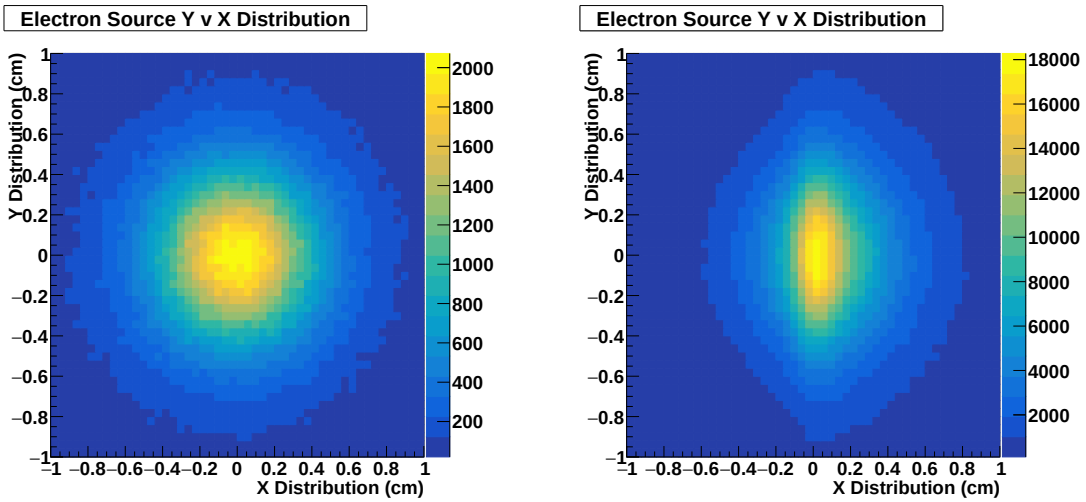

Figure 4.5: Electron/positron distributions on the test plane immediately after the position of the M target graphite disk. ***Left Panel:*** The distribution when the simulation throws π^0's from the source, but without the graphite disk, so that only Dalitz decays are shown. ***Right Panel:*** The full simulated distribution including both γ conversion in the graphite disk and Dalitz decays.

When we apply our correlation and acceptance cuts we see the few mm sized source distribution shown in Fig. 4.6. The x and y projected distributions are shown in Fig. 4.7. Both distributions have an RMS width of ≈ 0.4 mm. We note that the slightly wider y distribution is likely due to the full amount of graphite that electrons and positrons must pass through in y before entering QTA1. In the $-x$ direction the photons leave the graphite quickly and cannot convert, but in the $+x$ direction photons pass through both the flange and the graphite disk. This accounts for the slight offset in x and its narrower width. This was also seen in the right panel of Fig. 4.5. It is worth noting that for simplicity the initial π^0 distribution was simulated at a point, rather than across the entire flange, therefore we should add the full flange width of 2 mm to our electron distribution widths. However since the electron source distribution appears to be so much smaller than the flange width, it is sufficient to use the *same* source size, the 2 mm flange width, as the source size for both

e's and π's. The effective QTA1 distribution after satisfying all the QTA1 cuts is shown in Fig. 4.8

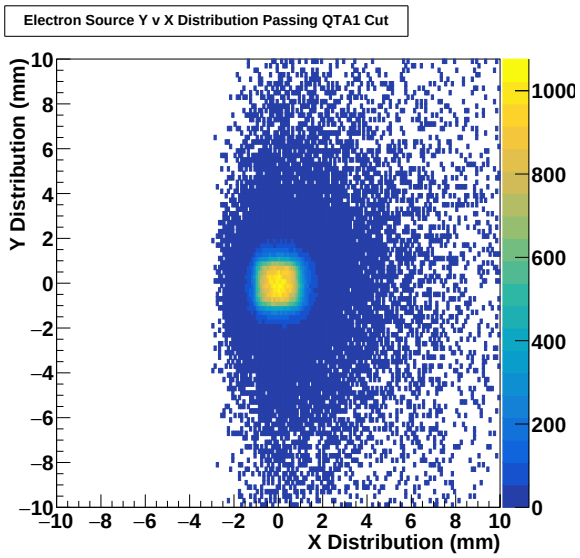

Figure 4.6: Electron/positron source distributions for electrons satisfying QTA1 cuts and correlations.

To further characterize the $e^{\pm}$ source distributions we also investigated the momentum, angle, and position correlations in the electron sources with no momentum or angle cuts on QTA1. The momentum distribution of the electrons entering QTA1 is shown in Fig. 4.9, while the momentum vs. position correlations are shown in Fig. 4.10. For a fixed $y = 0$ plane we see that as we move along x the momentum drops rapidly, and it is slightly higher on the $+x$ side, where the graphite disk is located. For a fixed $x = 0$ plane as we move along y we also see the momentum drops quickly but not as quickly as in x. In order to generate a large source size of $e^{\pm}$ rather than the small source we see in our simulations, a γ would need to be created moving at large angle to the QTA1 aperture, pass through several cm of graphite, and then convert to an $e^{\pm}$ at a large angle to the γ direction, while still having sufficient momentum to pass our momentum selection in the PiM1 channel. The probability for this is small and so the electron source size is small in the x direction. It is more likely in the y direction, but as has been mentioned previously and will be expanded upon further in Sec. 4.2, the channel acceptance is more limited in y than in x.

We conclude that the $e^{\pm}$ source size is small and consistent in size with the $\pi^{\pm}$ source size. Consistent source sizes imply consistent behavior in the magnetic channel and essentially identical channel properties. Any differences observed most likely come from multiple scattering and energy loss mechanisms from material in the beam, or potentially from decays in flight in the case of π's. We conclude the effective muon source size is 1.28 cm in x by 0.5 cm in y, while the pion and electron

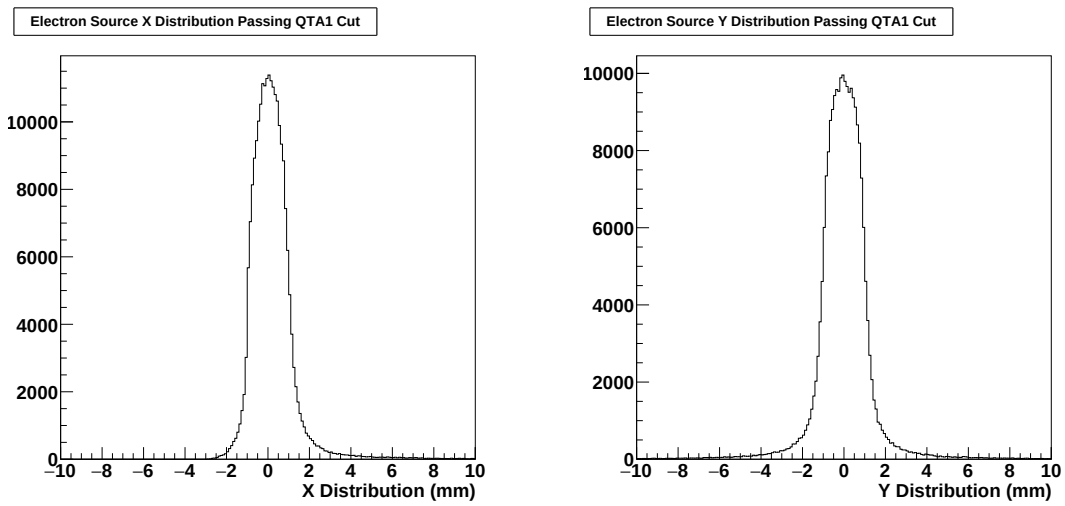

Figure 4.7: Electron/positron source distributions for electrons satisfying QTA1 cuts and correlations. Note the slight asymmetric tail in the $+x$ direction corresponds to the M target material allowing photons to convert.

source sizes are both 2 mm in x and 2 mm in y.

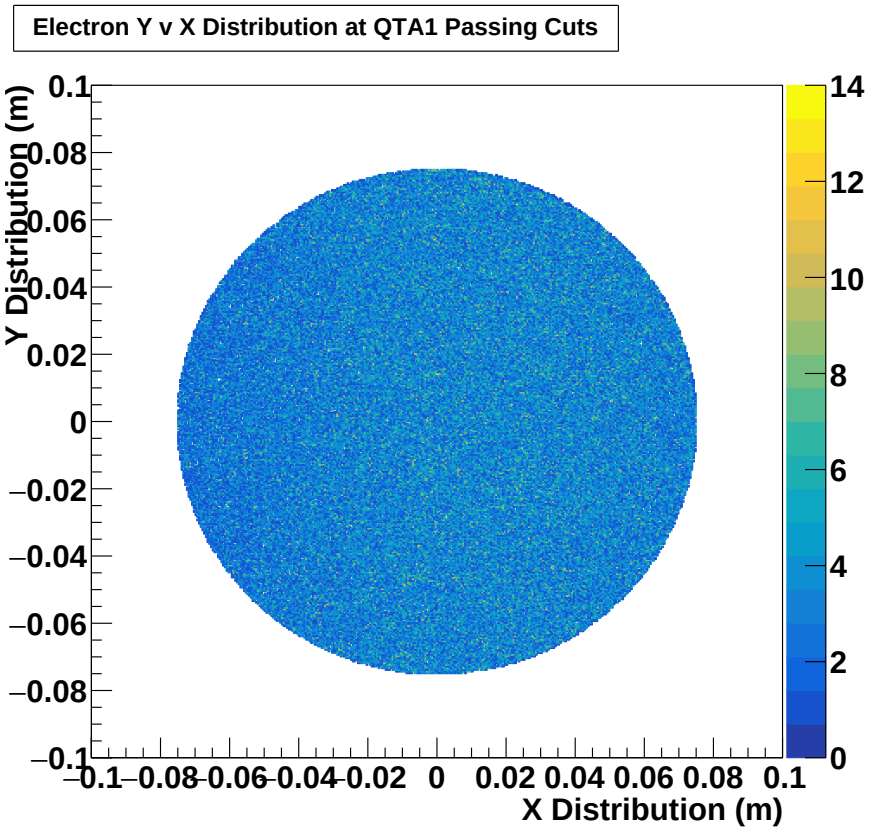

Figure 4.8: Electron/positron distribution entering QTA1

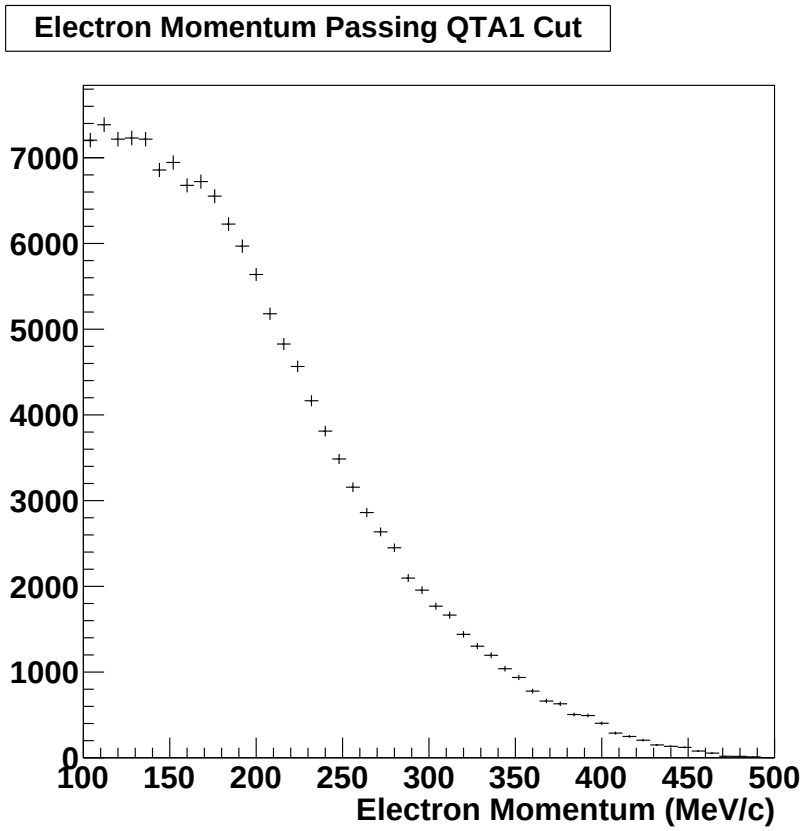

Figure 4.9: Momentum distribution of electrons/positrons passing through the Q1 cuts.

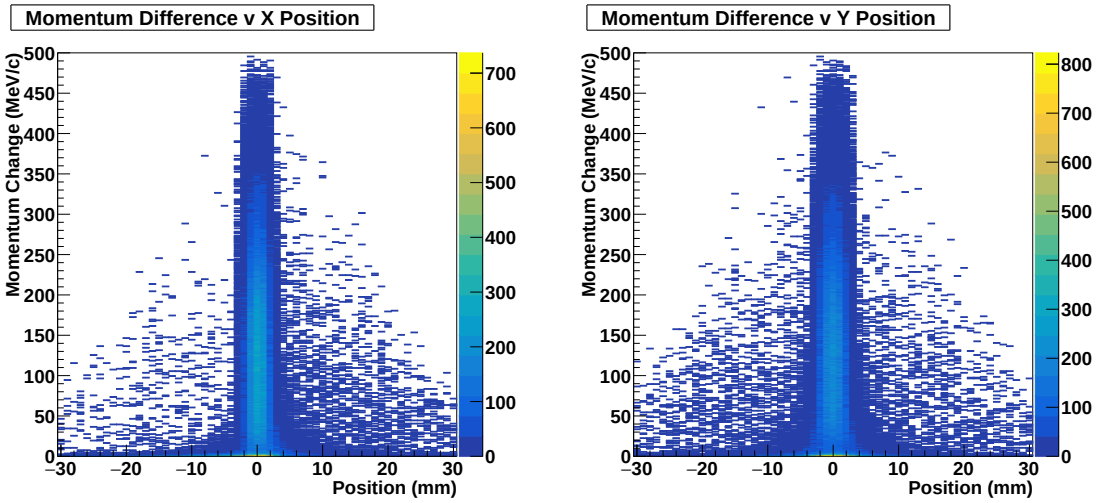

Figure 4.10: ***Left***: Electron momentum in MeV/c as a function of x on the test plane for $y = 0$. ***Right***: Electron momentum in MeV/c as a function of y on the test plane for $x = 0$.

4.2 TURTLE Simulation

PSI has a long history using TURTLE to simulate its beam lines. As a result a description of PiM1 existed at PSI and was provided to MUSE. MUSE updated much of the simulation input in collaboration with Davide Reggiani of PSI, specifically quadrupole magnetic lengths and magnet positions. Several new apertures, including beam pipe and vacuum chambers were also added to the simulation. The TURTLE input deck can be found in Appendix B. The default TURTLE input used muon beam particles, a point like source, and a central momentum of 155 MeV/c. As PiM1 is a magnetic channel, the TURTLE calculations are independent of particle species and momentum, to the extent that the simulation neglects multiple scattering, particle decays in flight, and differences in source size. From our discussion above we know that muons have a different source size than electrons and pions; this is an important point that must be addressed as the default TURTLE calculation used a point source for all particle species. Different source sizes implies that different particles could having differing momenta at the same point in the channel. This correlation must be well understood.

Our ROOT simulation describing the muon source size was used to produce input rays for TURTLE. For a point source TURTLE is capable of generating uniform distributions and running the simulations using the generated distributions. Note that our source size simulations were informed by cuts determined from TURTLE results; those cuts were produced using a large source size with a uniform distribution.

We determined the matrix elements between the production target, the IFP, and the PiM1 target area using a "pencil beam". The size and angular distribution was set to 0 along with the momentum dispersion, and one source parameter was varied at a time to observe the impact on the beam spot at the PiM1 target or the IFP. The first order matrix elements can be seen in Table 4.1 from the production target to the IFP and the PiM1 target. First order matrix elements from the IFP to the PiM1 target can be found in Table 4.2 We note that generally the y coordinate is decoupled from x and δ. We also point out that the 7 cm/% value for the IFP dispersion is reproduced to within 1%, however the magnification between the M target and the PiM1 target is slightly larger than 1. Generally at the IFP the x coordinate reflects the particles momentum, but slightly broadened due to the size of the source. The y coordinate is magnified by an order of magnitude from the production source, but is limited by beam line apertures.

Since we determine these matrix elements experimentally with the GEMs, we required that the particles traversing the beam lines pass through the GEMs. We compare the simulation to data later in Section 5.3.1.

	x_{prod}	x'_{prod}	y_{prod}	y'_{prod}	δ
x_{IFP}	-1.221	-0.036 cm/mr	-0.079	0	7.07 cm/%
x'_{IFP}	-3.37 mr/cm	-0.919	-0.005 mr/cm	0	1.276 mr/%
y_{IFP}	0	0	9.65	-0.009 cm/mr	0
y'_{IFP}	0	0	52.04 mr/cm	0.052	0
x_{targ}	1.47	0	0.325	0	-0.137 cm/%
x'_{targ}	7.31 mr/cm	0.678	0.967 mr/cm	0	-2.01 mr/%
y_{targ}	0	0	-0.319	-0.004 cm/mr	0
y'_{targ}	0	0	273.8 mr/cm	-0.091	0

Table 4.1: First-order PiM1 beam transport matrix elements from TURTLE. The numerical values were calculated using offsets of 1 mm in position, 1 mr in angle, and 0.1% in momentum.

	x_{IFP}	x'_{IFP}	y_{IFP}	y'_{IFP}	δ
x_{targ}	-1.35	-0.05 cm/mr	-0.001	0	9.52 cm/%
x'_{targ}	-4.44 mr/cm	-0.573	-0.003 mr/cm	0	30.3 mr/%
y_{targ}	0	0	0.17	-0.04 cm/mr	0
y'_{targ}	0	0	19.01 mr/cm	0.04	0

Table 4.2: Same as Table 4.1 but from IFP to PiM1 target.

4.2.1 TURTLE simulations with realistic source sizes

We can now compare the expected differences in the electron and pion beams vs the muon beam of PiM1. Fig. 4.11 and 4.12 shows the resulting distributions at the IFP, for point and extended sources. The x distributions are the same, with a full width of 21 cm as the IFP collimator limits the beam. This is larger than the 10 cm width of the IFP GEMs, so when comparing to experiment, the collimator must be narrowed to fit the beam in the GEM active area. The angle range in x' increases by ± 5 mr between the point and extended source. The y distributions increased from ± 2 cm width to ± 5 cm and y' increased from ± 15 mr to ± 30 mr. The shape of the y and y' distributions change as well, with the large source distributions bowing out at larger values. Recall the the y_{IFP} vs y_{prod} matrix element is ≈ 10, so the full size of y_{IFP} represents the largest possible y distribution given the source size of 0.5 cm. The momentum acceptance expands from $\pm 1.5\%$ to about $\pm 2\%$. The expansion of the momentum acceptance comes from the increased source size of the muons, and the slightly different production mechanism for muons than for the point like sources given for electrons and pions. A larger production distribution in x, coupled with a broader momentum distribution, allows for longer tails in the accepted muon momentum.

Fig. 4.13 and 4.14 shows the resulting distributions at the PiM1 GEMs, 35 cm upstream from the target. The muon distribution is wider with larger tails in x and x'. Both distributions are approximately centered in x and x'. The y and y' distributions nearly double in size. The momentum distribution is the same as at the IFP.

Figs. 4.15 and 4.16 show parameter correlations at the GEM chambers for point sources and for muons. The large source size clearly modifies all of the correlations except for the the variation of y' with y, which only broadens slightly. Since we do not measure momentum for each incoming particle, but we do measure each particle's trajectory, we are concerned about momentum variations over the beam spot, and also the difference between the larger μ source and the small e source. We can apply fiducial cuts using the GEMs in both the TOF measurements and in our production data to ensure we understand how momentum relates to trajectory in our analysis. Such a cut limits expansion in the momentum range of the muons. The more extreme trajectories that are more likely to scatter off the target cell walls can also be limited with such a cut.

The point source correlations in Fig. 4.15, show that the momenta are well focused into the central beam spot, with a symmetric tail in the momentum to the physical edges of the beam spot. This leaves the average momentum unchanged, but indicates that a narrow IFP collimator can produce a smaller beam spot in x. The muon source calculations in Fig. 4.16 shows the momentum varies uniformly in y but the variation is opposite that of the x coordinate. We also see the larger

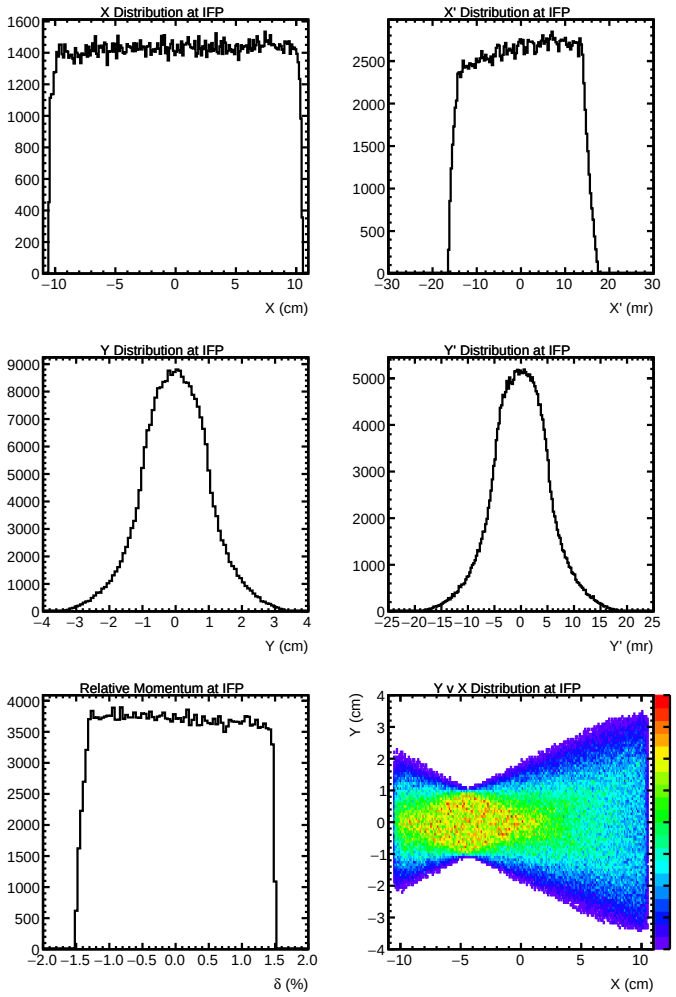

Figure 4.11: Simulations of PiM1 IFP distributions, for a point source. ***Upper Left:*** x distribution. ***Upper Right:*** x' distribution. ***Middle Left:*** y distribution. ***Middle Right:*** y' distribution. ***Lower Left:*** Relative Momentum, δ, distribution. ***Lower Right:*** x v y distribution.

momentum acceptance of the muons occurs at the edge of the beam spot, and that particles of lower and higher momentum appear at different locations in the beam. To remove this momentum bias from our analysis we conclude that we must make symmetric fiducial cuts around the beam spot. This points to a small left/right asymmetry in the momentum extracted from the left and right side of the detector system. This effect will cancel when an average momentum is calculated.

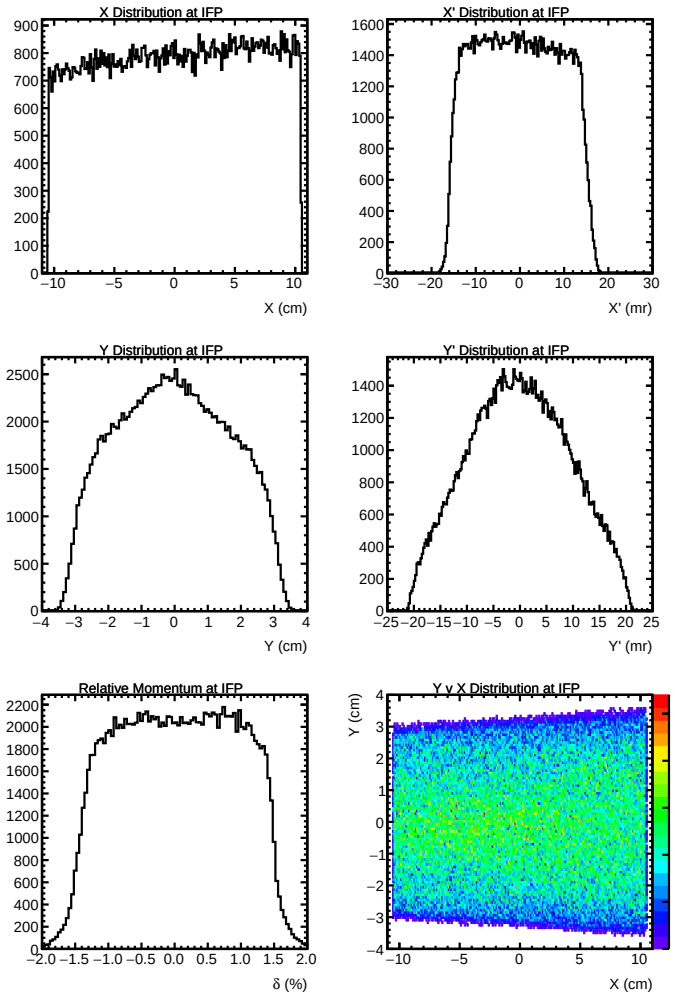

Figure 4.12: Simulations of PiM1 IFP distributions, for a muon source. ***Upper Left:*** x distribution. ***Upper Right:*** x' distribution. ***Middle Left:*** y distribution. ***Middle Right:*** y' distribution. ***Lower Left:*** Relative Momentum, δ, distribution. ***Lower Right:*** x v y distribution.

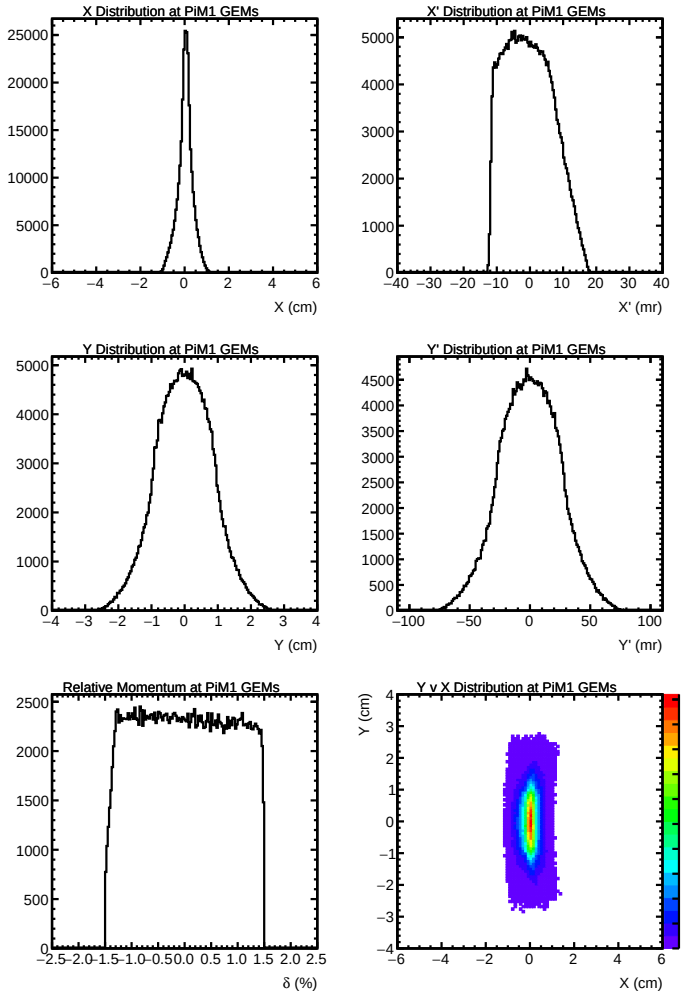

Figure 4.13: Simulations of PiM1 distributions from a point source, except distributions are at the GEM chambers. ***Upper Left:*** x distribution. ***Upper Right:*** x' distribution. ***Middle Left:*** y distribution. ***Middle Right:*** y' distribution. ***Lower Left:*** Relative Momentum, δ, distribution. ***Lower Right:*** x v y distribution.

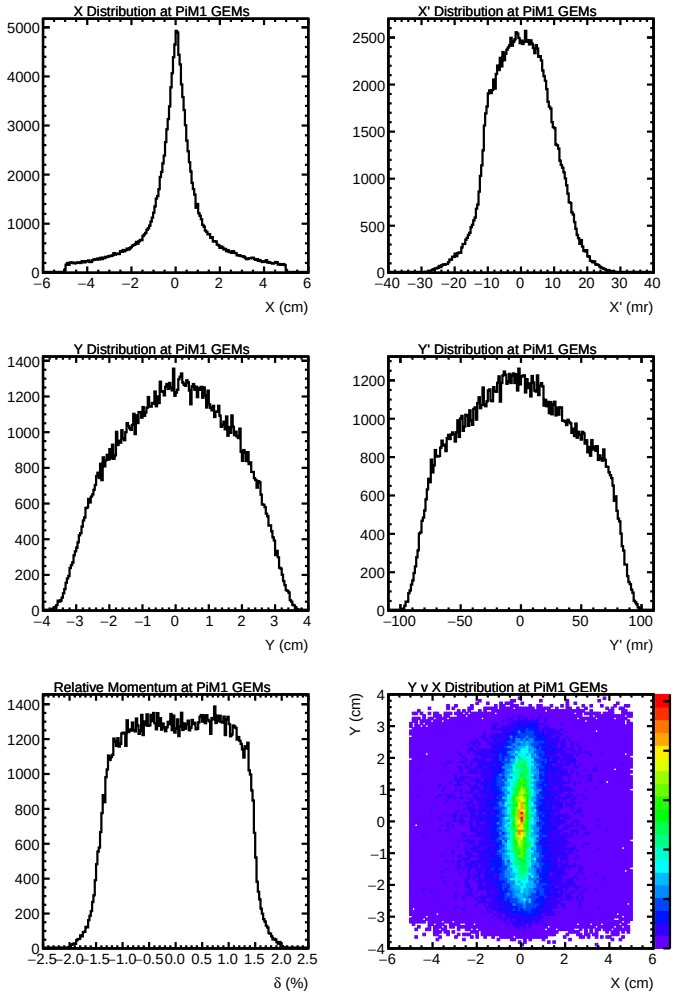

Figure 4.14: Simulations of PiM1 distributions from a muon source, except distributions are at the GEM chambers. ***Upper Left:*** x distribution. ***Upper Right:*** x' distribution. ***Middle Left:*** y distribution. ***Middle Right:*** y' distribution. ***Lower Left:*** Relative Momentum, δ, distribution. ***Lower Right:*** x v y distribution.

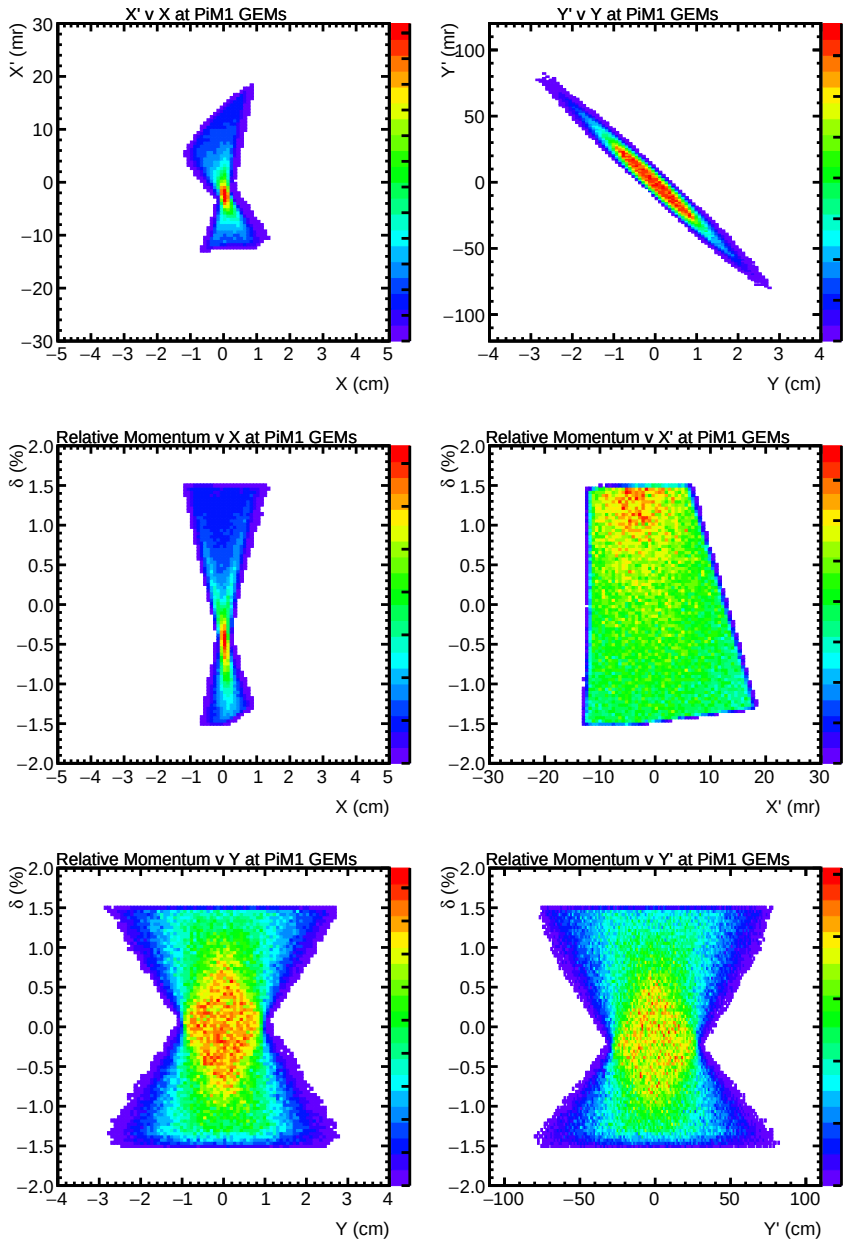

Figure 4.15: Parameter correlations at the GEM chambers, 35 cm upstream of the target, for a point source. Standard TURTLE units of cm, mr, and % are used. ***Upper left***: x' vs x. ***Upper right***: y' vs y. ***Center left***: δ vs x. ***Center right***: δ vs x'. ***Lower left***: δ vs y. ***Lower right***: δ vs y'.

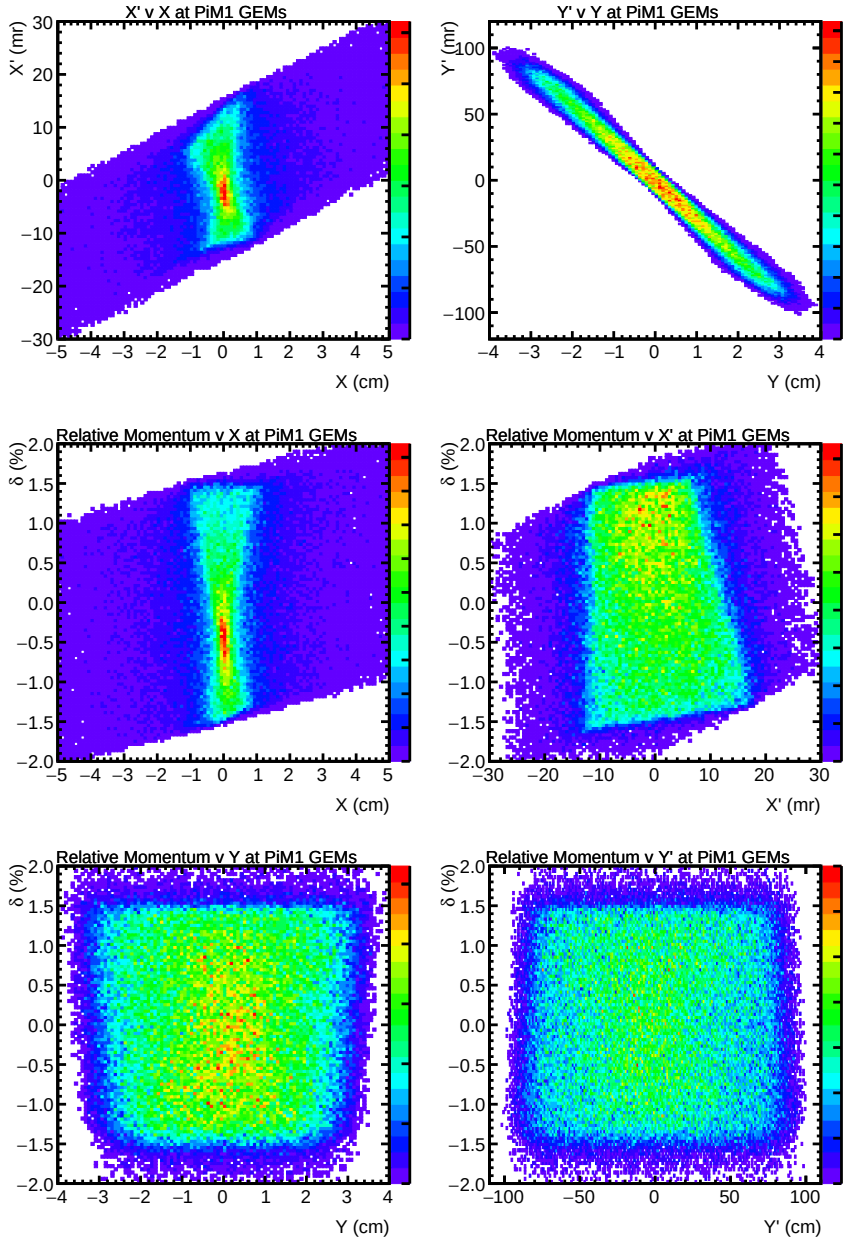

Figure 4.16: Parameter correlations at the GEM chambers, 35 cm upstream of the target, for a muon source source. Standard TURTLE units of cm, mr, and % are used. ***Upper left***: x' vs x. ***Upper right***: y' vs y. ***Center left***: δ vs x. ***Center right***: δ vs x'. ***Lower left***: δ vs y. ***Lower right***: δ vs y'.

4.2.2 TURTLE simulations of using the PiM1 channel as a spectrometer.

In this Section we are going to consider the use of the PiM1 channel as a relative momentum spectrometer. We will demonstrate how particles with different momentum distributions will appear to have differing beam spots at the PiM1 target.

In Sec. 4.2 we displayed the PiM1 matrix elements, which allow us to study the beam momentum through the particle distributions at the target. However this description of the beam line has the production target correlations built-in, we would like to investigate how a more general and random distribution at the IFP impacts the distribution at the target. This random distribution at the IFP allows for a more thorough understanding of how the momentum spread at each point in the IFP affects the distribution at the target. The generated distributions at the IFP match the size of the point distribution beam at the IFP, with $\pm$10.5 cm in x, $\pm$20 mr in x', $\pm$2.5 cm in y, $\pm$15 mr in y', and $\pm$1.5% in δ, but lack correlations between parameters. We consider two cases:

1. The default magnet settings.

2. All quadrupoles after the IFP are turned off, thus only having the particles interacting with the bending dipole.

We show in Fig. 4.17 that the y and y' distributions arising from these simulations are uncorrelated with δ in the case that the quadrupoles are turned on. This is consistent with the matrix elements we have shown, so it is not surprising we continue to see no correlations. For brevity we omit other plots showing no correlation of y or y' with δ.

Fig. 4.18 shows the resulting dispersion of x and x' in the first case, with quads on. The dispersion at the IFP is 7 cm / %, and in the left column we see that if we select x_{IFP} = -7 cm, we see $x_{targ} = 0$ at δ = -1%. Furthermore if we select $x_{IFP} = 0$ cm, we see $x_{targ} = 0$ at $\delta = 0$%, and for $x_{IFP} = 7$ cm, we see $x_{targ} = 0$ at $\delta = +1$%, as expected for the dispersion in the channel.

For each of the 3 choices of x_{IFP}, we see that the dispersion at the target is similar, $\approx$ 9 cm/% which is $\approx$ 30% larger than the IFP dispersion. If we select a narrow region at the IFP experimentally, the position and width in x of the beam spot at the target is a measure of the central momentum and width in momentum at the IFP. If different particles have different average momenta, there is the 9 cm/% dispersion. For particles to differ in momentum by 1% at the IFP they would shift by nearly the full GEM width at the target.

For a beam arising from a point source, a given 1-cm wide region at the IFP corresponds to a 0.14% momentum range, and generates an x_{targ} range of a few cm. The first-order matrix elements presented, $(x_{IFP}/x_{prod}) = -1.225$, along with the $\approx$1.28 cm muon source size in x and a dispersion

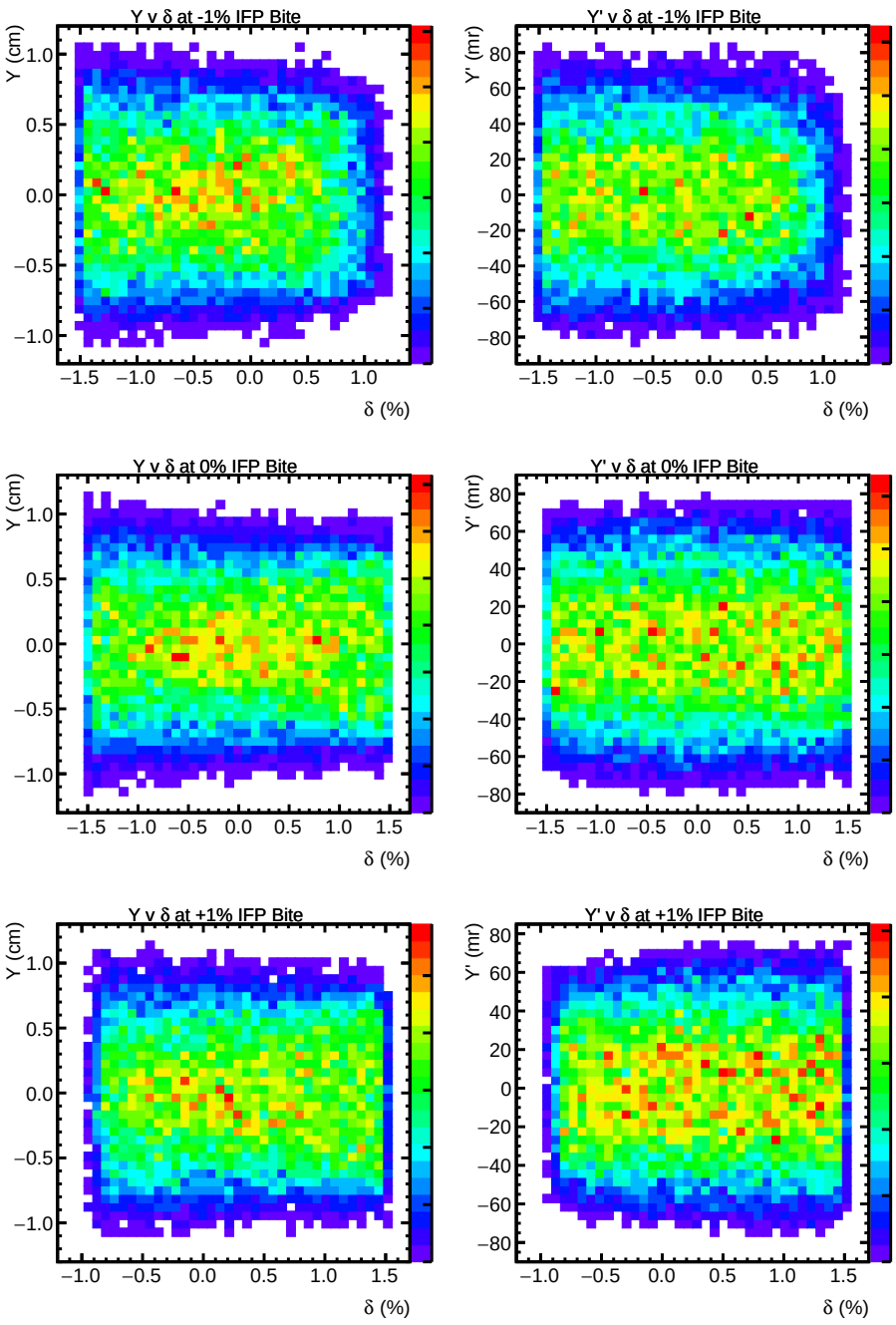

Figure 4.17: ***Left column***: Dispersion in y_{targ} in cm/% for particles from 3 points at the IFP, (upper) x_{IFP} = -7 ± 0.5 cm, (center) 0 ± 0.5 cm, and (lower) 7 ± 0.5 cm. ***Right column***: Dispersion in y'_{targ} in mr/% for particles from the same 3 points at the IFP.

of 7 cm/% suggest that for muons a 1-cm wide slit at the IFP has a momentum range of about 1.28 × 1.225 / 7 cm/% ≈ 0.23%, which is about twice as large as for a point source, and which should make the beam spot about twice as large. The right column of Fig. 4.18 shows similar effects for

the angle x', with a dispersion in angle of $\approx$ 25 mr / %, but the range of δ covered is larger for a fixed x' than for a fixed x, so x is a more sensitive quantity.

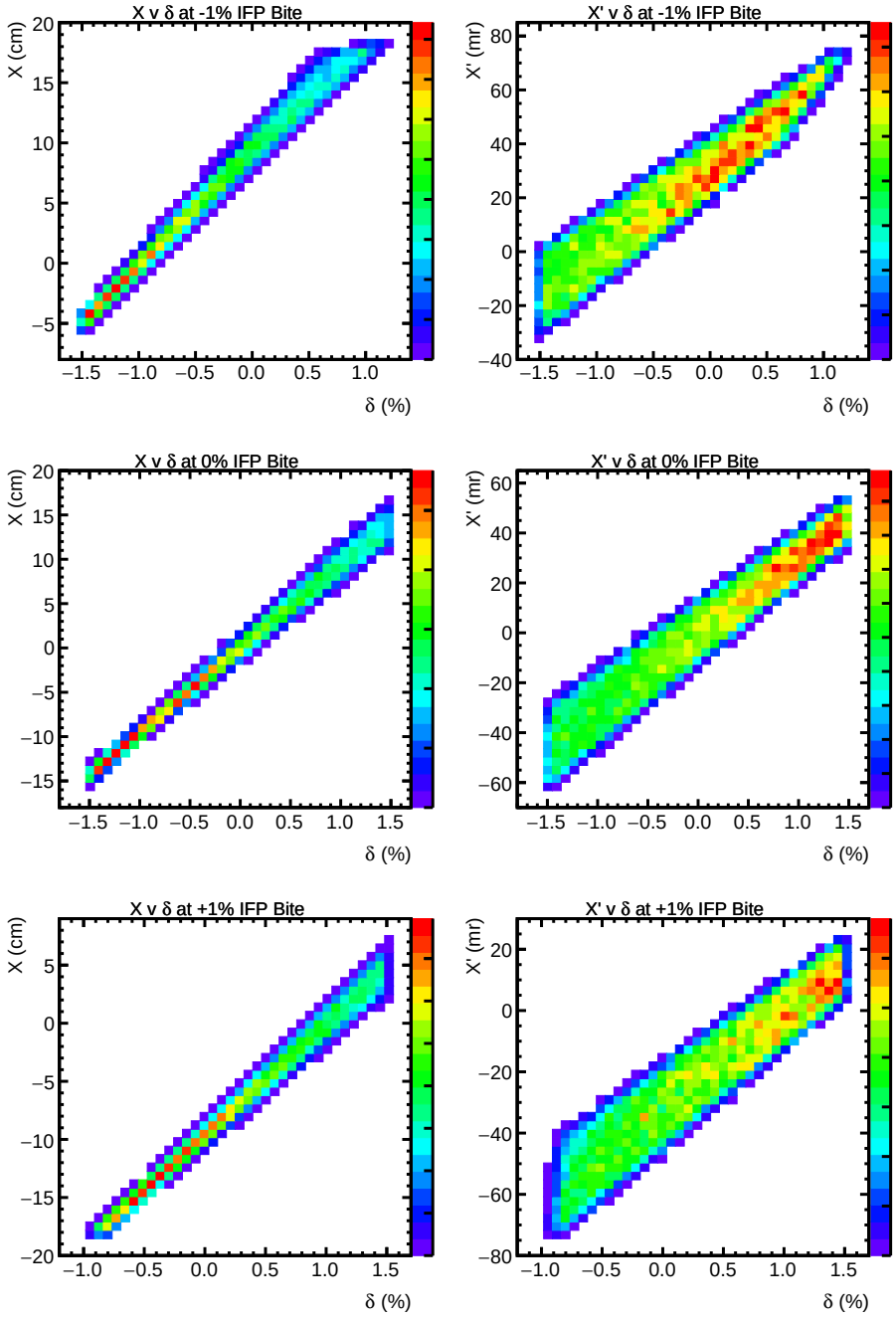

Figure 4.18: ***Left column***: Dispersion in x_{targ} in cm/% for particles from 3 points at the IFP, (upper) x_{IFP} = -7 $\pm$ 0.5 cm, (center) 0 $\pm$ 0.5 cm, and (lower) 7 $\pm$ 0.5 cm. ***Right column***: Dispersion in x'_{targ} in mr/% for particles from the same 3 points at the IFP.

Now we move to case 2, with the quadrupoles turned off to see their impact on the beam. Figure

4.19 shows the resulting dispersion in this second case, with quads off. The correlations are similar to those of Fig. 4.18, but generally broader. The key difference is that the correlation between x and δ has grown much broader. That the distributions in these two cases are not much different, and that the distributions do not spread much in x even with the quads off, over the flight path from the IFP to the GEMs, indicates that there is significant focusing of the distributions from the curvature at the entrance and exit of the ASAM12 dipole pole faces. This demonstrates that measuring the beam properties with quadrupoles turned off can also give direct access to magnetic channel properties. The wider x and δ correlation allows us to directly see how particles of differing momentum appear at different places at the target GEMs.

As a check of whether our conclusions are affected by too small a source distribution, the calculations were redone using the larger source size of the muon distribution beam at the IFP. The large source used ± 10.5 cm in x, ± 27 mr in x', ± 5 cm in y, ± 35 mr in y', and $\pm 2\%$ in δ, and again lacked correlations between parameters.

Fig. 4.20 shows the resulting dispersions at the target for the case with quadrupoles on. Comparing these results to Fig. 4.18, the range of the correlations is larger – there is more momentum acceptance leading to a broader beam spot – but otherwise the correlations are unchanged.

To summarize, when taking measurements with a narrow collimator opening, the width of the beam spot in x and x' reflects the range of momentum of the particles within the collimator opening. Particles with a broader momentum range, for the same point at the IFP, will have a broader beam spot at the target. If different particles have different average momenta, the centers of their distributions will be shifted, which should be easy to see with measurements of the beam with quadrupoles turned off. The dispersion is about 9 cm/% in x and 25 mr / % in x' with the quads on, and somewhat less with the quads off. A 0.1% relative average momentum measurement requires determining the relative centers of the distributions to 9 mm or 2.5 mr, which falls well within the resolution of our GEM chambers.

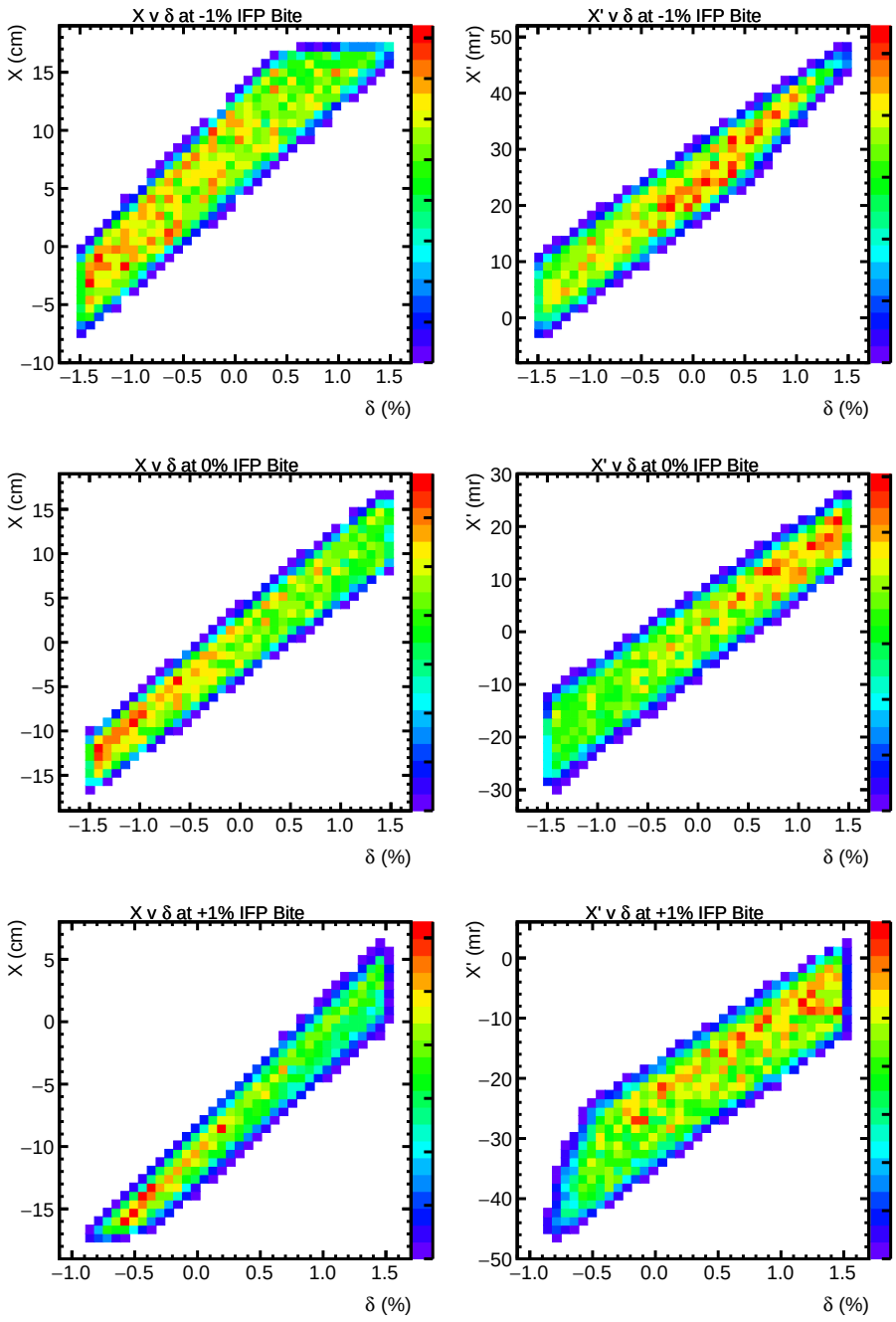

Figure 4.19: ***Left column***: Dispersion in x_{targ} in cm/% for particles from 3 points at the IFP with quadrupoles turned off, (upper) x_{IFP} = -7 ± 0.5 cm, (center) 0 ± 0.5 cm, and (lower) 7 ± 0.5 cm. ***Right column***: Dispersion in x'_{targ} in mr/% for particles from the same 3 points at the IFP.

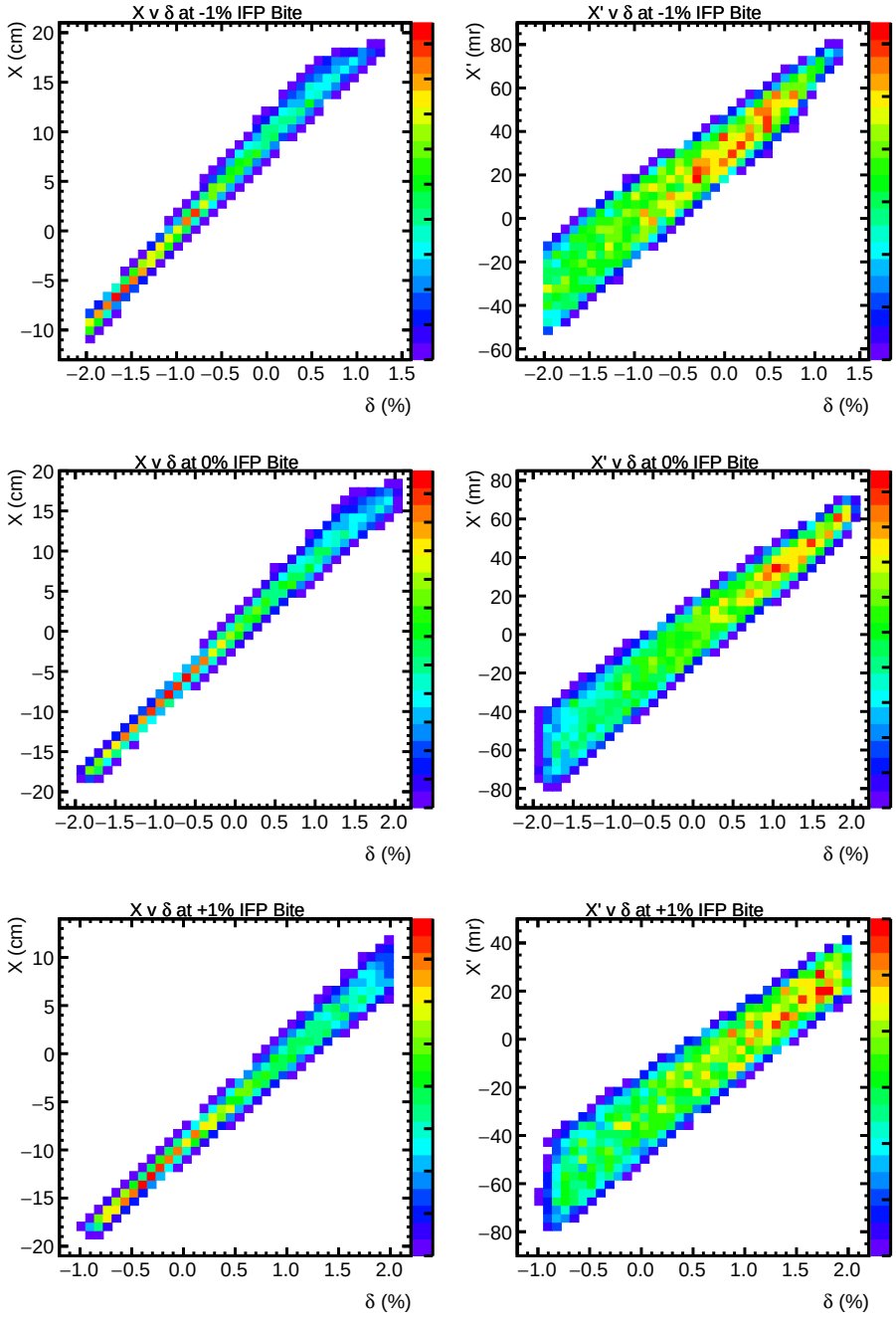

Figure 4.20: Dispersion distributions starting from a larger source distributions at the IFP, reflecting the larger range of angles and positions at the IFP generated by a muon source at the M target. ***Left column***: Dispersion in x_{targ} in cm/% for particles from 3 points at the IFP, (upper) x_{IFP} = -7 ± 0.5 cm, (center) 0 ± 0.5 cm, and (lower) 7 ± 0.5 cm. ***Right column***: Dispersion in x'_{targ} in mr/% for particles from the same 3 points at the IFP.

4.3 G4beamline vs TURTLE comparison

The G4beamline [39] simulation software is specifically designed to simulate particles traveling down beam lines using the GEANT4 [1] toolkit. G4beamline and TURTLE fundamentally differ in the way that they propagate particles through electromagnetic fields. TURTLE comes from a well developed set of beam line codes written in FORTRAN that use matrix algebra to act on a vector $X = (x, x', y, y', \ell, \delta)$ that represents the particle's position and kinematics, with matrices that represent the electromagnetic fields. It would be possible to represent the entirety of the PiM1 beam line as one matrix that is the product of all the individual matrices representing the magnets and drifts between them. However such a matrix would not include any description of a beam particle interacting with matter, such as multiple scattering on apertures in the beam line. As such we represent each magnet with its own matrix representation and include apertures in the beam line. In order to see clearer correlations we often do not include particle decays.

In contrast, GEANT4 and therefore G4beamline determine propagation through electromagnetic fields in short individual "steps". The force is then calculated and applied to the beam particle which is then propagated to the next step. G4beamline requires magnetic field maps for each magnetic element. For a simple quadrupole in PiM1, it is possible to describe the geometry of the magnet and include the field strength in such a way that G4beamline can calculate the field. The dipoles in the channel are more complicated than the models available in G4beamline, as the magnetic pole faces are curved. As this geometry is unavailable in G4beamline, a field map was produced, though still for a simpler dipole geometry than that used in TURTLE, and fed into the simulation. The geometry of the dipoles is shown in Fig. 4.21.

In principle it should be sufficient to simulate the PiM1 channel with either TURTLE or G4beamline alone. Since the two codes implement the magnetic channel slightly differently, with different techniques and approaches, the comparison between the two simulations provides an estimate of the uncertainty in the calculations.

As both codes represent the beam line in slightly different formalisms, a good cross check to show that they represent the beam line in a consistent manner is to calculation their transmission efficiencies. The efficiencies can be seen in Tables 4.3 and 4.4. We see that for the 2018 fields used to take data both G4beamline and TURTLE are of the same order of magnitude in their efficiency for transmitting a particle down the beam line. TURTLE has a higher transmission efficiency for a point source, while G4beamline has a higher transmission efficiency for a muon source.

The G4beamline description of the beamline is shown in Fig. 4.22 along with 5000 μ^+ particles traversing the beam line. The input deck is shown in Appendix C. To illustrate the agreement

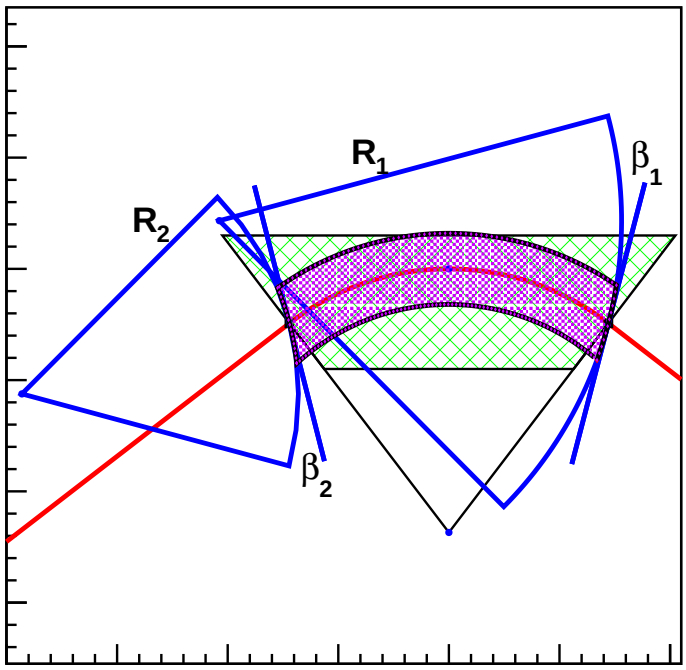

Figure 4.21: Diagram showing the pole face angles and radii of curvature for the first (ASM11) dipole. The red line represents the path particles travel through the dipole. The purple shaded region is the region containing the magnetic field. The green cross hatched region indicates where material in the dipole is located. β_1 and β_2 are lines tangent to the dipole face, while the curved lines R_1 and R_2 show the actual curved faces of the dipole. The second (ASM12) dipole is a mirror image.

Transmission Efficiencies	Point Source (%)	Muon Source (%)
IFP	0.15 (0.09)	0.09 (0.14)
PiM1 Target	0.15 (0.08)	0.09 (0.12)

Table 4.3: Transmission efficiencies for TURTLE and G4beamline (in parentheses) for the summer 2018 setup. Note that in this setup the FS-11 jaws are closed to ± 1 cm in x and y and the IFP collimator is set to a 1 cm width. This reduces overall transmission by two orders of magnitude.

between the TURTLE and G4beamline simulations, we compared simulations using the same input distributions, both point-like and the larger muon source distribution. We also included a copper collimator at the IFP and the FS-11 jaws used to control beam flux. These apertures are included in TURTLE in the default simulation.

Transmission Efficiencies	Point Source (%)	Muon Source (%)
IFP	41.14 (28.07)	32.37 (41.19)
PiM1 Target	41.11 (27.97)	23.53 (40.59)

Table 4.4: Same as Table 4.3 but for the default setup with FS-11 set to ±8 cm and the IFP collimator set to a width of 21 cm.

We placed several virtual detectors, shown as magenta lines in Fig. 4.22, to study the spatial distributions and correlations at various places along the beam line. The distributions are shown in Figs. 4.23 to 4.34. We show only distributions before and after the ASM11 and ASM12 dipoles, at the IFP, and at the PiM1 target. The TURTLE simulation was scaled to the same height as the G4beamline simulation for ease of visualization.

Before entering the first bending dipole, the point source distributions agree well between the two simulations as shown in Figs. 4.23. The notable exception is TURTLE shows a wider y' distribution. For the large muon source shown in Fig. 4.24 TURTLE predicts a narrower y distribution, this is due to the energy loss differences between the two simulations. There are also differences in the distributions due to the differences in how the simulations handle the focusing quadrupoles upstream of the first dipole.

The dipole then broadens the TURTLE y' distributions but not the G4beamline y' in Fig. 4.25. In Fig. 4.26 we see that the larger y distributions are brought under control, but not to full agreement, at the expense of the agreement in y'. There is a bite taken out of the beam in the negative side of the x coordinate in G4beamline; this is due to nonphysical events that do not properly bend through the ASM11 dipole. These events do not traverse the rest of the beam line nor make it to the PiM1 target.

The IFP is located almost half-way between the first dipole and the second dipole. The distributions for a point source at the IFP appear quite well matched as seen in Fig. 4.27. For the muon source in Fig. 4.28 we see that TURTLE predicts a wider y but smaller y' distribution.

After exiting the IFP, the beam passes through another set of quadrupole magnets and the ASM12 dipole magnet before reaching the PiM1 target. The distributions immediately before ASM12 show qualitatively good agreement for the point source (Fig. 4.29). The muon source figure shows TURTLE predicting narrower y distributions (Fig. 4.30). After the ASM12 dipole we see in both Fig. 4.31 and 4.32 a large shoulder in G4beamline in x. This shoulder is caused by non-physical events in the beam line that do not propagate to the PiM1 target. As the ASM12 field map

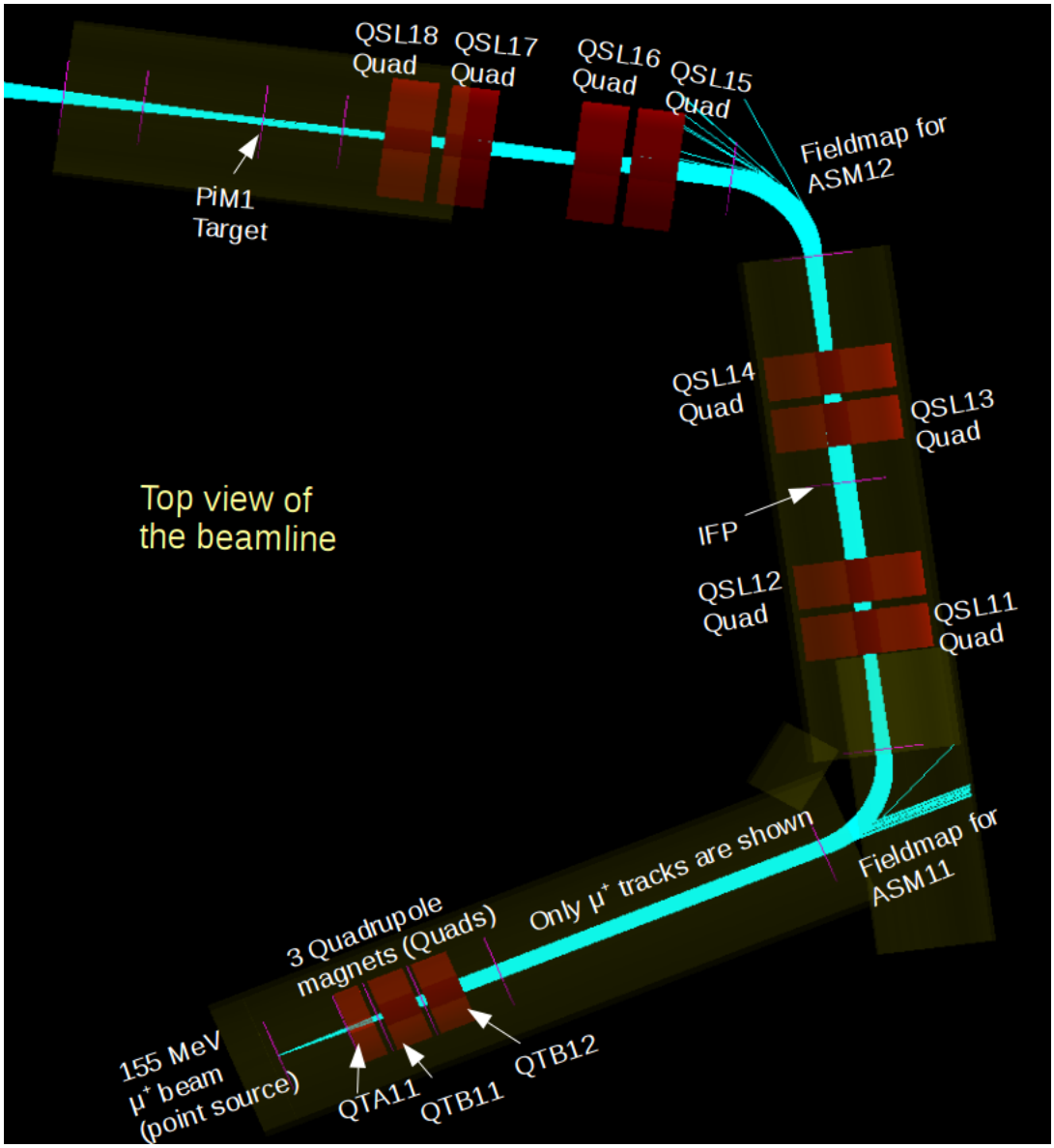

Figure 4.22: The MUSE G4beamline model of the PiM1 channel. This image shows 5000 μ^+ events from a point source (described in the text). The magenta lines correspond to virtual detectors. The almost transparent cylinders enclosing the beam line correspond to shields, which eliminate particles that are scattered outside of the beam line.

description improves, these shoulders will disappear. The shoulder is larger for the muon source because the more extended distributions have access to a larger region of the dipole and more events interact in a non-physical way with the dipole. Again we see TURTLE predicts wider y distributions.

At the PiM1 target region we see that for a point source TURTLE brings the beam to a focus and now predicts a narrower y and x distribution than G4beamline (Fig. 4.33 and 4.34). For the

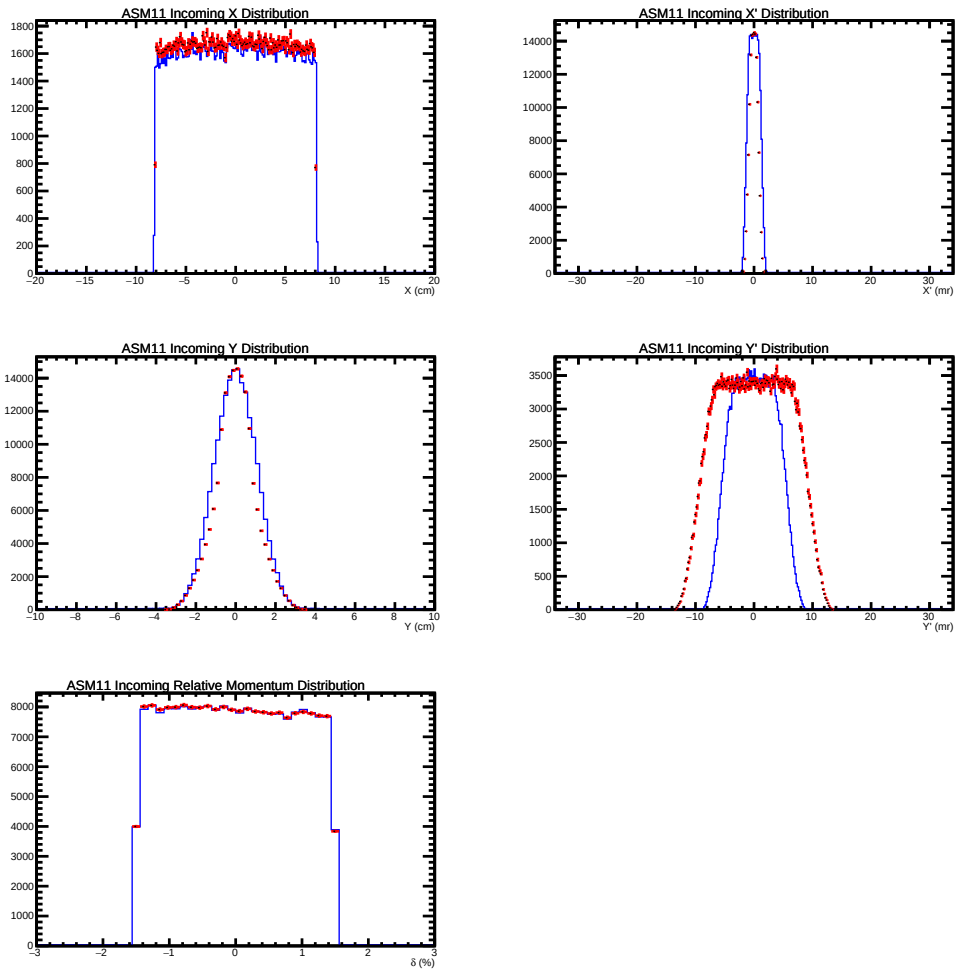

Figure 4.23: The distributions that enter ASM11 using a point source for both TURTLE and G4beamline. TURTLE histograms are shown in red and G4beamline histograms are in blue. ***Upper Left:*** x distribution. ***Upper Right:*** x' distribution. ***Middle Left:*** y distribution. ***Middle Right:*** y' distribution. ***Lower Left:*** Relative Momentum, δ, distribution.

muon source we see TURTLE and G4beamline predicts long tails in x at the target. TURTLE predicts slightly narrower x and y distributions but a wider y' distribution.

Based on the figures shown we conclude there is qualitatively good agreement between both simulations. The field maps for both ASM11 and ASM12 will be improved for future simulations which will hopefully resolve the discrepancies in the simulations. The simulations will be compared to data at the IFP and target in Sec. 5.2. Generally speaking we note that G4beamline predicts larger distributions in y than TURTLE when entering and exiting ASM11 and when entering ASM12. However the opposite is true concerning the y' distributions. These differences are due entirely to

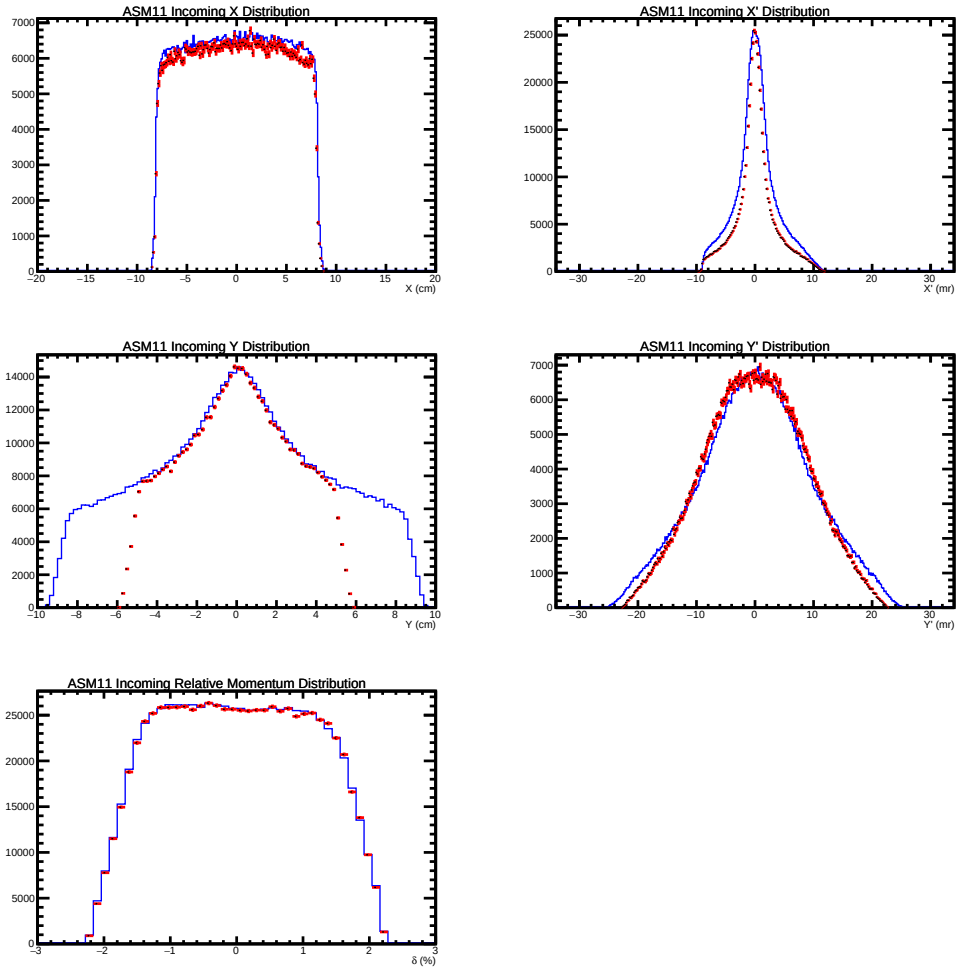

Figure 4.24: The distributions that enter ASM11 using a muon source for both TURTLE and G4beamline. TURTLE histograms are shown in red and G4beamline histograms are in blue. ***Upper Left:*** x distribution. ***Upper Right:*** x' distribution. ***Middle Left:*** y distribution. ***Middle Right:*** y' distribution. ***Lower Left:*** Relative Momentum, δ, distribution.

the description of the focusing quadrupoles in the two simulations.

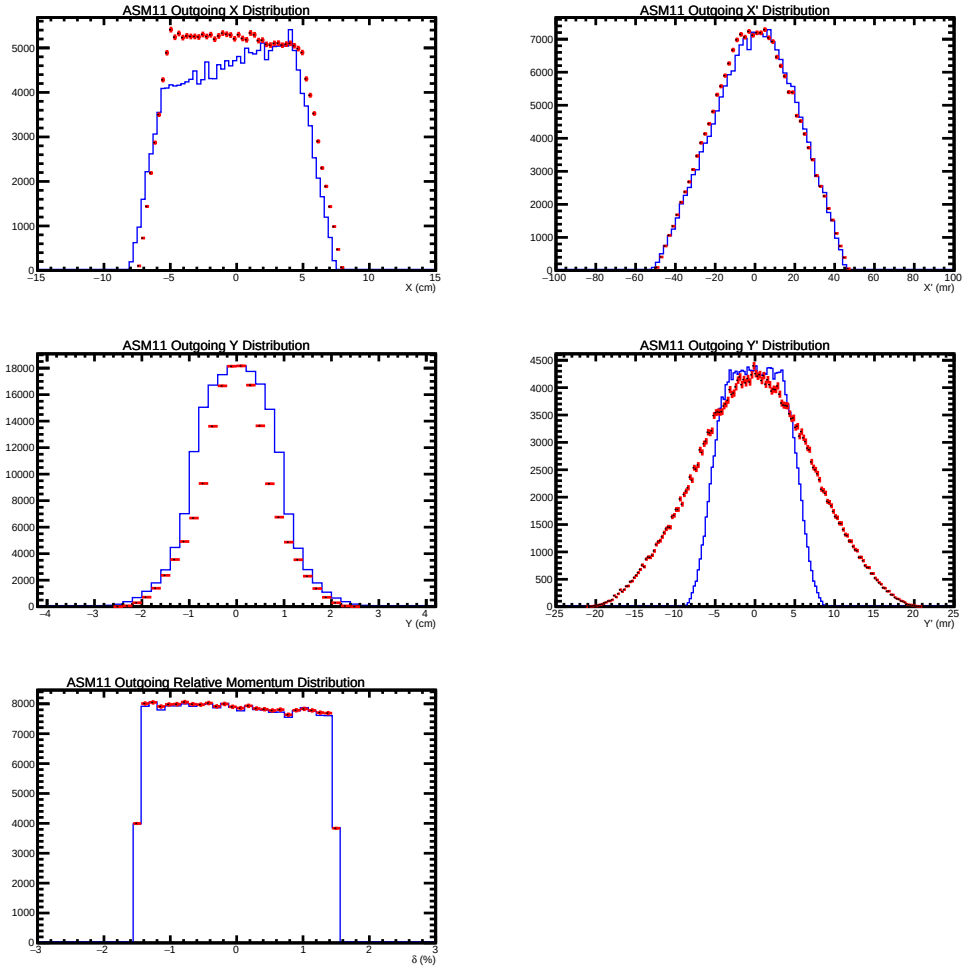

Figure 4.25: The distributions that leave ASM11 using a point source for both TURTLE and G4beamline. TURTLE histograms are shown in red and G4beamline histograms are in blue. ***Upper Left:*** x distribution. ***Upper Right:*** x' distribution. ***Middle Left:*** y distribution. ***Middle Right:*** y' distribution. ***Lower Left:*** Relative Momentum, δ, distribution.

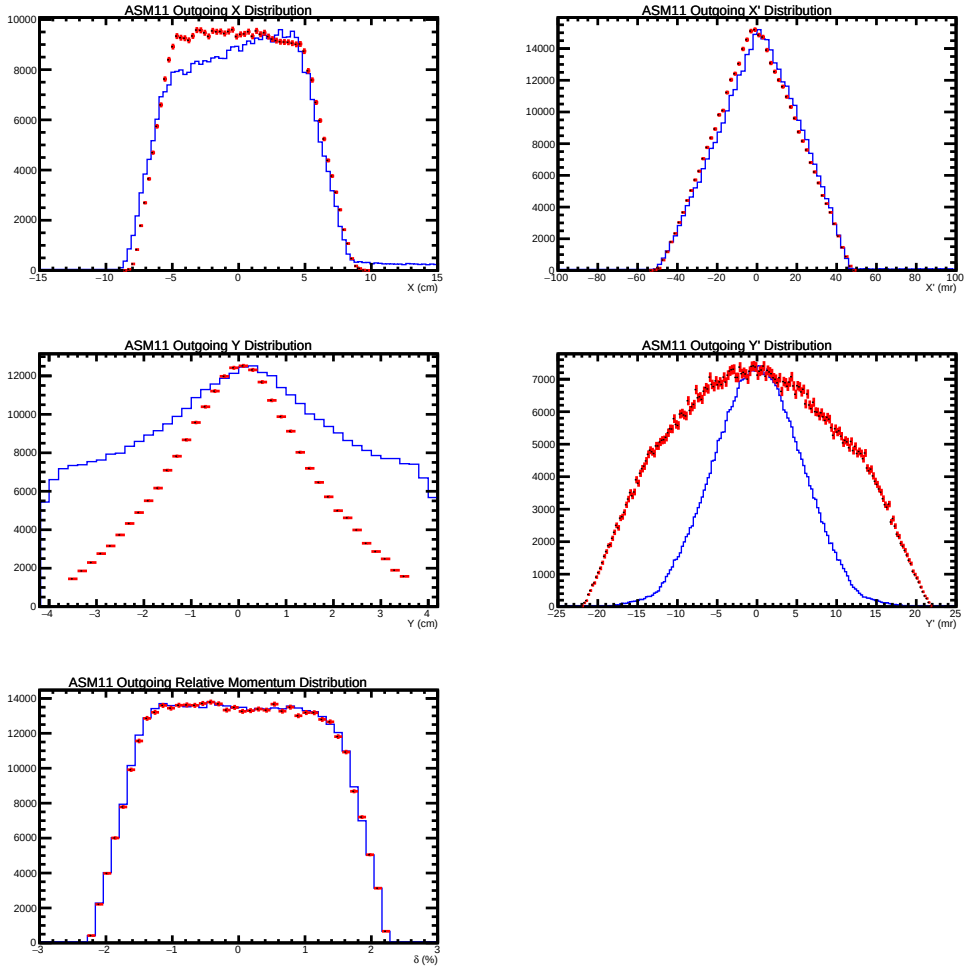

Figure 4.26: The distributions that leave ASM11 using a muon source for both TURTLE and G4beamline. TURTLE histograms are shown in red and G4beamline histograms are in blue. ***Upper Left:*** x distribution. ***Upper Right:*** x' distribution. ***Middle Left:*** y distribution. ***Middle Right:*** y' distribution. ***Lower Left:*** Relative Momentum, δ, distribution.

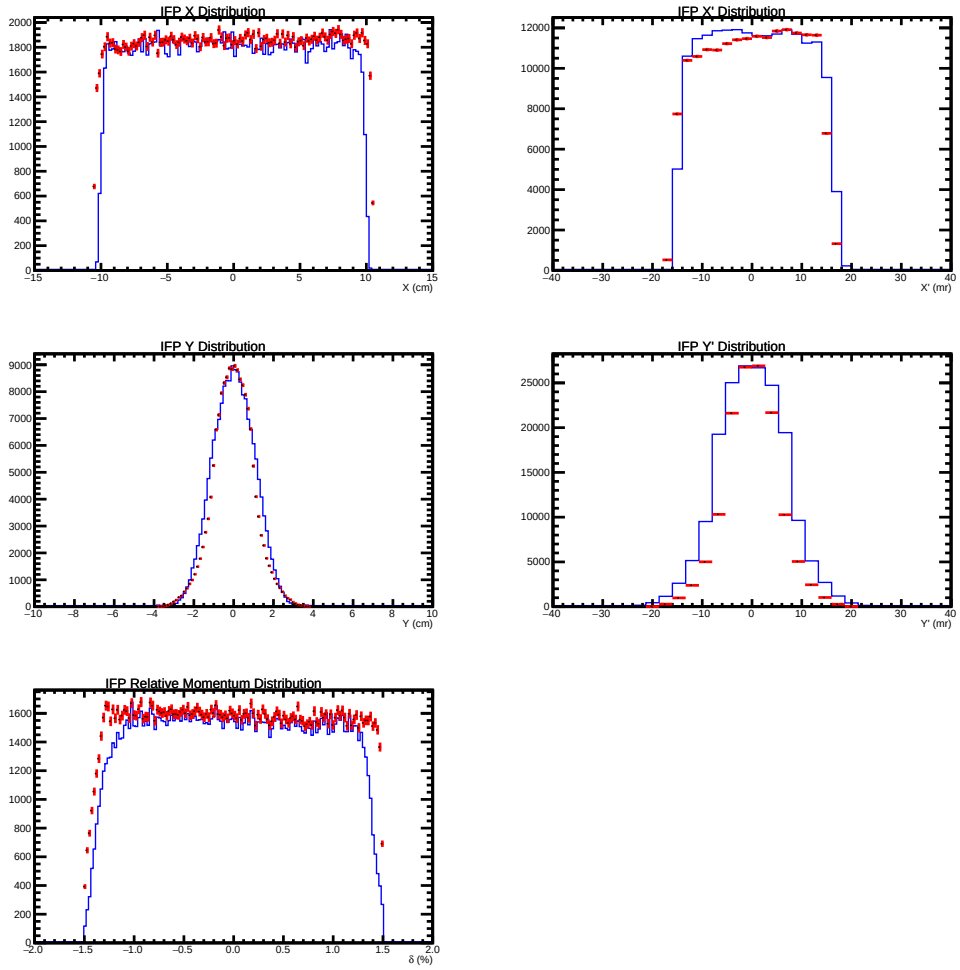

Figure 4.27: The distributions at the IFP using a point source for both TURTLE and G4beamline. TURTLE histograms are shown in red and G4beamline histograms are in blue. ***Upper Left:*** x distribution. ***Upper Right:*** x' distribution. ***Middle Left:*** y distribution. ***Middle Right:*** y' distribution. ***Lower Left:*** Relative Momentum, δ, distribution.

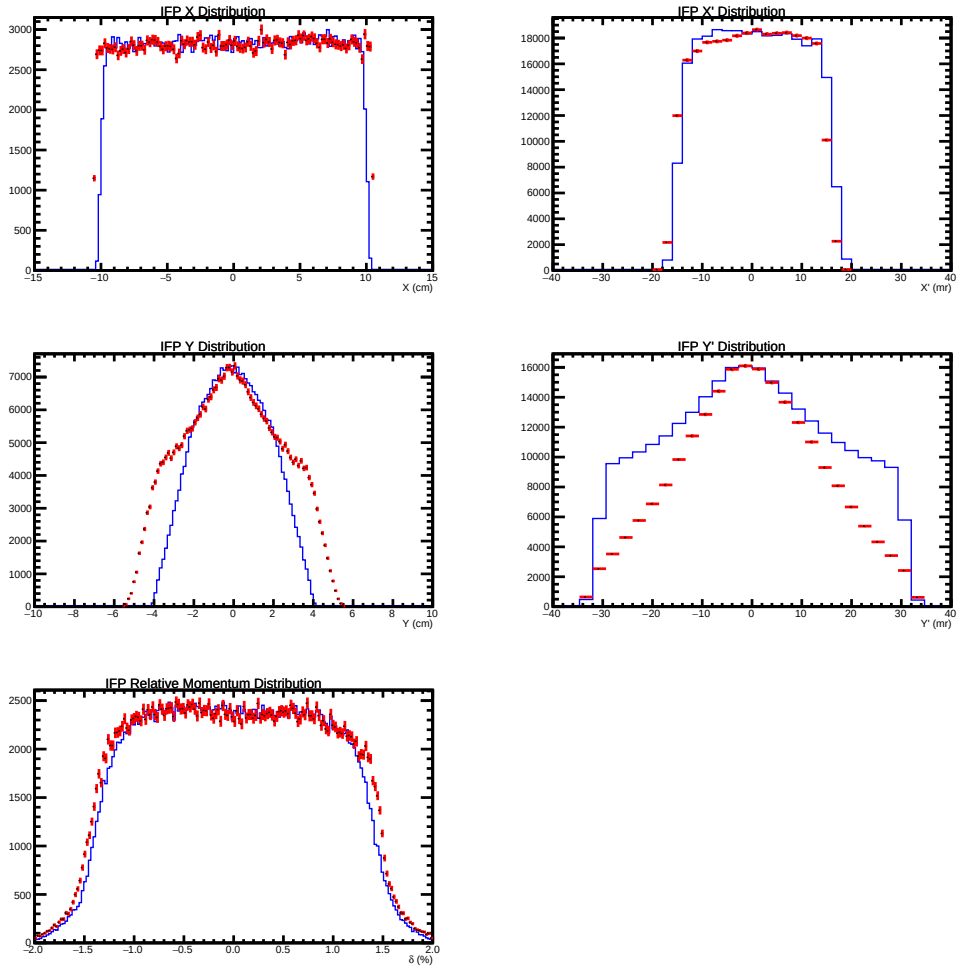

Figure 4.28: he distributions at the IFP using a muon source for both TURTLE and G4beamline. TURTLE histograms are shown in red and G4beamline histograms are in blue. ***Upper Left:*** x distribution. ***Upper Right:*** x' distribution. ***Middle Left:*** y distribution. ***Middle Right:*** y' distribution. ***Lower Left:*** Relative Momentum, δ, distribution.

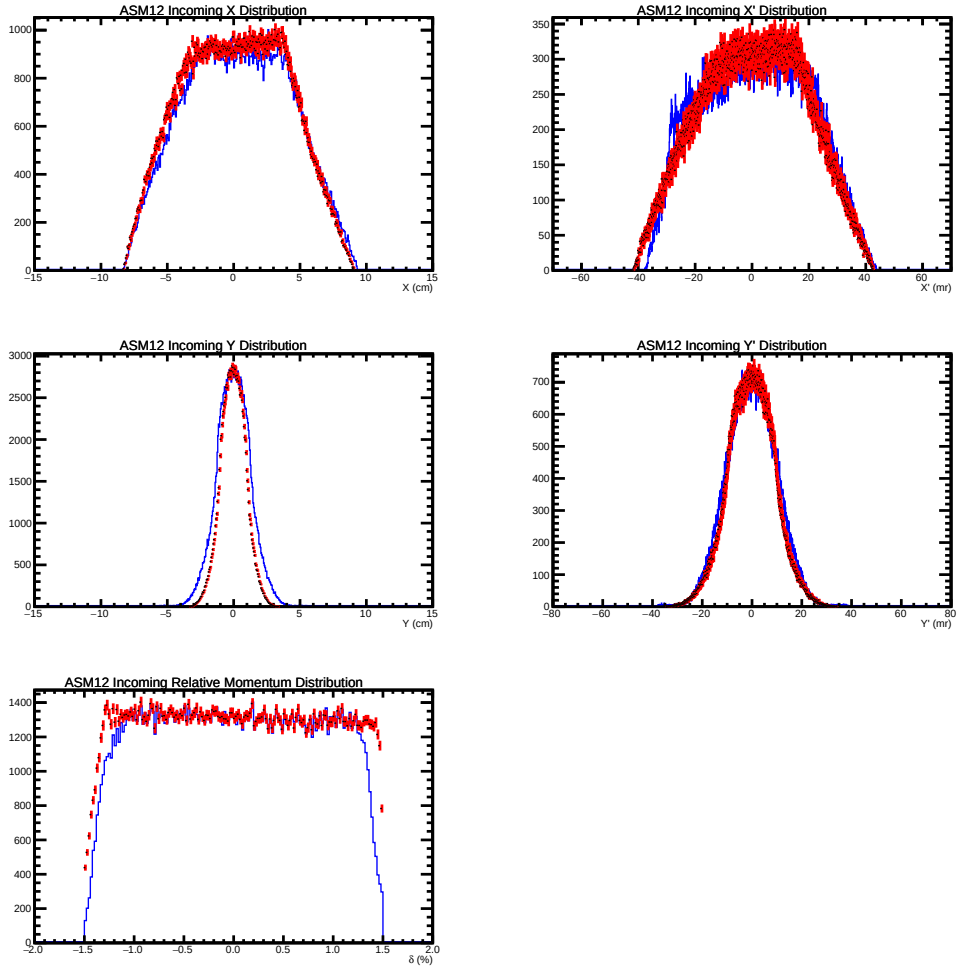

Figure 4.29: The distributions that enter ASM12 using a point source for both TURTLE and G4beamline. TURTLE histograms are shown in red and G4beamline histograms are in blue. ***Upper Left:*** x distribution. ***Upper Right:*** x' distribution. ***Middle Left:*** y distribution. ***Middle Right:*** y' distribution. ***Lower Left:*** Relative Momentum, δ, distribution.

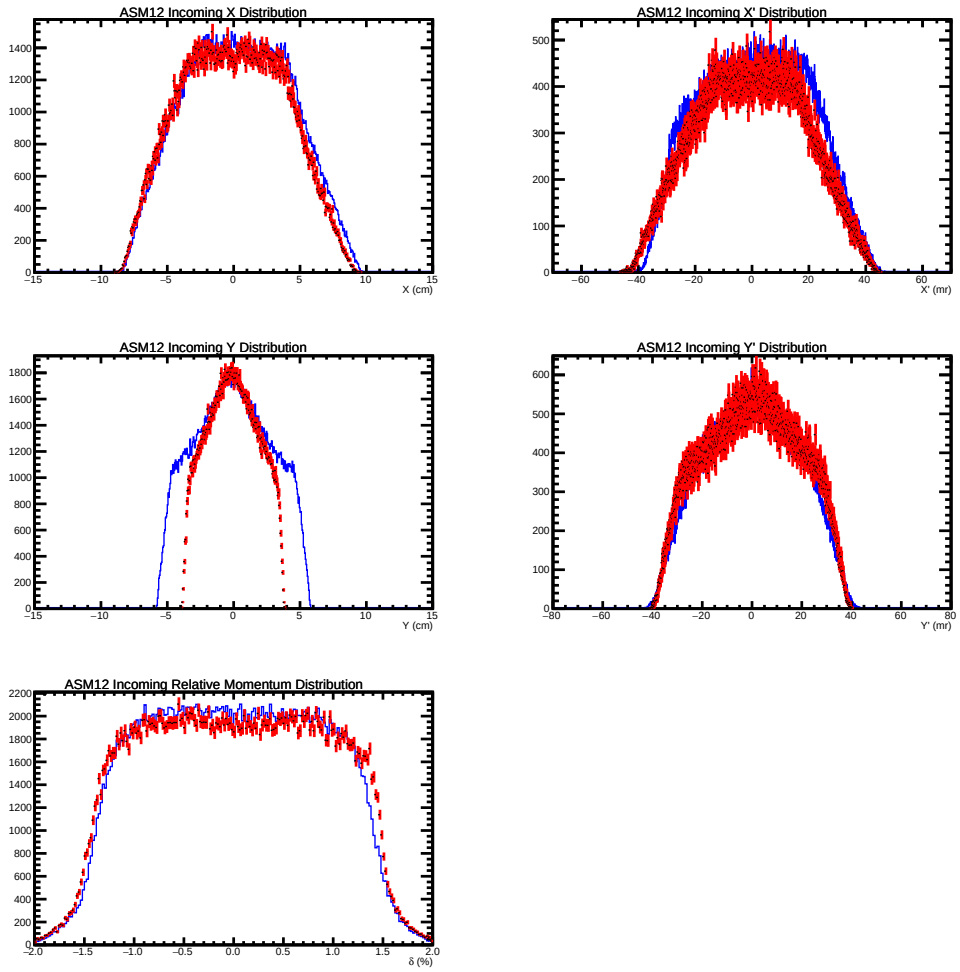

Figure 4.30: The distributions that enter ASM12 using a muon source for both TURTLE and G4beamline. TURTLE histograms are shown in red and G4beamline histograms are in blue. ***Upper Left:*** x distribution. ***Upper Right:*** x' distribution. ***Middle Left:*** y distribution. ***Middle Right:*** y' distribution. ***Lower Left:*** Relative Momentum, δ, distribution.

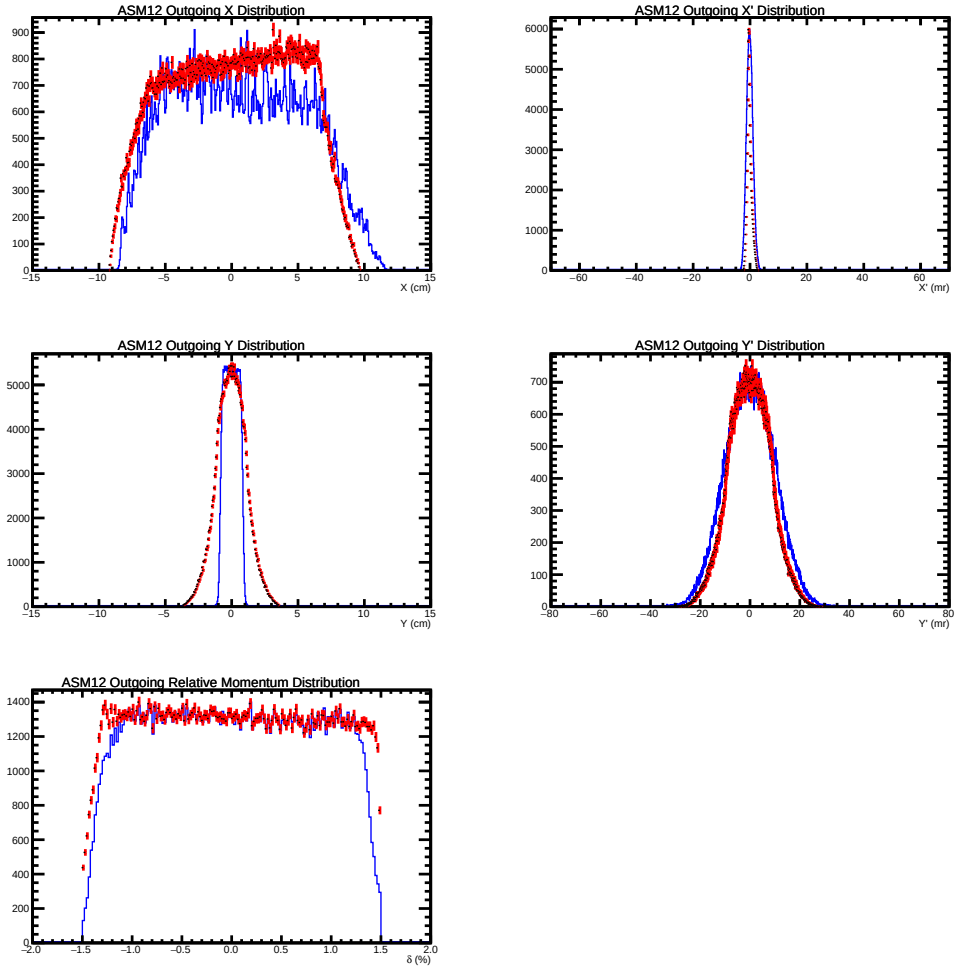

Figure 4.31: The distributions that leave ASM12 using a point source for both TURTLE and G4beamline. TURTLE histograms are shown in red and G4beamline histograms are in blue. ***Upper Left:*** x distribution. ***Upper Right:*** x' distribution. ***Middle Left:*** y distribution. ***Middle Right:*** y' distribution. ***Lower Left:*** Relative Momentum, δ, distribution.

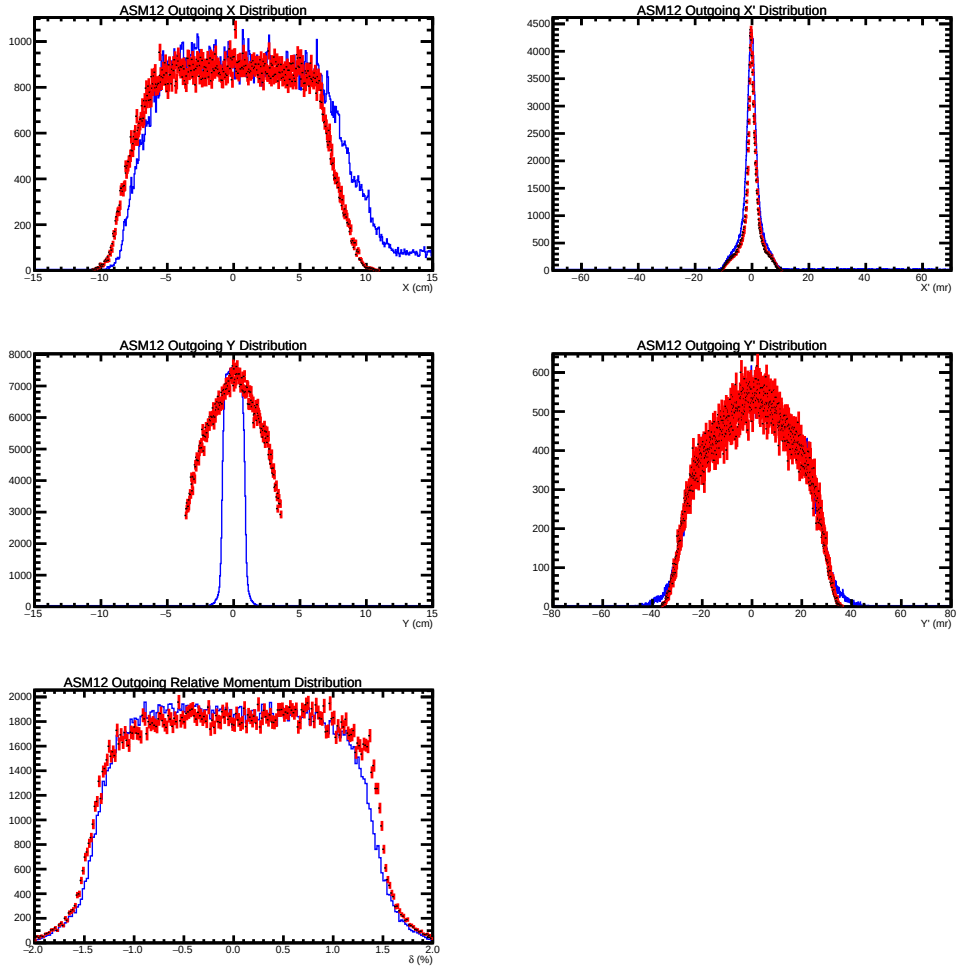

Figure 4.32: The distributions that leave ASM12 using a muon source for both TURTLE and G4beamline. TURTLE histograms are shown in red and G4beamline histograms are in blue. ***Upper Left:*** x distribution. ***Upper Right:*** x' distribution. ***Middle Left:*** y distribution. ***Middle Right:*** y' distribution. ***Lower Left:*** Relative Momentum, δ, distribution.

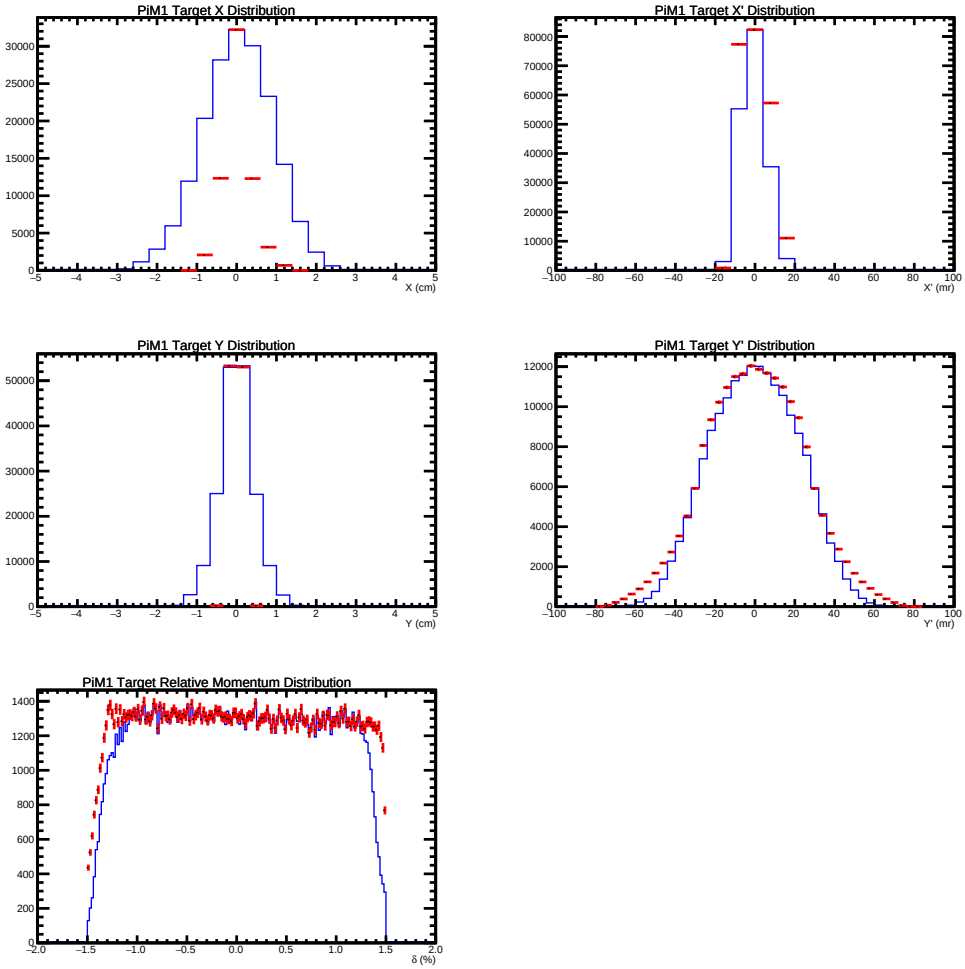

Figure 4.33: The distributions at the PiM1 target using a point source for both TURTLE and G4beamline. TURTLE histograms are shown in red and G4beamline histograms are in blue. ***Upper Left:*** x distribution. ***Upper Right:*** x' distribution. ***Middle Left:*** y distribution. ***Middle Right:*** y' distribution. ***Lower Left:*** Relative Momentum, δ, distribution.

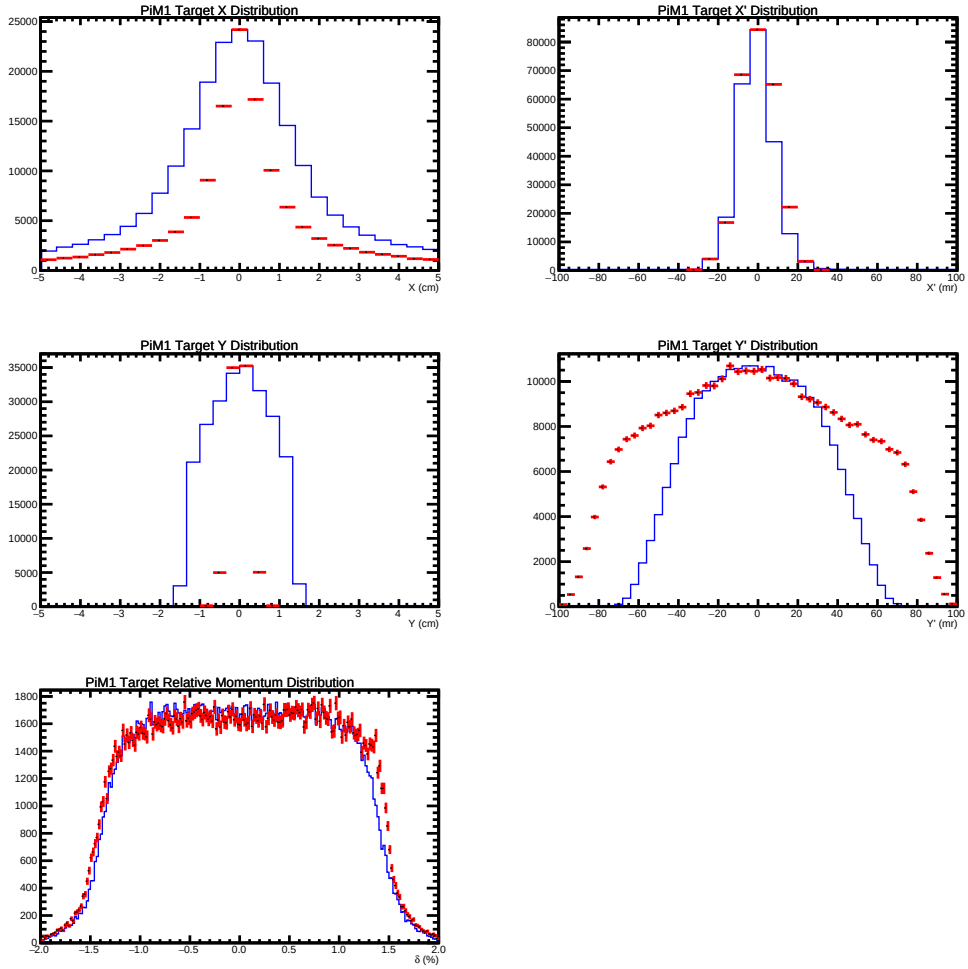

Figure 4.34: The distributions at the PiM1 target using a muon source for both TURTLE and G4beamline. TURTLE histograms are shown in red and G4beamline histograms are in blue. ***Upper Left:*** x distribution. ***Upper Right:*** x' distribution. ***Middle Left:*** y distribution. ***Middle Right:*** y' distribution. ***Lower Left:*** Relative Momentum, δ, distribution.

4.4 Time-of-Flight Simulations

The TOF of a particle is $t = L\sqrt{1 + \frac{m^2}{p^2}}$, as seen in Eq. 1.8, keeping in mind that t and L are the measured quantities and p is the quantity we wish to extract. This can also be represented as $t = L/(\beta c)$, where β is the average speed of the particle over the distance L. In the MUSE experimental setup there are 4 possible combinations of the 2 timing detectors used for the momentum measurement. Both the BH and BM detectors have two measurement positions. As we are measuring the beam momentum and not the scattered particle momentum we use beam line detectors and not scattered particle detectors. In our simulations and data analysis we take position L_0 to be our nominal position. L_0 is the position that has the minimum separation between our timing detectors.

A Geant4 description of the MUSE setup was written by Steffen Strauch of the University of South Carolina to simulate the full experiment as well as the special TOF calibration setup. The TOF simulation included the timing detectors used to start and stop the timing measurement, the GEM chambers, the VETO detector, and the MUSE scattering chamber. A detailed description of the experimental setup is necessary to simulate the momenta to the necessary precision. Every detector is fully described in Geant4 in order to take multiple scattering and energy loss processes into account as precisely as possible. To simulate the incoming beam, data was taken with the GEM chambers to measure the beam spot and angular distribution. This data was parameterized and fed into the simulation. Particle decay processes and Bremsstrahlung production were included for completeness to study and correct for background in the experimental data.

A detailed write up of the TOF simulation was provided by Steffen Strauch and is reproduced in Appendix D.

Examples of speed distributions from this simulation are given in Fig. 4.35. It is important that the analysis takes the variations shown into account as they correspond to momentum variations that are similar to the goal accuracy of $dp/p \lesssim 0.3\%$.

In summary time and distance in the experiment can be related to the speed of particles in the beam line simulation. The TOF simulation is capable of generating these quantities for the MUSE momenta and a detailed analysis that carefully includes peak positions and shapes will be performed in order to extract the momentum. It will be necessary to expand on the formalism required to compare the simulated quantities with the measured quantities. The details of this analysis will be shown in Sec. 5.4.

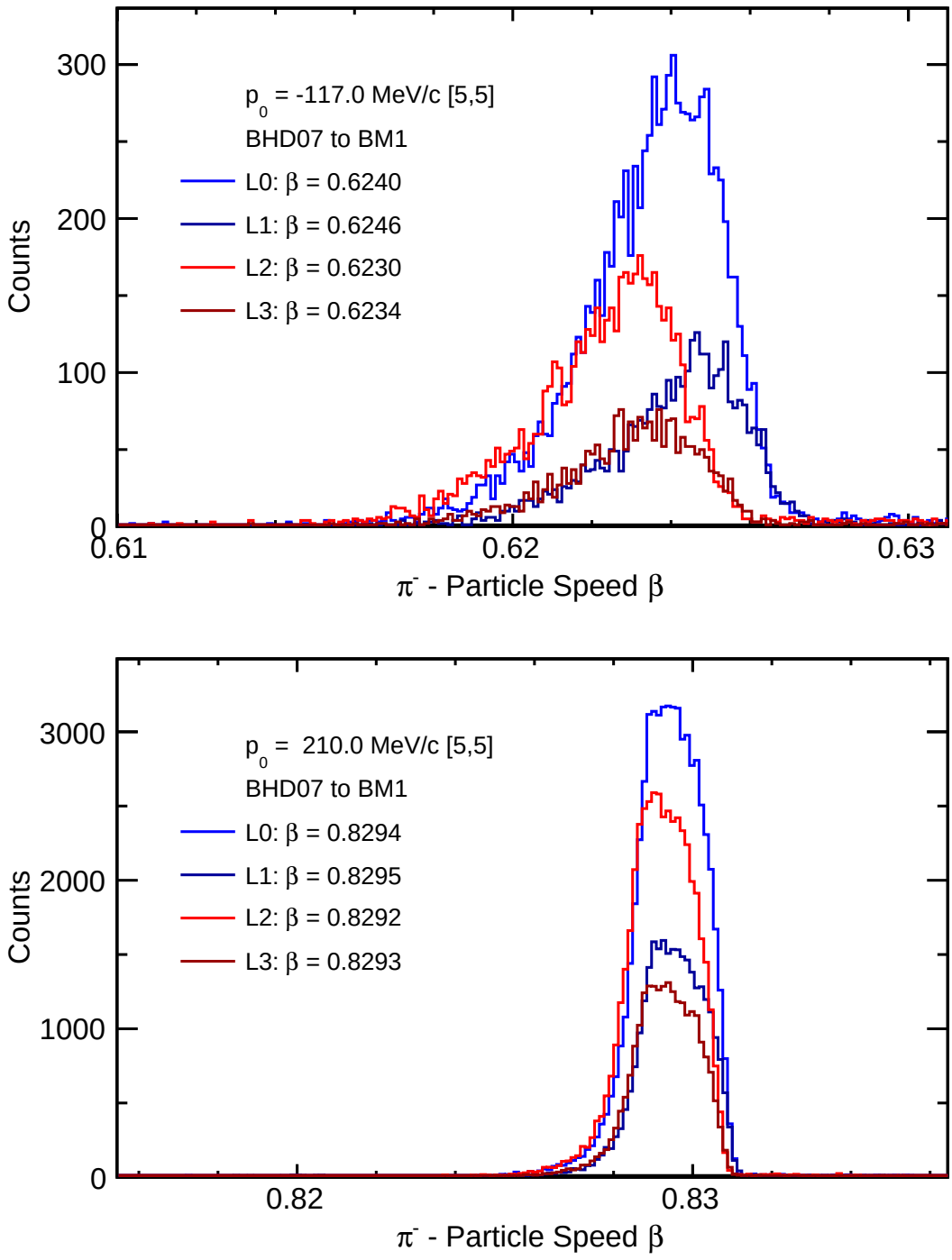

Figure 4.35: Examples of simulated speed distributions for pions at channel-momentum settings of 117 and 210 MeV/c.

Chapter 5
Analysis of Data

5.1 Detector Performance

5.1.1 GEMs

In general it has been established that all MUSE detectors are capable of achieving the resolution and efficiency necessary for the experiment in Sec. 3.1.1. However for the summer 2018 beam time there were two additional GEM planes installed at the IFP. These planes are not part of the MUSE production data setup and have generally poor performance. They were added to measure beam distributions at the IFP. In Fig. 5.1 we show several examples of ADC values for the x coordinate readout of the GEMs before noise subtraction routines were applied to the data. The top row of plots show ADC values for the "upstream" and "middle" GEMs at the PiM1 target region. The bottom row shows ADC values for the two GEMs at the IFP. It can be quickly noticed that the bottom left panel has a jump in the middle of the x axis. This jump in ADC value corresponds to two different APV cards. Recall that each coordinate on each GEM is read out by 2 APV cards. It appears that one of the APV cards is broken, given its higher noise baseline and restricted range of ADC values.

In the bottom left panel we see that one APV has a much higher baseline noise level than its adjacent APV. Both bottom panels also exhibit periodic noise structure in their ADC values at a larger level than the top panels. The top panels show reasonable ADC spectra for GEMs in the PiM1 target region. It can be seen at an ADC value of of $\approx 2500 - 3000$ for the top panels that there is an extended region of maxima near the center of the APV strip numbers. This corresponds to the beam passing through the center of the GEMs and depositing large amounts of energy near the center of the GEM.

In Fig. 5.2 we see the same GEMs after the noise subtraction routines have been implemented. The IFP GEMs have periodic noise in their spectra even after the noise subtraction. This leads to erroneous clusters and poorer performance when forming tracks between GEMs.

Hitmaps generated from the GEMs are shown in Fig. 5.3. The top panels again are from GEMs

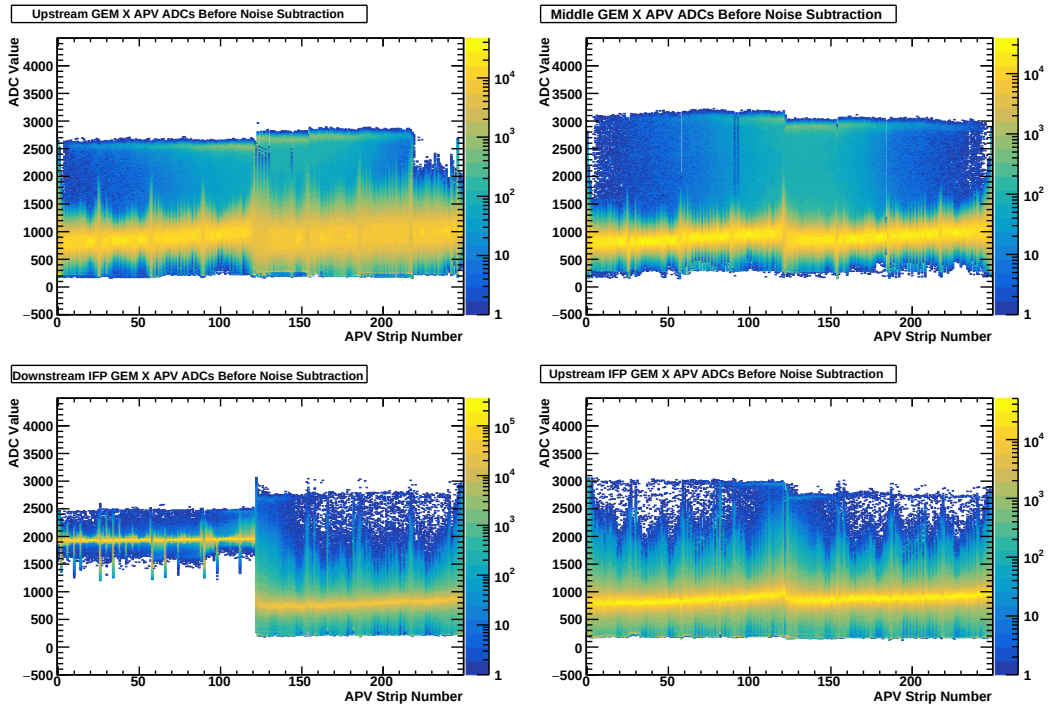

Figure 5.1: GEM X APV values before implementing noise subtraction routines.

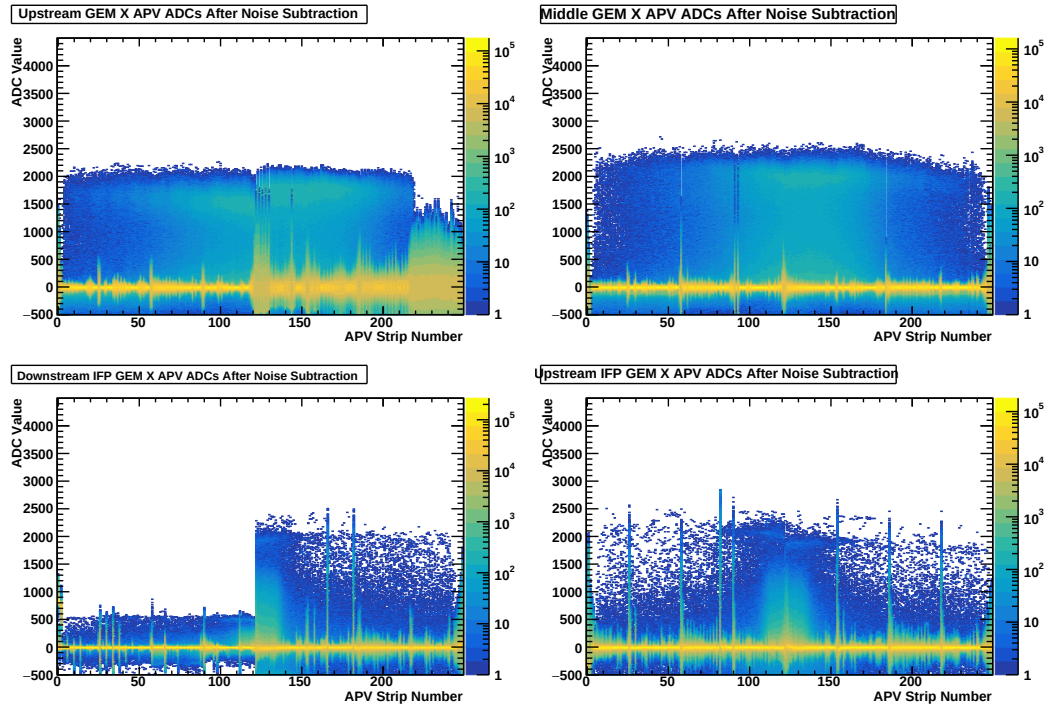

Figure 5.2: GEM X APV values after implementing noise subtraction routines.

in the PiM1 target region. It can be seen for the top left panel that there is an apparent dead region in the $+x$ section. This comes from nearly dead strips that could be seen in that x region in Figs. 5.1 and 5.2. For the bottom panels the IFP GEMs clearly have more noise and bumps in their distributions. This noise impacts to our ability to form high precision tracks. One dimensional distributions will be shown compared to simulation in Sec. 5.3 and 5.3.1 and the impact of the noise on our analysis will be clear. By careful inspection of the top two panels it can be seen that the GEM distribution is wider for the upstream GEM than for the middle GEM. The beam in PiM1 comes to a focus after the GEMs, at the scattering target. So it is consistent with expectations that the beam is wider in the upstream GEM and later comes to a focus.

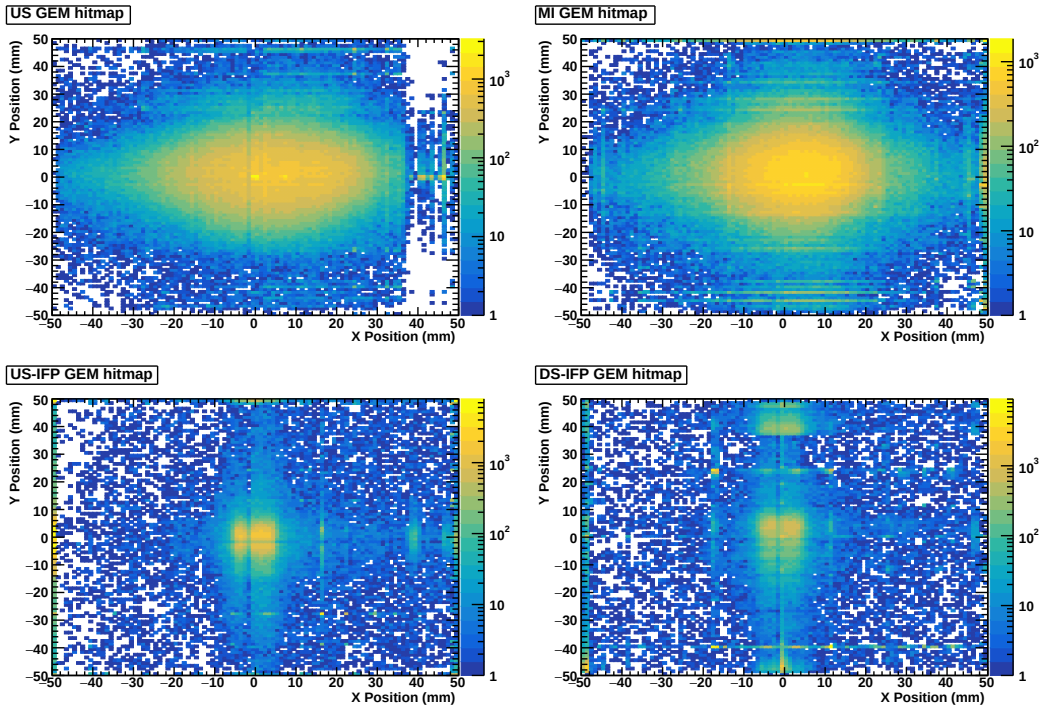

Figure 5.3: Example GEM hitmaps.

5.1.2 Beam Hodoscope

The BH detector, which provides our initial timing for the TOF measurements, also provides beam particle identification (PID) in our analysis. This detector is a low noise, high efficiency scintillator. Some multiplicity distributions can be seen in Fig. 5.4. The top row shows the multiplicity on a bar-by-bar basis for planes C and D, which were used in our data taking. We see that generally our multiplicities peak at 0, indicating low noise, with a secondary peak in the middle of the plane at a multiplicity of 2. This does not mean that the BH saw 2 hits per event; the TRB3 provides

timing for both leading and trailing edges. A multiplicity of 2 indicates that exactly one hit was seen in an event, and that hit had both leading and trailing edge. Even multiplicities correspond to hits with both leading and trailing edges. Odd multiplicities occur when one edge is cut off in our timing window. The bottom row of panels in the figure show the integrated multiplicity across a plane. We see the odd multiplicities are suppressed, and even multiplicities peak at 2 and decrease for each higher multiple of 2. In these integrated plots we see that the number of 0's is reduced in comparison to the number of 2's. When compared with the top panels in the figure this leads to the conclusion that any given bar most often did not see a hit in an event, but the entire plane saw 1 hit per event.

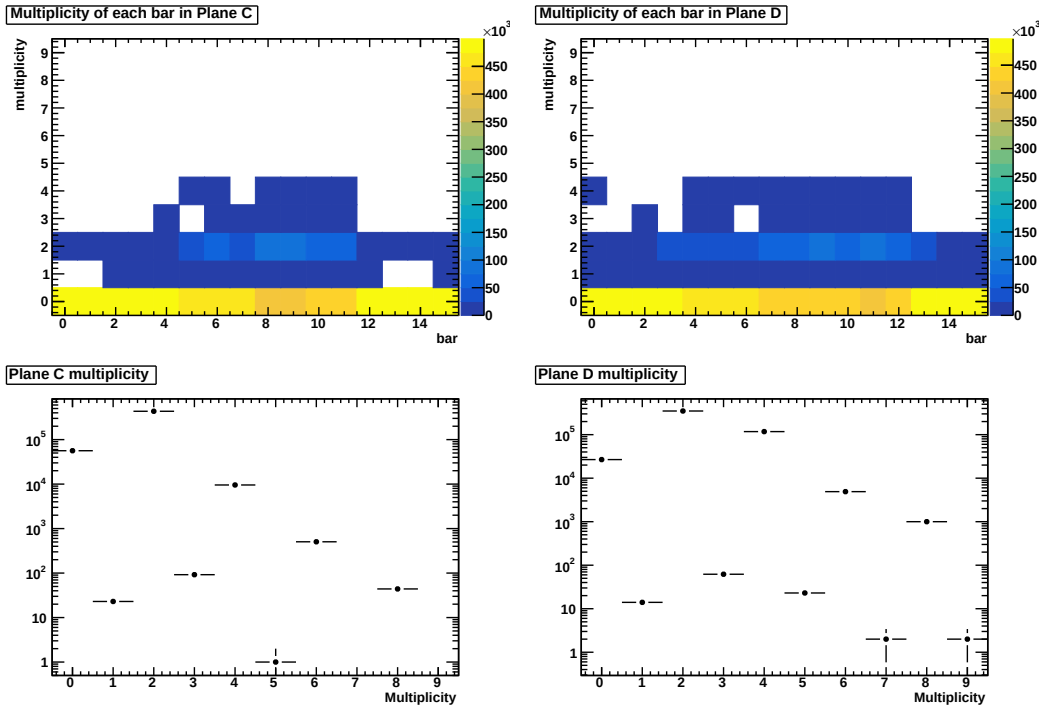

Figure 5.4: Example BH multiplicity.

As a cross check of the GEM distributions we can present a "paddle map", similar to a wire map from a drift chamber, from the BH. This paddle map provides a cross section of the beam at the BH detector and shows the number of hits across the entire run on a bar-by-bar basis. The paddle map is shown in Fig. 5.5. Variations in the number of events in each bar can give a rough estimation of how well gained matched the bars are. The two planes we show here are oriented perpendicularly to each other, allowing us to see the width of the beam in x and y. Plane D measures in x and plane C in y. The wide plane D distribution matches with the GEM hitmaps in Fig. 5.3 that show a wider x distribution than y. Recall that the BH sits upstream from the most upstream GEM plane.

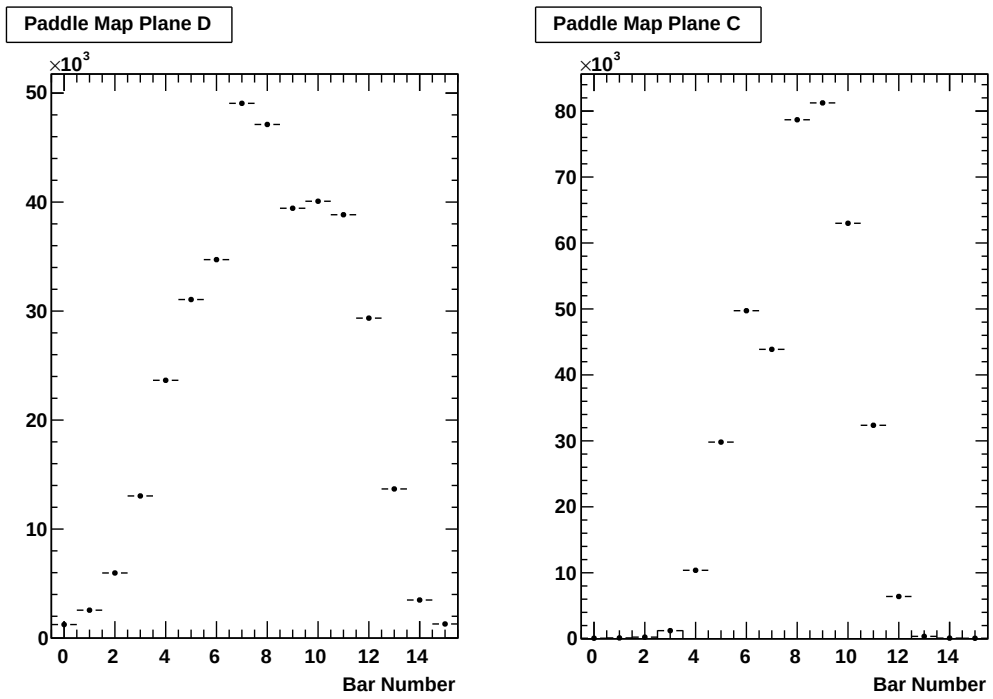

Figure 5.5: Example BH paddle map.

5.2 Beam distribution measurements

Next we move on to a comparison of our experimental results with g4beamline simulations and TURTLE simulations of the entire PiM1 channel in Sections 5.3 and 5.3.1, respectively. Note that all results in this section are presented in transport coordinates: in the PiM1 area +z is along the beamline, +x is to beam right, and +y is vertically downward.

5.2.1 Beam distributions at target with quadrupoles ON or OFF

Here we present a comparison of the centroids of our particle distributions at the target position with the last 6 quadrupoles ON or OFF. The results are shown in Table 5.1 and 5.2. All quoted uncertainties are statistical only. We know that a systematic uncertainty exists from a warping of the distributions caused by inefficiencies in the GEMs but we do not have an estimate for this effect.

Comparing Table 5.1 with 5.2, we see that the centroid position values at the PiM1 target are shifted significantly when the IFP GEMs are in place. This is caused by momentum loss of the beam as it interacts with the GEM material. Furthermore, it is interesting to see that there is a 1 cm deviation in the centroid positions from one particle type to the next, when the IFP GEMs are in place and the quads are turned off.

IFP GEMs In	Quads On Centroid Position (mm)	Quads off Centroid Position (mm)
e	3.7 ± 0.11	11.2 ± 0.10
μ	1.9 ± 0.27	0.9 ± 0.24
π	0.4 ± 0.09	-8.8 ± 0.16

Table 5.1: Particle ensemble centroid positions with quadrupoles on and off and the IFP GEM planes installed, for a central momentum of +161 MeV/c. The collimator is set to a width of 1 cm.

IFP GEMs Out	Quads On Centroid Position (mm)	Quads off Centroid Position (mm)
e	1.9 ± 0.09	8.7 ± 0.14
μ	0.6 ± 0.30	1.2 ± 0.45
π	0.4 ± 0.09	-0.2 ± 0.12

Table 5.2: Particle ensemble centroid positions with quadrupoles on and off and the IFP GEM planes removed, for a central momentum of +161 MeV/c

5.2.2 Momentum loss due to IFP-GEMs: Geant4 simulation versus data

Geant4 simulations of only two GEM planes, an extended region of air with plastic vacuum windows at the IFP and beam were performed to study how energy losses in the windows, air and GEMs at the IFP affect the electrons, muons and pions in the beam. These simulations were run both with and without GEM planes at the IFP. The simulations used a pencil beam with no dispersion to approximate the PiM1 beam at the IFP. For completeness, the simulations were also run with a momentum bite of ± 0.5% around the central momentum for a more realistic description of our beamline set-up, but this was found to have an effect on the order of less than 10^{-3} on the mean momentum loss. Appendix A shows the initial particle momentum going into the IFP region in red and the particle momentum as it leaves the IFP as a distribution in black. To present the results in a more human-readable format we compile the results into Table 5.3 showing the initial momentum and the mean final momentum after passing through the IFP material and GEM planes. Similarly, we list the momentum loss of particles traversing the IFP region without the GEMs in Table 5.4.

Since the central bend angle of the ASM12 dipole magnet is 75°, a 1% change in momentum corresponds to a shift in the bend angle through the dipole of 0.75°. This shift, when combined with the 7.5 m lever arm between the ASM12 dipole and the target, yields a position change of 10 cm. Our simple estimate here is consistent with the simulations presented in Section 4.2.2, that 1-cm

Δp Loss due to IFP GEMs	117 MeV/c	161 MeV/c	210 MeV/c
e	116.51(0.4%)	160.47(0.3%)	209.44(0.3%)
μ	116.22(0.6%)	160.43(0.4%)	209.51(0.2%)
π	115.85(1%)	160.26(0.5%)	209.42(0.3%)

Table 5.3: A Geant4 simulation to study momentum loss for all 3 particle species and all 3 MUSE momenta due to GEMs at the IFP. The values in parenthesis indicate the percent of the central momentum that is lost.

Δp Loss due to IFP Material	117 MeV/c	161 MeV/c	210 MeV/c
e	116.741(0.22%)	160.728(0.16%)	209.717(0.13%)
μ	116.599(0.34%)	160.705(0.18%)	209.746(0.12%)
π	116.408(0.51%)	160.617(0.24%)	209.701(0.14%)

Table 5.4: A Geant4 simulation to study momentum loss for all 3 particle species and all 3 MUSE momenta due to air and magnet windows at the IFP. The values in parenthesis indicate the percent of the central momentum that is lost.

offsets in position distributions at the target between different particle types correspond to roughly 0.1% momentum differences. We note that from our simulation, in particular the 117 MeV/c column of Table 5.3, we expect a maximum relative shift of 4 cm between particles at any momentum, and for 161 MeV/c in particular we expect a shift of no larger than 1 cm between particle types. We also note that the simulation indicates that the 2 GEM planes roughly double the momentum loss at the IFP compared to the loss induced by air and the windows.

We now compare Geant4 results with experimental results. We focus on our experimental data taken when the quadrupoles were turned off. In addition to comparing the energy loss in simulation with data, we want to determine the variation in the bending of the different particle types through the ASM12 dipole after they interact with material at the IFP. For our results, we compare relative differences between particle types at a single momentum setting. As an arbitrary choice, we compare all differences to the values, position and momentum, given by the μ's. Usually in our kinematics the e's lose less momentum than the μ's so that they are at $+x$ or beam right, of the μ's, while π's lose more momentum and appear at $-x$ or beam left of the μ's. We see that this is the case for 161 MeV/c and the simulation and experiment agree. For 210 MeV/c the simulation predicts that e's lose more momentum than the μ's and our data reflects this.

Beam Momentum	GEM Position	Particle Type	δx at target			Momentum Difference Relative to μ (%)	
			Mea. (mm)	Relative to μ (mm)			
			Abs.	Rel.	Sim.	Mea.	Sim.
161	In	e	11.2 ± 0.10	10.3 ± 0.26	10	0.103%	0.1%
		μ	0.9 ± 0.24	-	-	-	-
		π	-8.8 ± 0.16	-9.7 ± 0.29	-10	-0.097%	-0.1%
	Out	e	8.7 ± 0.14	7.5 ± 0.47	2	0.075%	0.02%
		μ	1.2 ± 0.45	-	-	-	-
		π	-0.2 ± 0.12	-1.4 ± 0.46	-6	-0.01%	-0.06%
210	In	e	-14.7 ± 0.13	-9.9 ± 0.37	-10	-0.099%	-0.1%
		μ	-4.8 ± 0.35	-	-	-	-
		π	-19.1 ± 0.10	-14.3 ± 0.36	-10	-0.143%	-0.1%

Table 5.5: Comparison between experimental data and Geant4 simulation for 161 MeV/c and 210 MeV/c. We compare experiment and simulation if the IFP GEMs are in place or removed, and we separate out each particle type. We show the measured absolute position of the particle distributions at the PiM1 target and the relative difference between each particle type and the μ distribution. We compare our measured values to simulation for both the relative position and momentum, using the assumption that a 1% difference in momentum corresponds to a 10 cm shift in position at the target. For 161 MeV/c the e and π distributions appear on opposite sides of the μ distribution, however this is not the case for 210 MeV/c, which is in agreement with simulation.

As can be seen in Table 5.5, our simulation recreates the expected differences in particle distribution to within 0.003% when GEMs are placed at the IFP position for 161 MeV/c. We can also see agreement between simulation and experiment on the order of 0.05% when GEMs are not placed at the IFP. As an additional check we performed both a simulation and measurement of momentum loss for a central momentum of 210 MeV/c with IFP GEMs in place. We again see agreement between simulation and experiment on the order of 0.05%. Again the uncertainties are purely statistical in nature. We have do not have a firm number for the experimental systematic uncertainties. To conclude, the measured data are consistent with simulated energy loss and channel properties.

5.3 Comparison between G4beamline and experiment

The previous section demonstrated that Geant4 simulations of just the material at the IFP give results that are consistent with data. Now, we transition to a simulation of the entire beamline using the G4beamline simulation software. We updated the G4beamline default simulation presented in Section 4.3 to match it with the actual beamline set-up, including matching the material type to account for energy loss and multiple scattering. We also added shields around the GEM detectors and beam hodoscope planes to be consistent with the cuts applied in the analysis of the summer data, in which only those tracks were considered that were detected by the GEM and beam hodoscope detectors. Figure 5.6 shows a visualization of the updated beamline. The details are given below:

1. We added a collimator made of copper blocks at the IFP. We set the slit opening to ± 0.5 cm along the x direction. Each copper block is 20 cm wide along x, 40 cm high along y and 10 cm long along the beamline.

2. We added two GEM planes after the collimator. The first plane is 8 cm away from the downstream end of the collimator. The second GEM plane is 8 cm away from the first GEM plane. The active material is made of Mylar, Aluminum, Kapton, Copper layers and GEM gas (70% Argon, 30% CO_2). We placed a shield around each GEM plane to kill particles that did not hit the active material of the GEM detector. This is consistent with the cuts applied to the data.

3. We replaced the virtual detector at the beam hodoscope location with two beam hodoscope planes, each made of vinyltoluene plastic. Each plane is 2 mm thick and 10 cm diameter. The spacing between the two planes is 2 cm. We placed a shield around each GEM plane to kill particles that did not hit the active material of the GEM detector, consistent with data analysis.

4. We added four GEM planes near the PiM1 target location, with 6.5 cm space between each GEM plane. The first GEM plane is placed 2 cm downstream of the second beam hodoscope plane. The fourth GEM plane is placed 35 cm upstream of the target location.

5. We updated the fields of the quadrupoles to summer 2018 settings. We also flipped the polarities of QSL17 and QSL18, consistent with the experimental settings. The power supplies for these magnets were inadvertently hooked up backwards.

6. We lowered the dipole current of the second dipole by 1% because the particles lost energy when they interacted with the GEM material at the IFP. We performed this tuning by hand

in order to center the beam on the GEMs and so we matched that tuning in the simulation.

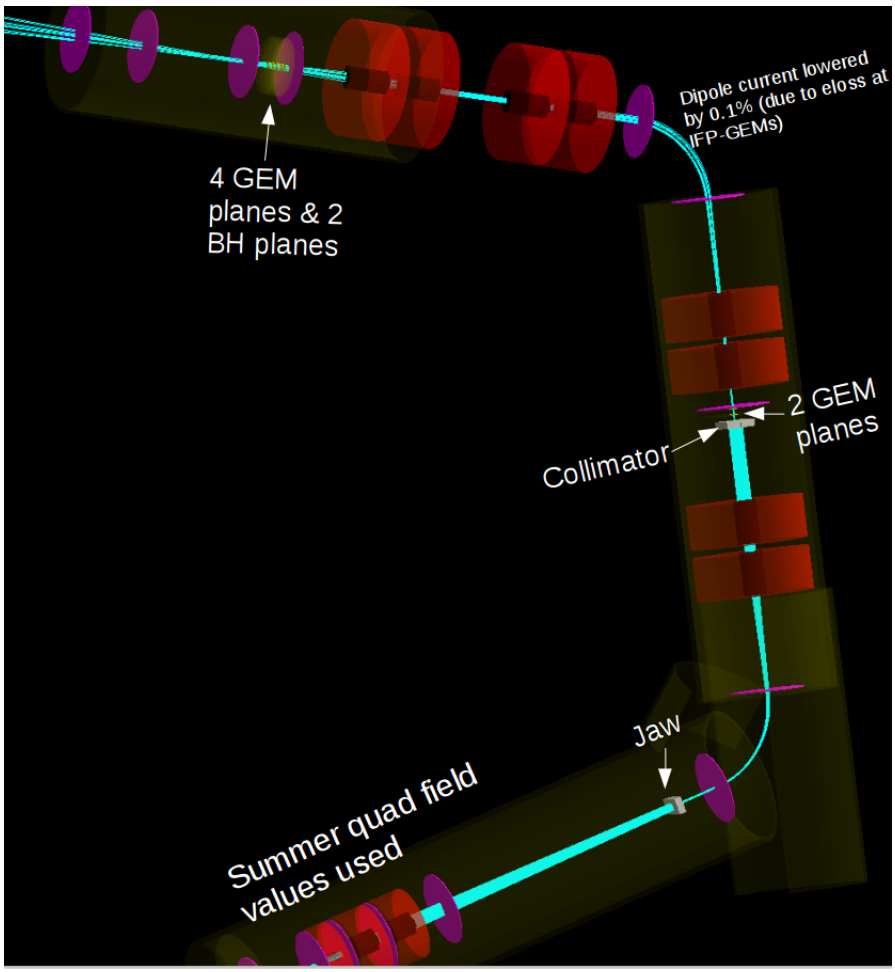

Figure 5.6: A visualization in G4beamline simulation of 5000 μ^+ sample events from a point source. Only μ^+ parent particles are propagated. The picture shows the jaw, collimator, GEM planes and beam hodoscope planes that were added to the simulation to match the experimental set-up.

Here we compare G4beamline results and experimental results for the beam distributions at the IFP and the PiM1 target for a 161 MeV beam. The input distributions are the realistic distributions that were also used for TURTLE. By applying a PID cut on our BH detectors we are able to perform a particle type separation in the analysis so we can compare each particle species with a corresponding simulation. Particles are produced at the M production target frequency locked with pulses of protons from the primary beam line. Taking the time difference in our BH detector and the RF pulse from the proton accelerator and modulating that difference by the RF frequency of the accelerator we see each particle species is well separated in this "RF time".

Figures 5.7 to 5.9 shows the spatial and angle distributions at the IFP. Only those events are

shown which are detected by the two GEM detectors at the IFP, the two beam hodoscope planes and the four GEMs at PiM1 target, in G4beamline as well as the data. In each distribution, we scaled the simulation by a constant factor given by (peak height in data/peak height in simulation). Both simulation and measured distributions show that the beam spot is very narrow at the IFP, due to the collimator. There is a reasonable agreement between the simulation and experimental measurements. We see a dip in the y distribution near $y = 0$ in the experimental measurement, but not in the simulation. This is because there are dead GEM strips at that location which have not been taken into account in the simulation. We also stress that the GEMs placed at the IFP have not been surveyed, and with only two GEM planes it is not possible to perform a software alignment. This lack of survey likely accounts for the offsets between simulated and measured x' and y' distributions. We note that agreement between simulation and data at the IFP is generally good, but the measured y distributions are wider than those shown in simulation.

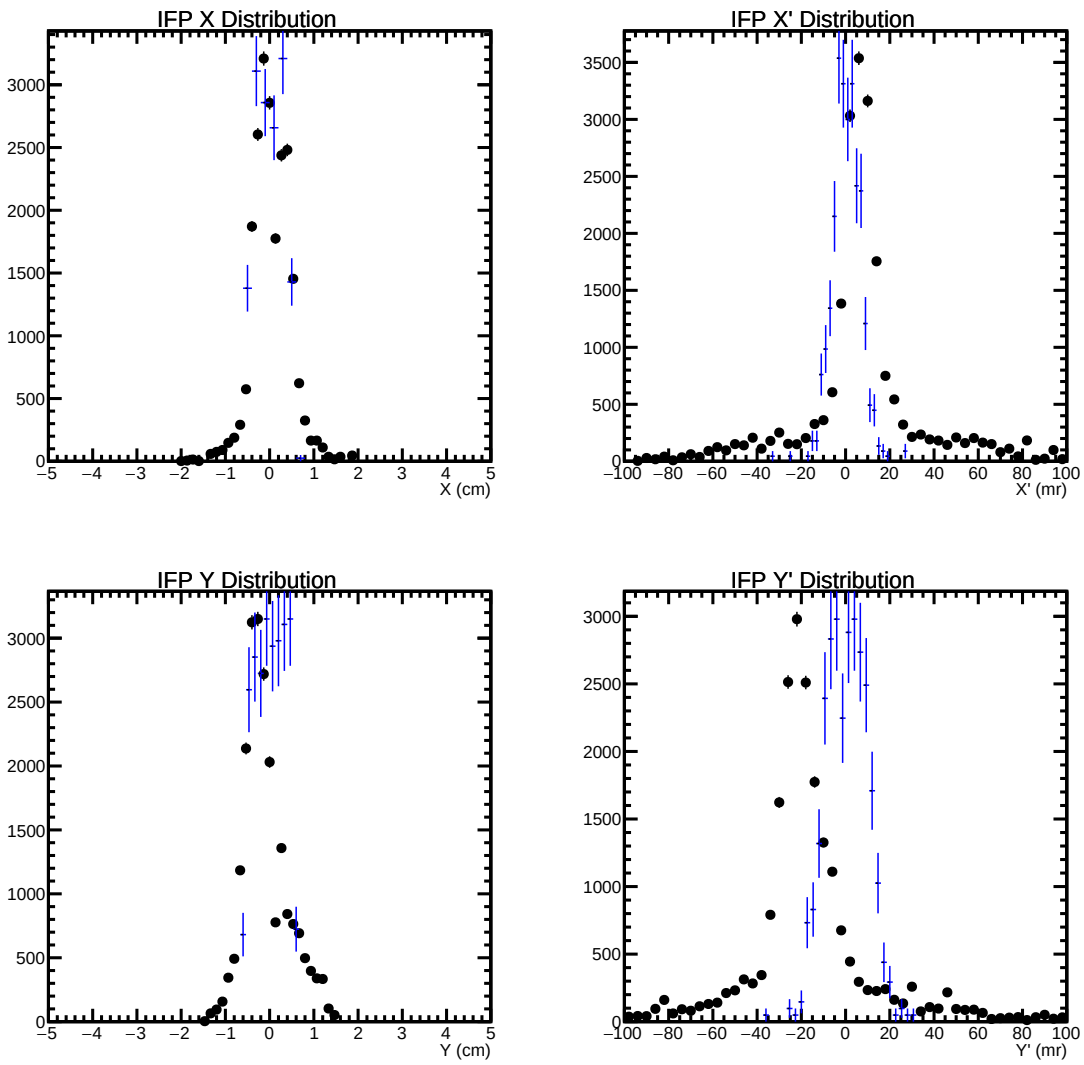

Figure 5.7: A comparison between G4beamline and experimental data at the IFP for electrons. The G4beamline simulation is in blue and the data is in black. ***Upper Left:*** x distribution. ***Upper Right:*** x' distribution. ***Lower Left:*** y distribution. ***Lower Right:*** y' distribution.

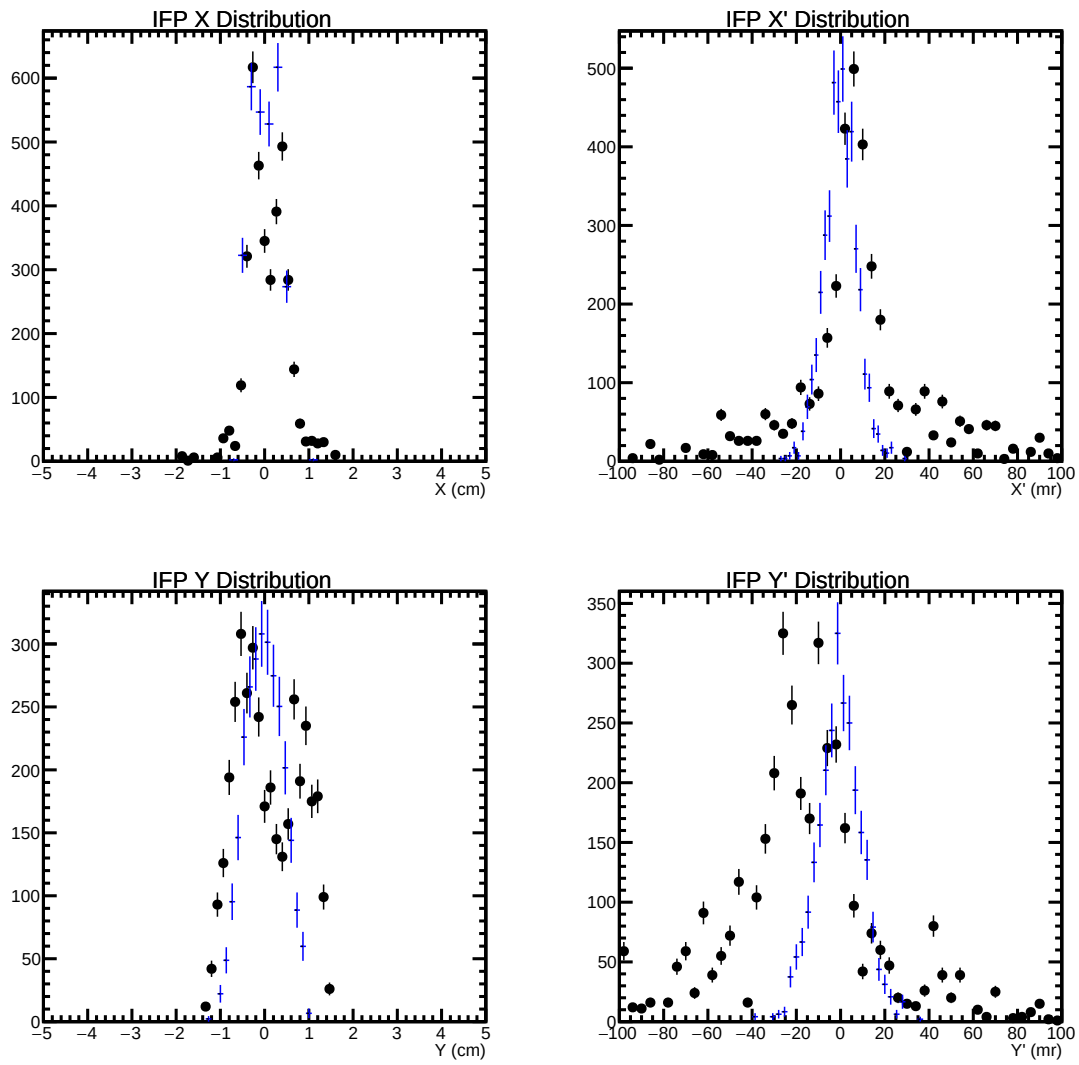

Figure 5.8: A comparison between G4beamline and experimental data at the IFP for muons. The G4beamline simulation is in blue and the data is in black. ***Upper Left:*** x distribution. ***Upper Right:*** x' distribution. ***Lower Left:*** y distribution. ***Lower Right:*** y' distribution.

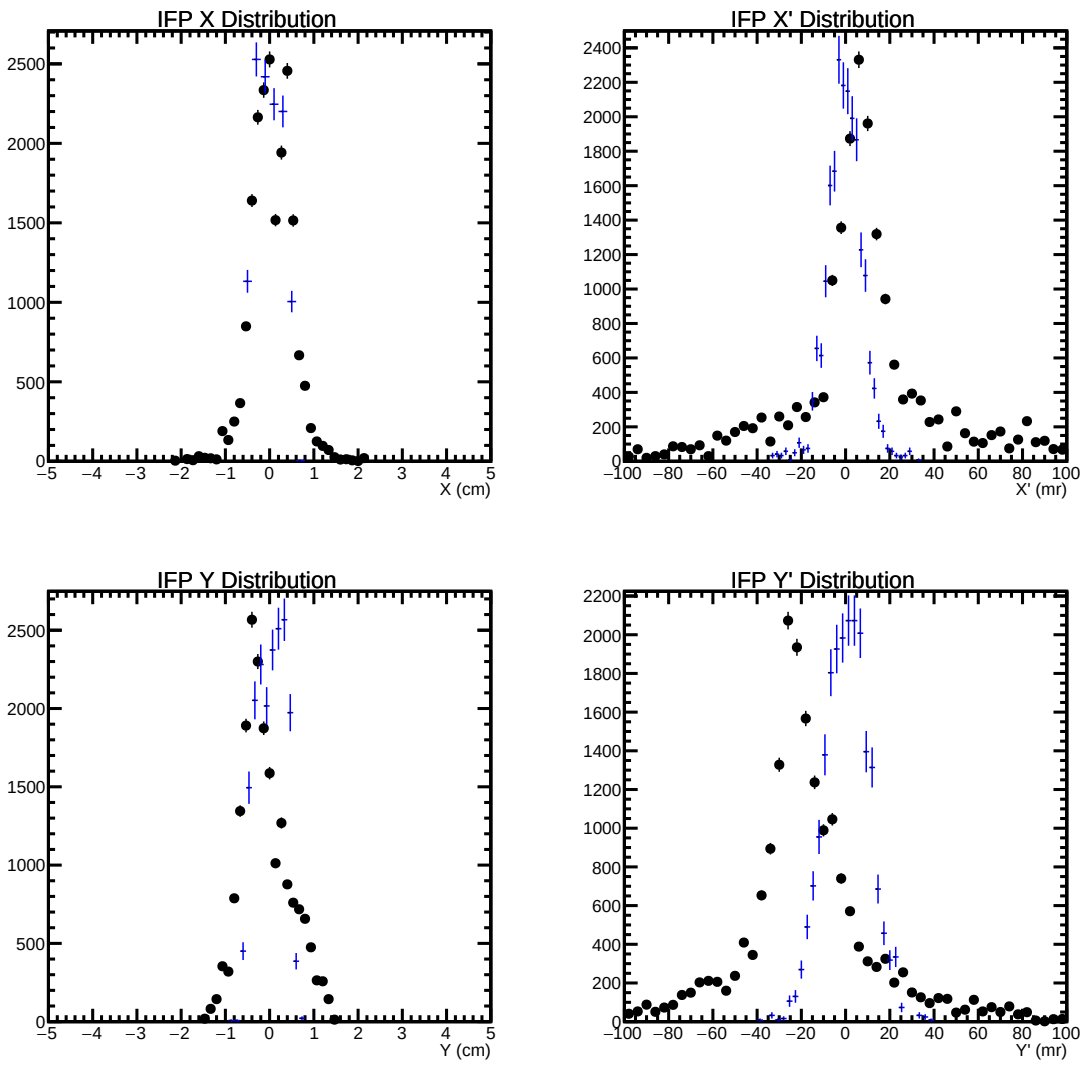

Figure 5.9: A comparison between G4beamline and experimental data at the IFP for pions. The G4beamline simulation is in blue and the data is in black. ***Upper Left:*** x distribution. ***Upper Right:*** x' distribution. ***Lower Left:*** y distribution. ***Lower Right:*** y' distribution.

Figures 5.10 to 5.12 show the spatial and angular distributions of the beam at the PiM1 target, after removing events that were not detected by all of the six GEM (including the two at the IFP) planes and the two beam hodoscope planes (used for PID). We see good agreement between the simulation and data for all data sets. We note that the measured muon distribution does not exhibit long tails as predicted in the simulations. We believe that the level of agreement can be improved further by improving the dipole field maps in the simulations.

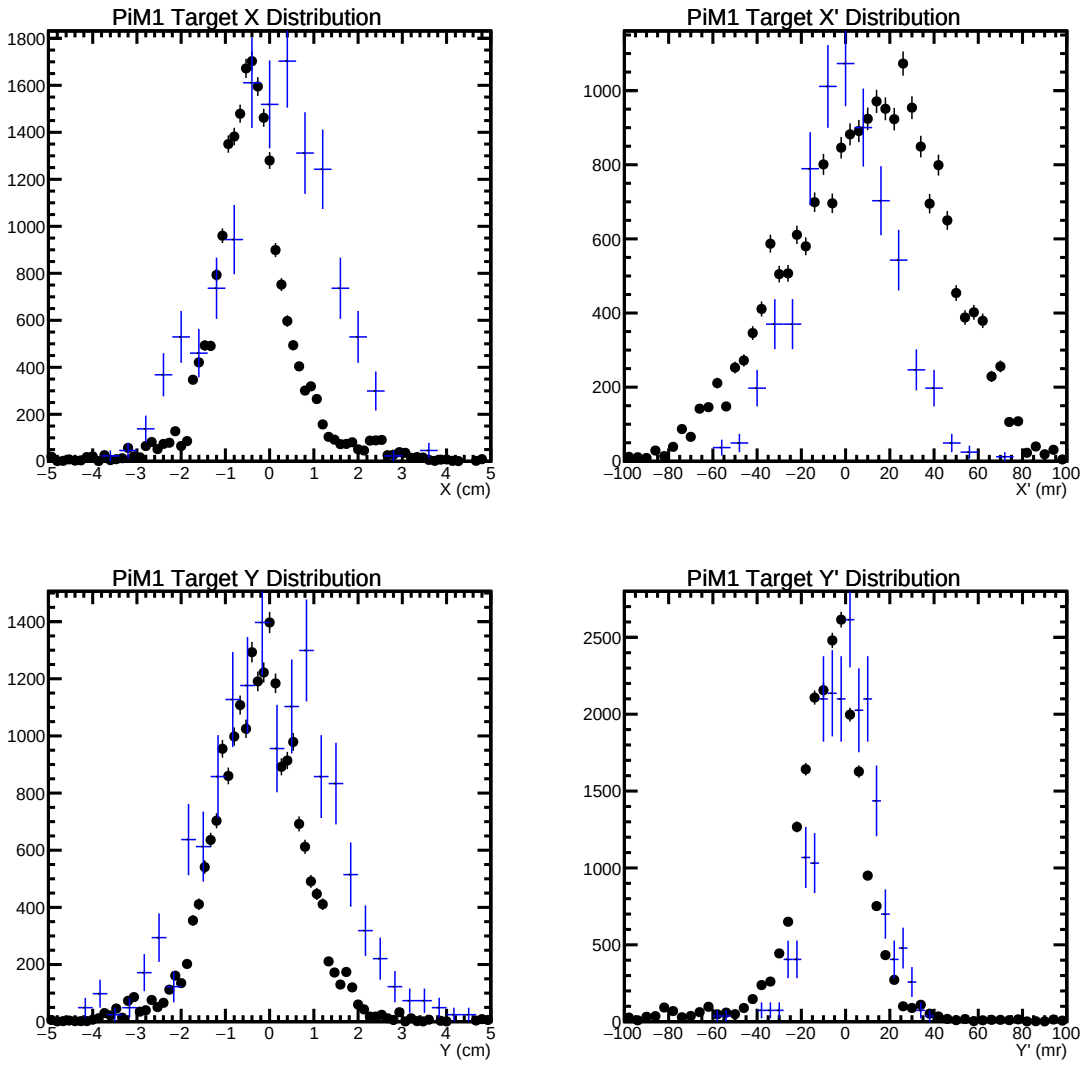

Figure 5.10: A comparison between G4beamline and experimental data at the PiM1 target for electrons. The G4beamline simulation is in blue and the data is in black. ***Upper Left:*** x distribution. ***Upper Right:*** x' distribution. ***Lower Left:*** y distribution. ***Lower Right:*** y' distribution.

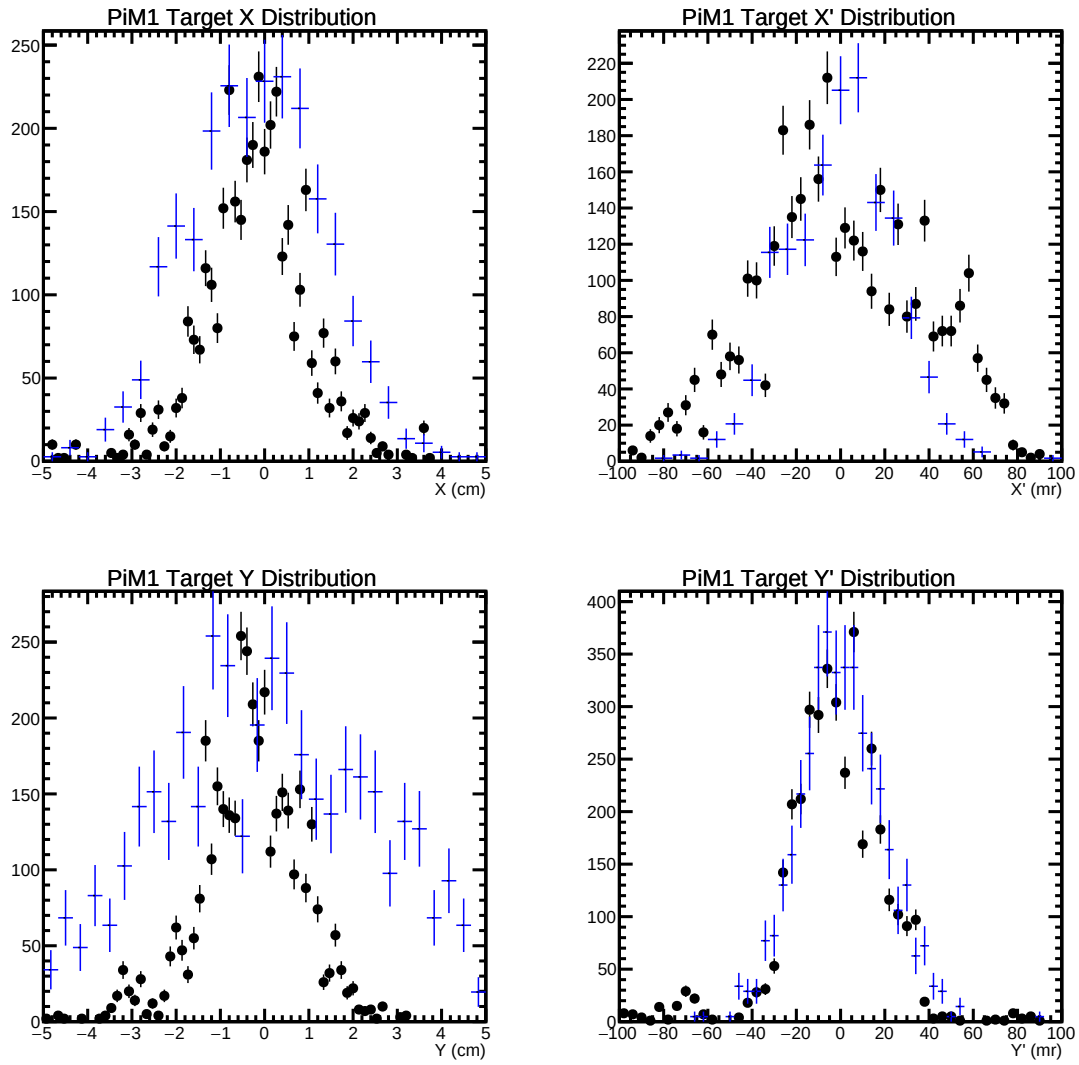

Figure 5.11: A comparison between G4beamline and experimental data at the PiM1 target for muons. The G4beamline simulation is in blue and the data is in black. ***Upper Left:*** x distribution. ***Upper Right:*** x' distribution. ***Lower Left:*** y distribution. ***Lower Right:*** y' distribution.

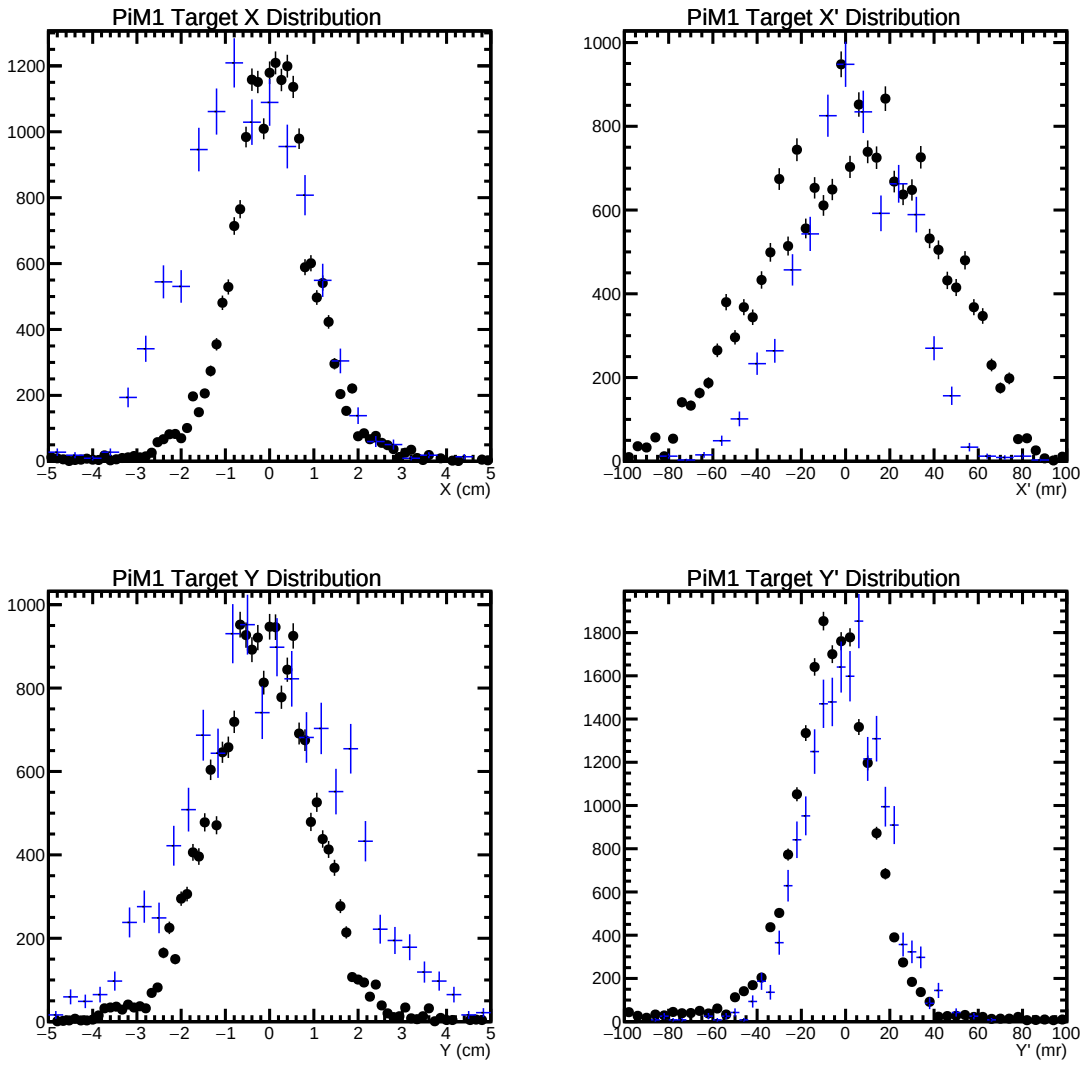

Figure 5.12: A comparison between G4beamline and experimental data at the PiM1 target for pions. The G4beamline simulation is in blue and the data is in black. ***Upper Left:*** x distribution. ***Upper Right:*** x' distribution. ***Lower Left:*** y distribution. ***Lower Right:*** y' distribution.

5.3.1 Comparison between TURTLE and experiment

The TURTLE simulation inputs were modified in the same way as the G4beamline inputs to simulate the 2018 data. We adjusted the default simulation to use quadrupole fields as set, added in FS11 jaws, and the narrow collimator at the IFP. We included energy loss routines for TURTLE and placed 1 mm of carbon at the IFP to approximate the energy loss experienced by particles passing through 2 GEM planes. It is difficult to accurately model more complicated materials in TURTLE so an approximation with carbon was made. As TURTLE treats all particles the same when traversing

the beam line with the exception of the source size, we use the same simulation of electrons and pions, but a simulation with a large source size for muons.

The resulting simulation at the IFP is shown in Figs. 5.13 to 5.15. The x distributions, which are constrained by the slot, and the x' distributions agree reasonably well in shape. The y distribution is wider in the simulation, in contrast with the G4beamline simulation. This is likely due to differences in energy loss mechanisms for the beam passing through the FS-11 jaws. The y' distribution is about the right size, but the data are not centered. We again note that the GEM chambers at the IFP were placed by hand, not surveyed, and their alignment relative to the beam is not certain. Also, since there were only 2 GEM chambers at the IFP, and there were some inefficiencies seen, the experimental distributions are somewhat modified from reality.

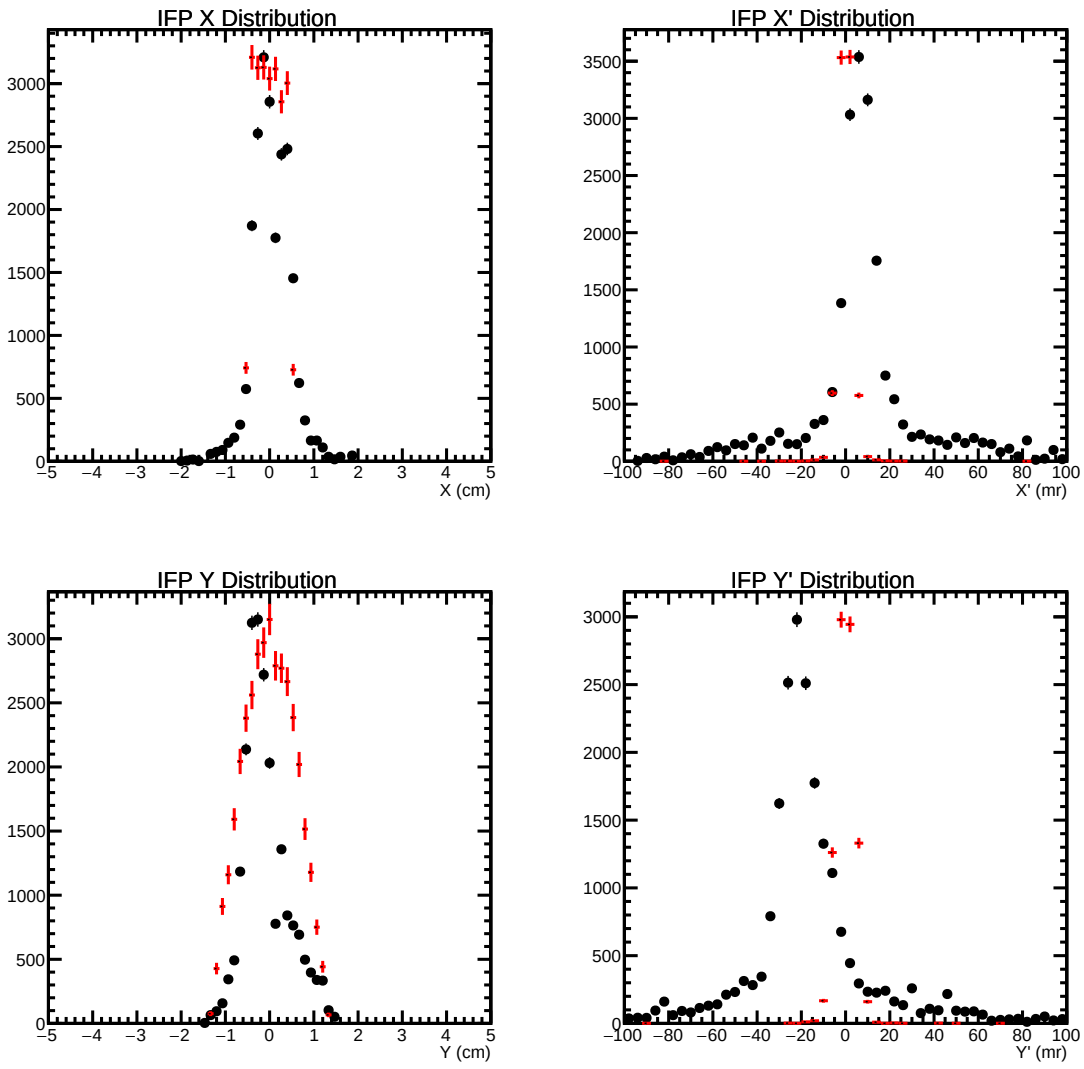

Figure 5.13: A comparison between TURTLE and experimental data at the IFP for electrons. The TURTLE simulation is in red and the data is in black. ***Upper Left***: x distribution. ***Upper Right***: x' distribution. ***Lower Left***: y distribution. ***Lower Right***: y' distribution.

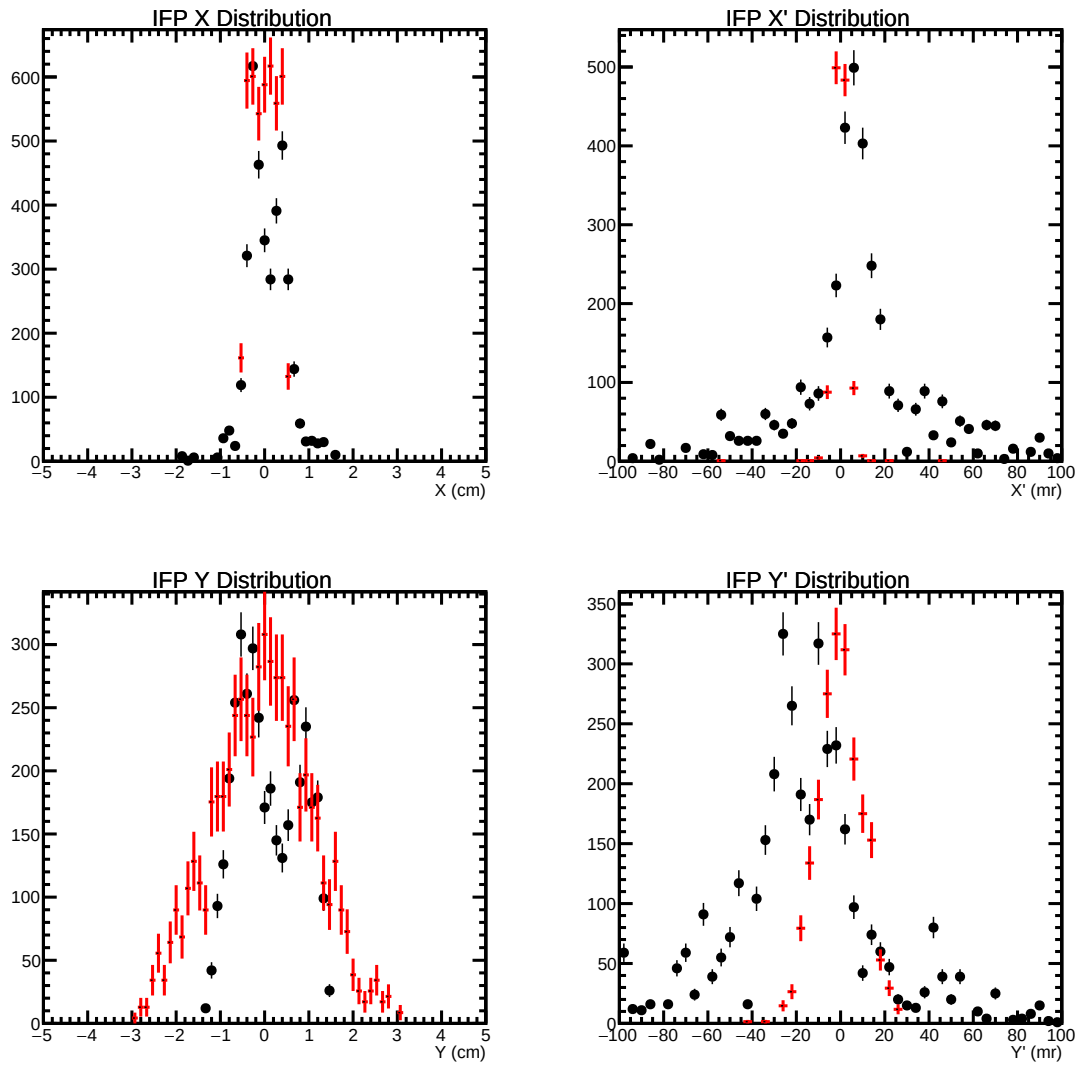

Figure 5.14: A comparison between TURTLE and experimental data at the IFP for muons. The TURTLE simulation is in red and the data is in black. ***Upper Left***: x distribution. ***Upper Right***: x' distribution. ***Lower Left***: y distribution. ***Lower Right***: y' distribution.

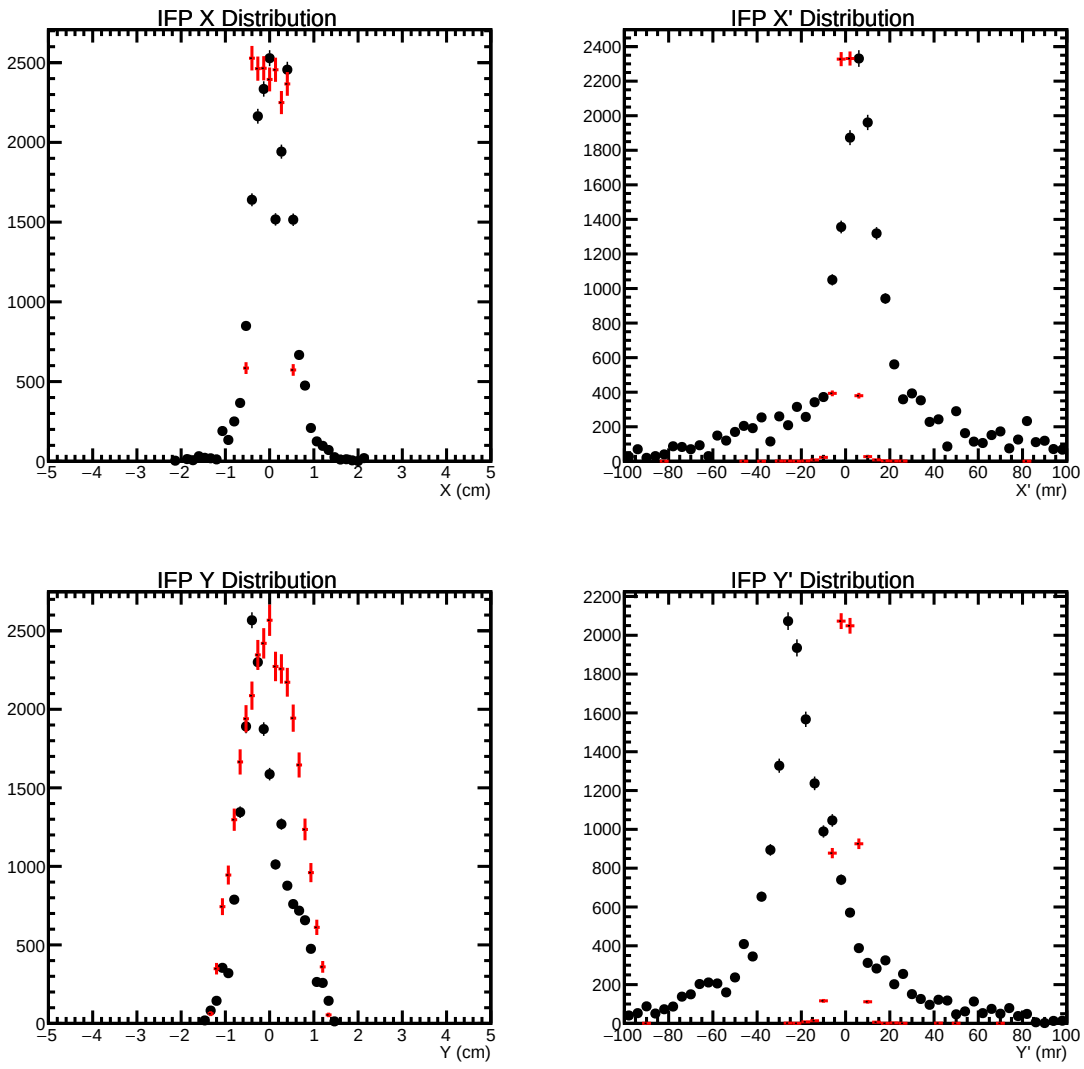

Figure 5.15: A comparison between TURTLE and experimental data at the IFP for pions. The TURTLE simulation is in red and the data is in black. ***Upper Left***: x distribution. ***Upper Right***: x' distribution. ***Lower Left***: y distribution. ***Lower Right***: y' distribution.

The resulting simulation at the target is shown in Figs. 5.16 to 5.18. The x distributions are wider in TURTLE than in the data, even though the distributions at the IFP match reasonably well. From the dispersion discussion and the experimental setup, this could arise because the momentum distributions at the IFP are broader than the simulation predicts, or because the simulation does not accurately reproduce the momentum and multiple scattering spread of the beam going through the GEMs. We see that TURTLE also generally predicts smaller ranges in x' than the data suggests. This is likely a phase space issue in focusing the last quads after the bending dipole. As was

mentioned earlier, the last quad pairs were set to the wrong current polarity and it is likely our conversion from current to magnetic field is not completely correct, as the magnets were not properly cycled. We cannot reconstruct what the precise magnetic field might have been from the data at our disposal. We note that for the muon data and simulation that the TURTLE prediction of the beam in y is so large that it runs off the end of plot. The distribution is $\pm$ 10 cm.

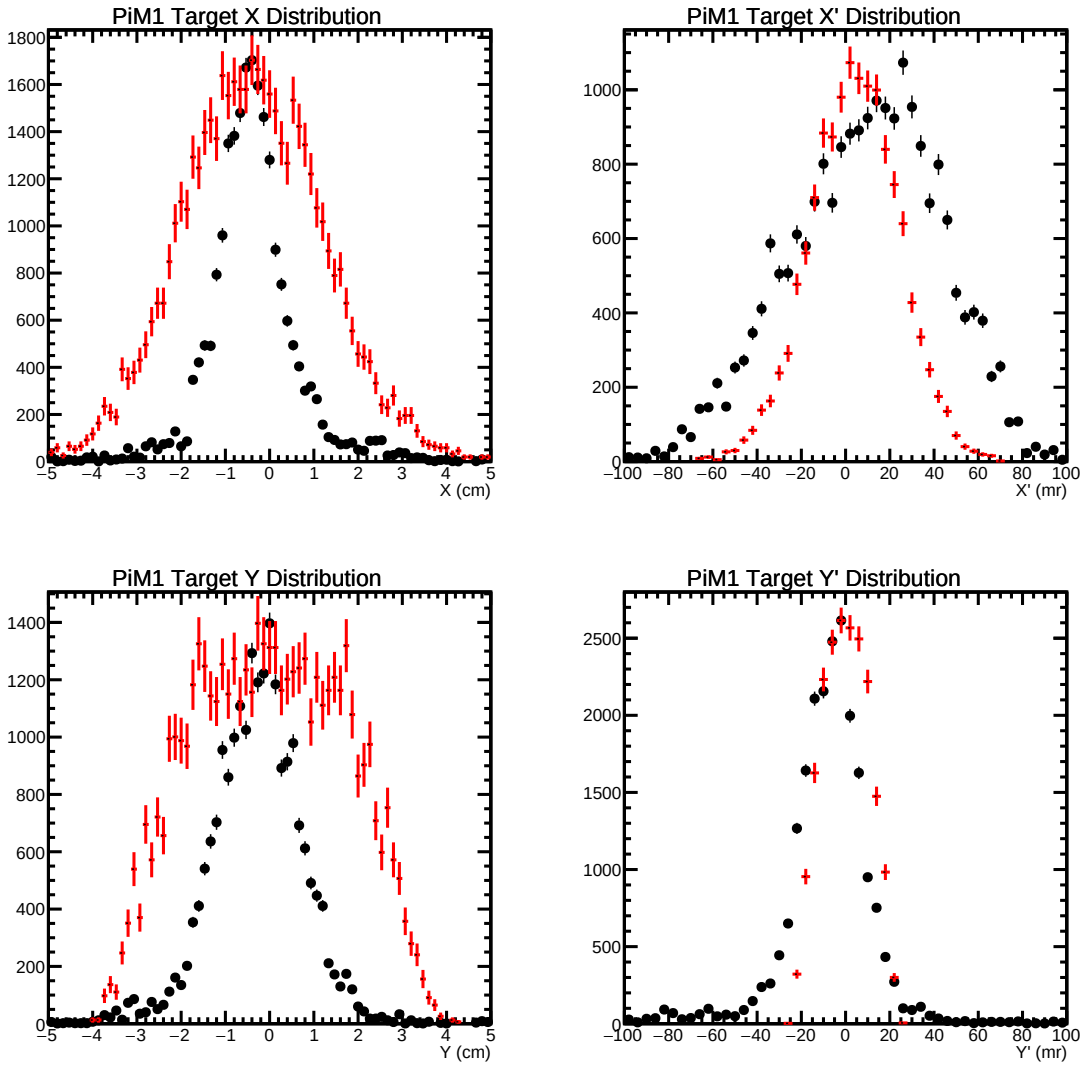

Figure 5.16: A comparison between TURTLE and experimental data at the PiM1 target for electrons. The TURTLE simulation is in red and the data is in black. ***Upper Left***: x distribution. ***Upper Right***: x' distribution. ***Lower Left***: y distribution. ***Lower Right***: y' distribution.

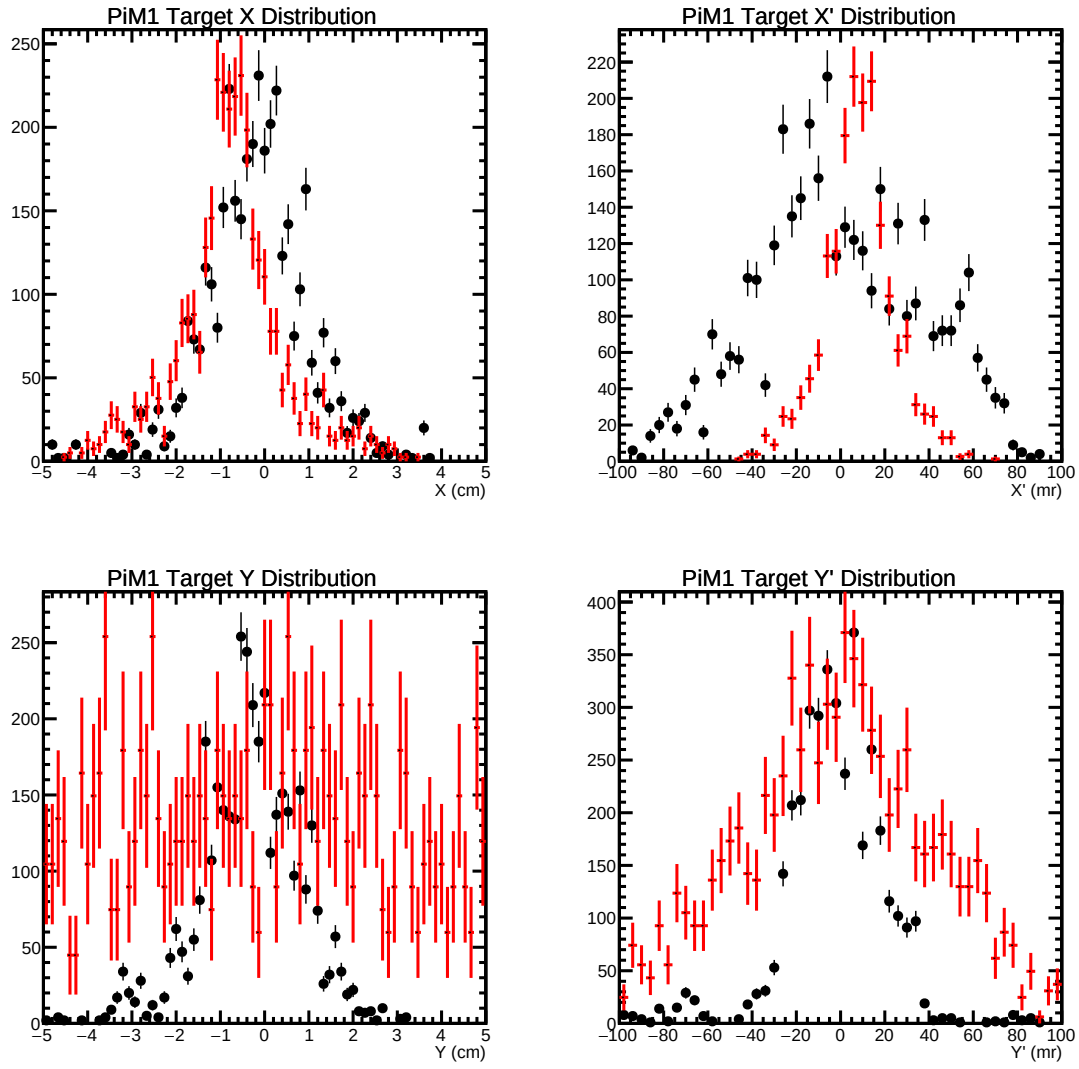

Figure 5.17: A comparison between TURTLE and experimental data at the PiM1 target for muons. The TURTLE simulation is in red and the data is in black. ***Upper Left***: x distribution. ***Upper Right***: x' distribution. ***Lower Left***: y distribution. ***Lower Right***: y' distribution.

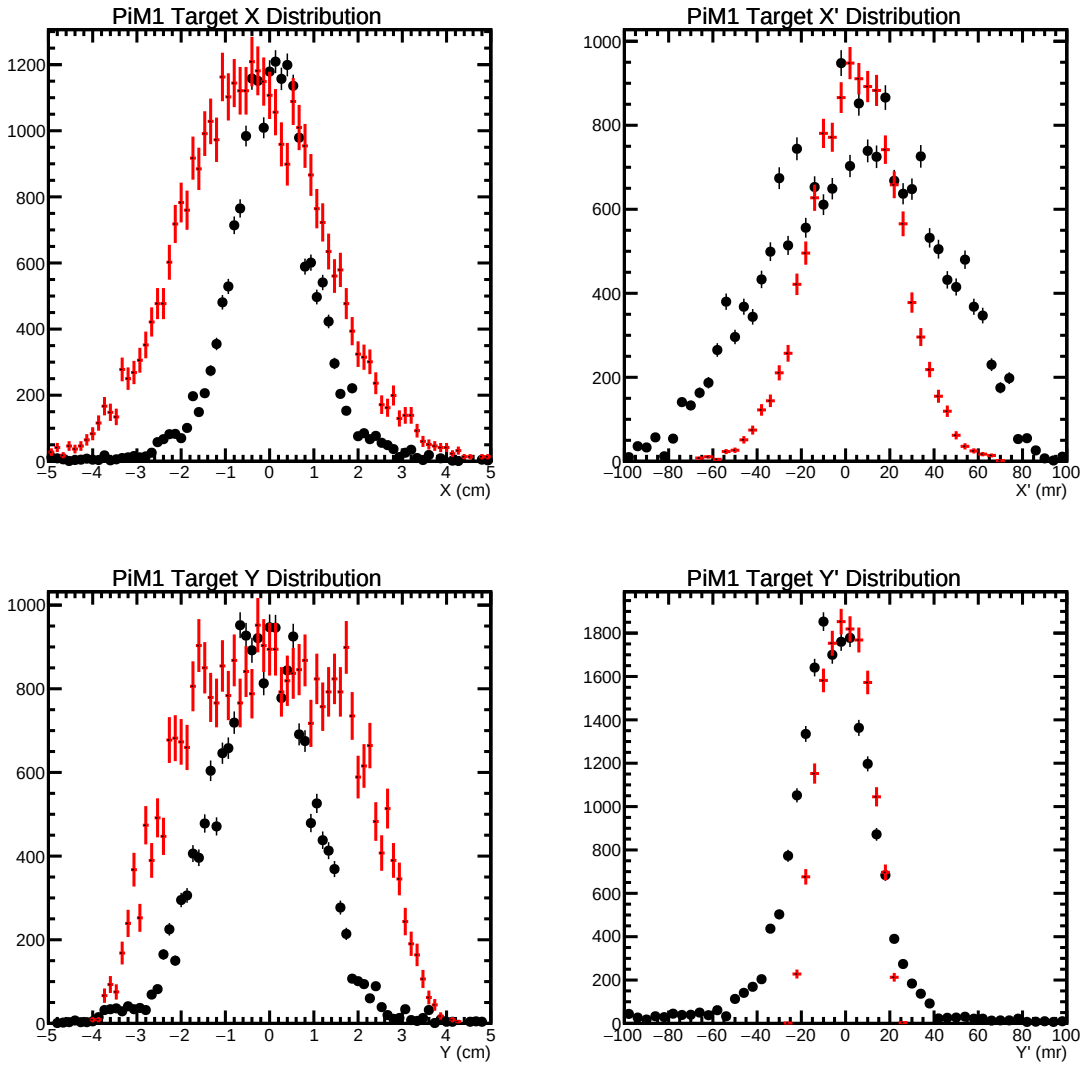

Figure 5.18: A comparison between TURTLE and experimental data at the PiM1 target for pions. The TURTLE simulation is in red and the data is in black. ***Upper Left***: x distribution. ***Upper Right***: x' distribution. ***Lower Left***: y distribution. ***Lower Right***: y' distribution.

To conclude, TURTLE and G4beamline provide a good qualitative description of the measured data, which perhaps would be improved if energy loss in material were better modeled. We expect G4beamline is more refined in its treatment of material effects, and the better description of the distributions at the target confirm this. The difference in y distributions might also be due in part to the GEM performance.

5.4 Time of Flight

As described in Sec. 4.4 and in Sec. 3.3.2 experimental TOF distributions were taken at all MUSE momenta with both positive and negative charge polarities. We used the standard technique of measuring the accelerator RF and comparing it to our BH timing to identify particle types. The timing difference between the BH and accelerator RF is modulated by the radio frequency of the accelerator; we call this time the "RF time". All particle types in RF time are well separated and can be used for PID purposes in our analysis. The "exclusivity cut", where only one event was measured in each timing detector, and the VETO cut were applied to the data and the pulse height distributions were studied to inform simulation cuts. For the data taking the collimator was set to a width of 1 cm. Since there is a 7 cm/% dispersion at the IFP by narrowing the collimator we are able to take a small 0.15% momentum bite of the beam. This momentum bite allows us to have an experimentally precise momentum with which we can compare simulation. The collimator was set to 5 different positions at the IFP so that for each central momenta of the PiM1 channel we could perform 5 momenta measurements. The data was analyzed by Win Lin and Shraddha Dogra of Rutgers University, and the final TOF analysis was performed by Steffen Strauch.

A detailed description of the analysis that extracts the path length, average speed, and energy loss in the simulation was written by Steffen and is provided in Appendix D for completeness.

Fig. 5.19 shows three example TOF spectra at various momenta for the L_1 detector setup. The bump seen in the 161 and 210 MeV/c panels at 19.5 ns comes from particles scattering from the scattering chamber. The TOF is taken from paddle 6 of plane D of the BH to paddle 1 of the BM. In all cases the TOF peaks for the three particle species are well resolved. In Fig. 5.20 we see three more example TOF spectra for the L_3 detector setup. The different geometry for this setup has pushed the background from chamber scattering at 161 MeV/c from 19.5 ns in setting L_1 to 25 ns.

In order to extract the momentum of the PiM1 channel, these experimental results must be carefully compared to simulation. We describe below the procedure to extract the momentum by comparing simulation and data.

- The path length must be extracted from simulation via the electron TOF.
- The average speeds of the muons and pions must be extracted using the path length determined by the electrons.
- The incident momentum must be corrected for energy loss mechanisms as the particles traverse the beam line.
- The simulation must be fit to the data in order to extract the central momentum of the channel.

Once the momentum is determined we show the tabulated results from our beam time and an overview of our understanding of the PiM1 channel momentum.

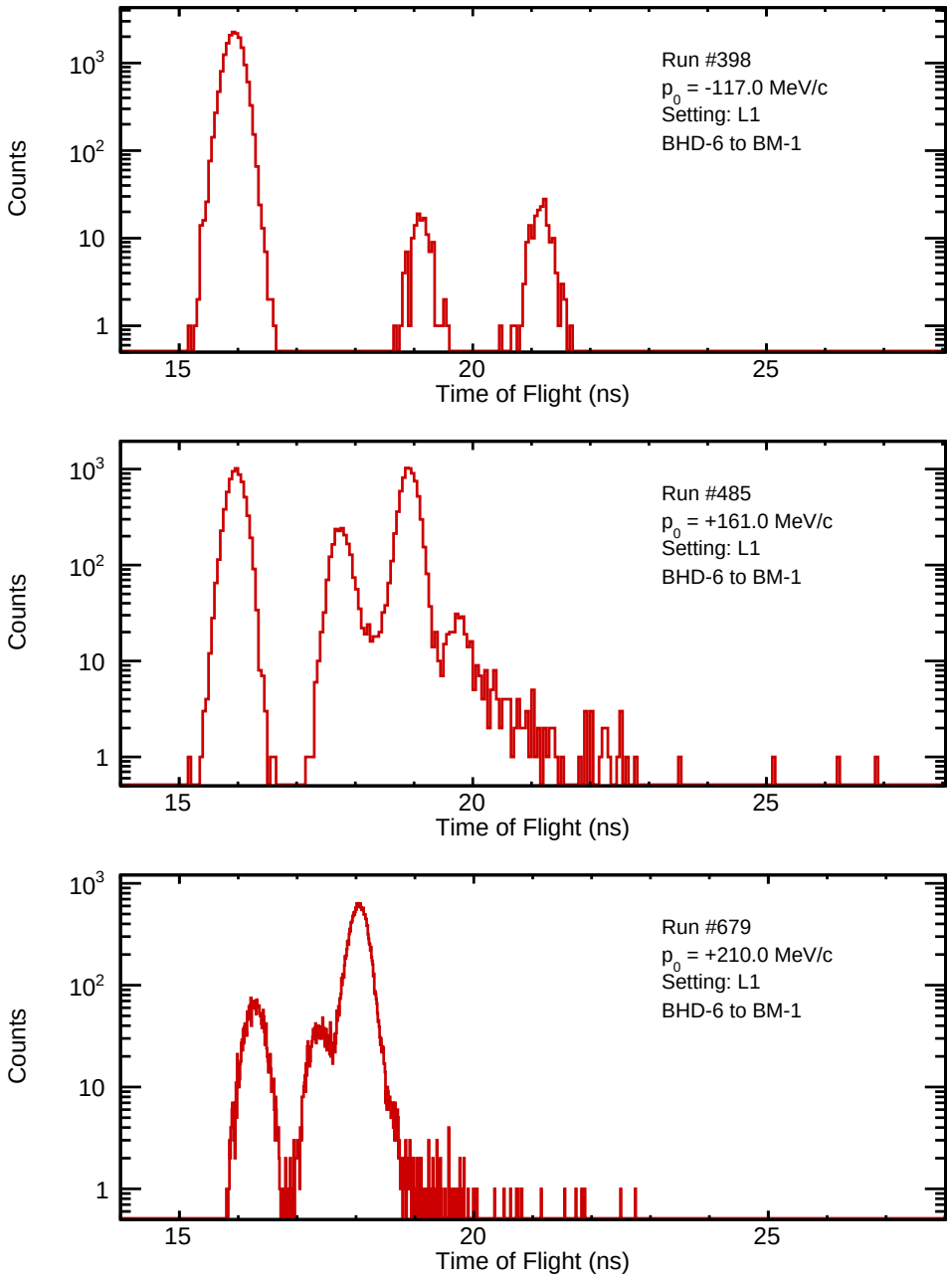

Figure 5.19: Three example spectra of the TOF from the beam-hodoscope, plane D, to the beam-monitor in the L_1 setting at nominal channel-momentum of 117, 161, and 210 MeV/c. From low to high TOF, the peaks correspond to electron, μ, and π particles. In these distributions, the TOF includes cable offsets. Courtesy of Steffen Strauch.

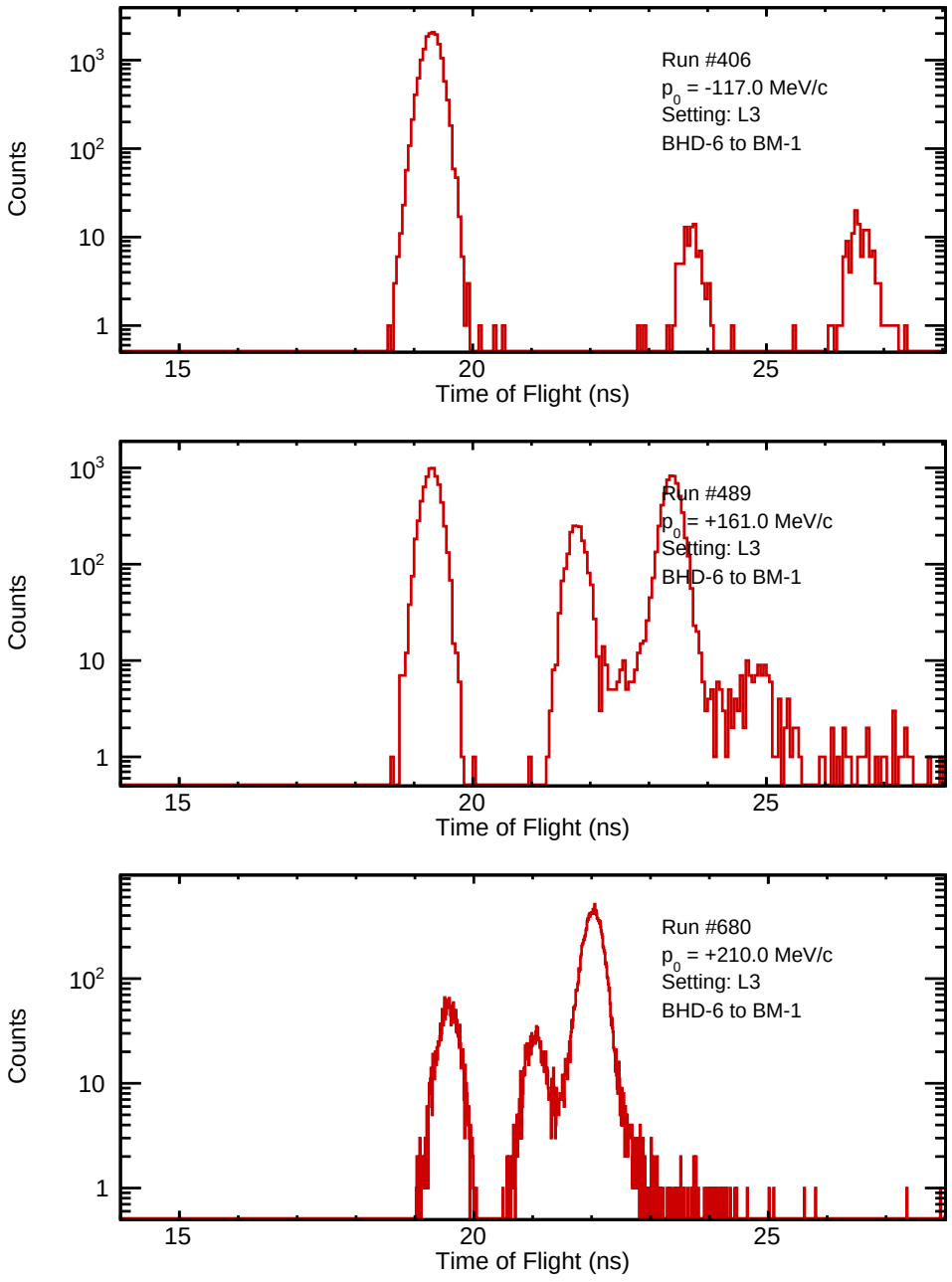

Figure 5.20: Three example spectra of the TOF from the beam-hodoscope, plane D, to the beam-monitor in the L_3 setting at nominal channel-momentum of 117, 161, and 210 MeV/c. From low to high TOF, the peaks correspond to electron, μ, and π particles. In these distributions, the TOF includes cable offsets. Courtesy of Steffen Strauch.

5.4.1 Fits

Once cuts were applied to simulation and experiment, the simulated TOF was folded with a gaussian distribution to include time resolution effects into the simulation. The simulation was then fit to the experimental data using a three parameter fit function. First the standard deviation σ of the Gaussian distribution that was used to fold the simulated spectrum. The second fit parameter, δ, determines the difference between the experimental and simulated distributions. Finally the third parameter is the normalization of the simulated data fit to the yield of the experiment.

Figs. 5.21 and 5.22 give examples of such fits. In this example, the channel momentum was set to 161 MeV/c momentum and negative polarity, the collimator was set to its central position, and flight times were measured from the BH paddle C9 to the BM bar one.

We see all three particle types in each panel of each figure. In order we have e, μ, and π. The side peaks in the μ distribution are random coincidences with other particle types. Fortunately from an analysis perspective, these side peaks are far enough from the main μ peak that they do not significantly impact the momentum extraction. The red curves are the full fits to the data with the parameters described above. The values of σ and δ are shown in the label. The green histograms show the simulation output for comparison with the δ offset applied but not the folded resolution. The peaks are arbitrarily scaled to half the height of the data peaks for ease of viewing. We also provide a gaussian fit to the data as a dashed line on the histogram.

We find an overall σ of ≈ 125 ps. This corresponds to the complete TOF resolution of the entire MUSE experimental apparatus. MUSE requires an overall TOF resolution of < 100 ps, which had been achieved at previous beam times. To verify our expected TOF resolution, the TOF resolution between combinations of individual paddles in the BH was studied. Since BH planes C and D are directly adjacent and oriented perpendicular to each other we can extract a TOF resolution between the two with approximately no geometric resolution effects. The two detectors form a cross with an overlap of 4 mm $\times$ 4 mm. The TOF resolution between individual paddle combinations in these two planes is ≈ 130 ps. If we assume that each paddle has the same timing resolution than this TOF resolution is worse than the paddle resolution by a factor of $\sqrt{2}$. Each BH paddle therefore has a resolution of ≈ 93 ps. From testing at the University of South Carolina it is expected that the BM bars have a timing resolution of at most 40 ps. By adding the timing resolution of the BH and BM in quadrature we expect a TOF resolution of the system to be ≈ 101 ps. This leads us to believe that the ≈ 125 ps resolution found in this analysis is broadened mostly due to the geometric and multiple scattering effects of an improperly positioned beam.

We can see from Figs. 5.21 and 5.22 that the L_1 setting has a ≈ 7 ps worse timing resolution.

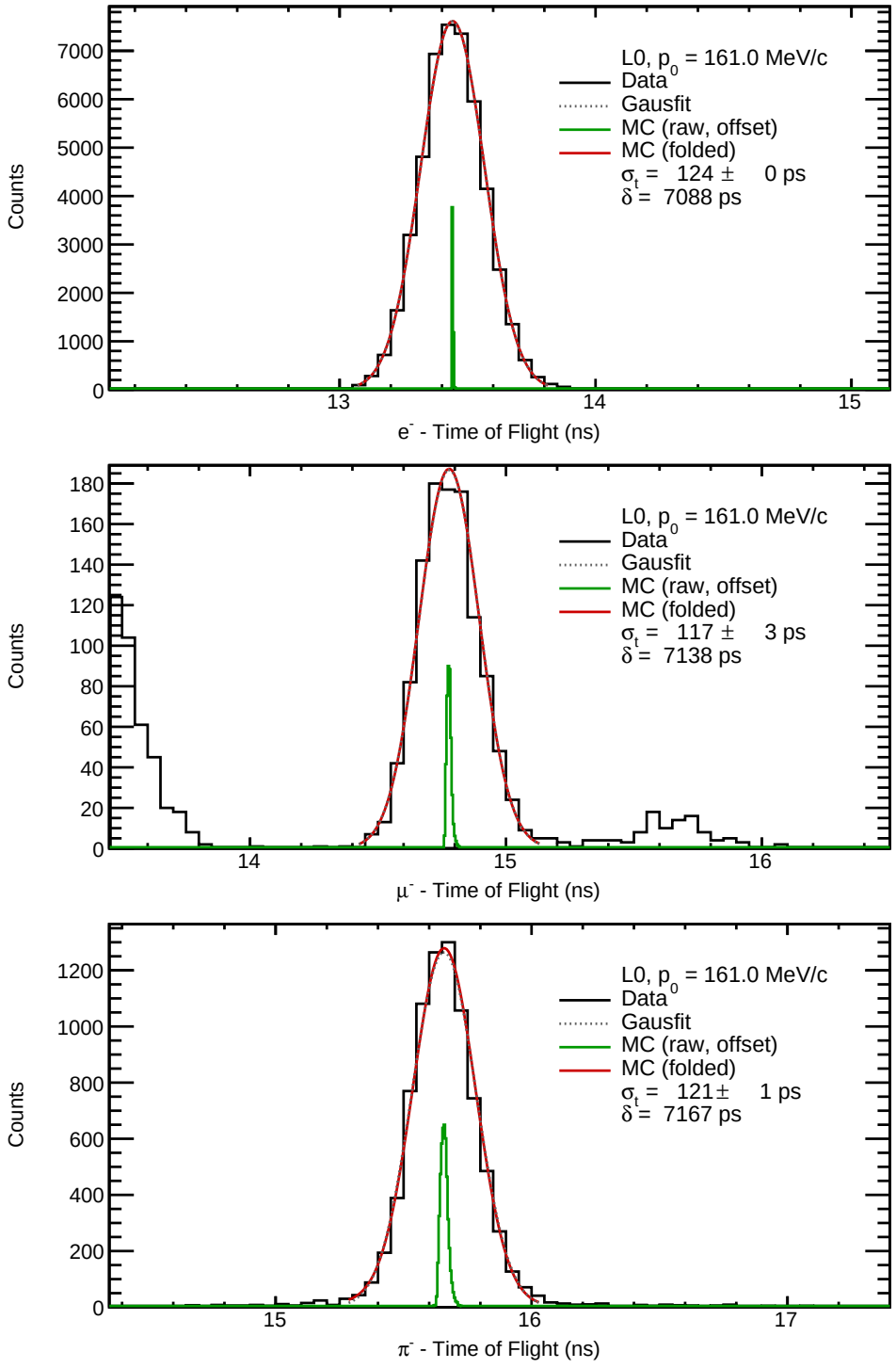

Figure 5.21: Three example spectra of fitted electron, muon, and pion time-of-flight spectra from the beam-hodoscope, paddle C9, to the beam-monitor paddle one in the L_0 setting at the nominal channel-momentum of 161 MeV/c. Courtesy of Steffen Strauch.

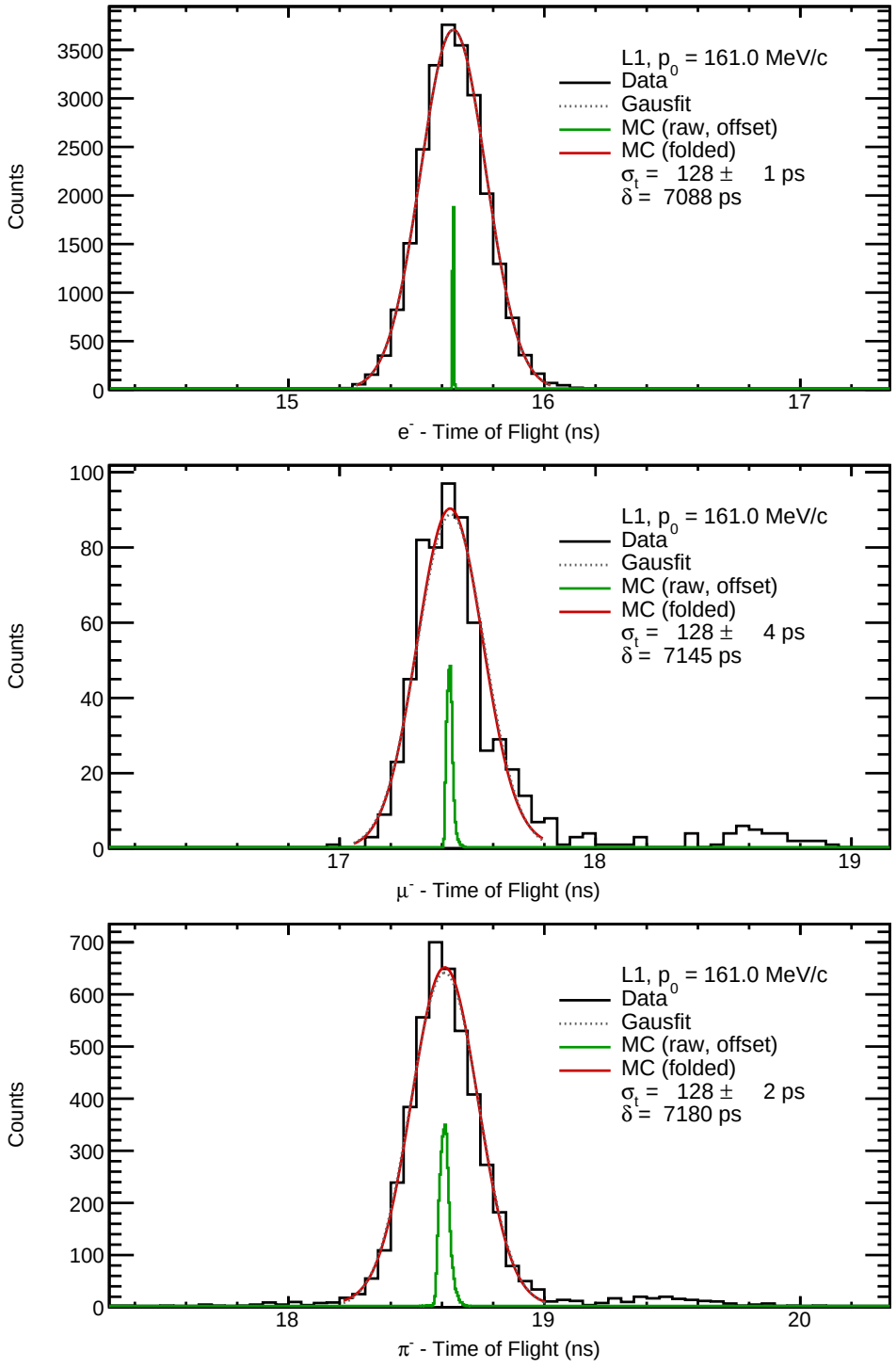

Figure 5.22: Three example spectra of fitted electron, muon, and pion time-of-flight spectra from the beam-hodoscope, paddle C9, to the beam-monitor paddle one in the L_1 setting at the nominal channel-momentum of 161 MeV/c. Courtesy of Steffen Strauch.

We know the background is higher in this configuration than the others but this is not a sufficient effect on the resolution to explain our poor overall resolution. We believe there is an additional unexplained background that has not been fully incorporated into the simulation. Unfortunately the final quadrupoles that were set to the wrong current polarities made our beam spot slightly larger than we typically expect. We generally needed to steer the beam for each momenta, it is likely we did not steer the beam as precisely as is needed.

The δ timing offsets are ≈ 7 ns, which are mostly cable and electronic delays, and most importantly are equal for both L_0 and L_1. This demonstrates the path length difference in the simulation well describes the experimental setup. Noting that the reference setting, L_0, has a larger value of δ for the muons and pions than for the electrons, shows that the momentum for the experimental measurements is less than the assumed momentum of the simulation. This is likely due to the additional momentum loss induced by the IFP GEMs.

Fig. 5.23 shows experimental measurements for all 4 measurement positions. The figure shows only one paddle combination, BH paddle C9 and BM paddle 1. The colored histograms show each particle type separated by RF timing and overlaid.

We see peaks underneath the electron peak that correspond to the other particle types. These are random coincidences that show up for the muons and pions. The colored cross hatching indicates a fit to particle types independently for each setting.

Following our procedure each particle type had its momentum extracted for each of the setups relative to the L_0 setup. Statistical uncertainties from fitted δ values, and uncertainties from simulated length, speed, and energy were propagated to find the statistical uncertainty on the momentum. The largest contribution to the uncertainty comes from δ. Results from the analysis are shown in Table 5.6, and the uncertainties are statistical only. The channel momentum was set to 161 MeV/c but as indicated above the actual momentum was slightly lower. This difference is almost entirely due to the IFP GEMs which induced energy loss not accounted for when the channel magnets were set. The energy loss due to these GEMs is detailed in Appendix A. This loss is not included in the Geant4 simulation of the experiment, but was corrected for with a value of 0.57 MeV/c for μ's and 0.74 MeV/c for pi's. Once the correction is applied we see excellent agreement, with extracted values of 160.4 ± 0.4 MeV/c and 159.9 ± 0.1 MeV/c for μ's and π's with statistical uncertainties of 0.25% and 0.1% respectively. This is below the required uncertainty of 0.3% for MUSE.

For the muons we are offset from the central channel momentum of 161 MeV/c by 0.37% and the pions are offset by 0.68%. However it is important to note that there is agreement between the relative momenta at the 0.3% level.

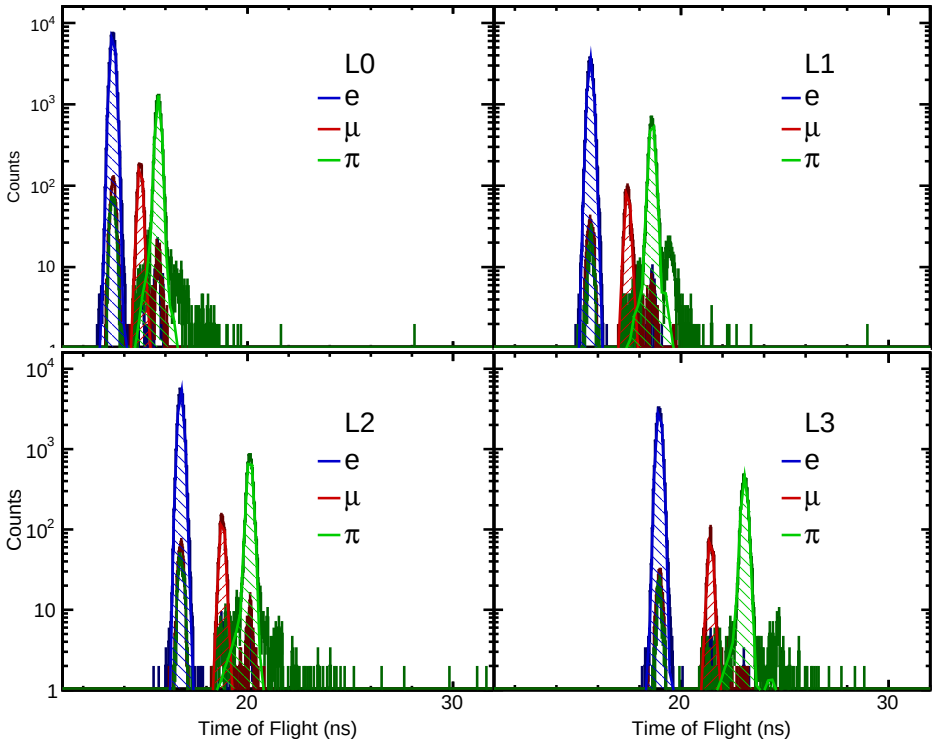

Figure 5.23: Summary of all fits to experimental time-of-flight spectra from the beam-hodoscope, paddle C9, to the beam-monitor paddle one for all detector positions L_0 through L_3. The nominal channel-momentum was set to 161 MeV/c, negative polarity. Courtesy of Steffen Strauch.

Setup	Δt_i^e (ps)	$c\Delta t_i^e$ (mm)	p_0^μ (MeV/c)	p_0^π (MeV/c)
ΔL_1	0.7 ± 1.0	0.2 ± 0.3	159.8 ± 1.3	159.6 ± 0.3
ΔL_2	-4.9 ± 0.9	-1.5 ± 0.3	160.1 ± 0.7	159.3 ± 0.2
ΔL_3	-9.6 ± 1.1	-2.9 ± 0.3	159.6 ± 0.5	159.2 ± 0.2
Average:			159.8 ± 0.4	159.2 ± 0.1
Average (incl. IFP energy-loss correction):			160.4 ± 0.4	159.9 ± 0.1

Table 5.6: Results of the analysis of the time-of-flight distributions in Fig. 5.23 for a nominal channel momentum of 161 MeV/c. The actual particle momentum at the IFP, however, was slightly lower due to energy losses in the GEM detector that was installed there; see Fig. A.2. Courtesy of Steffen Strauch.

5.4.2 Comparison Between TOF Simulation and Data

Nearly all TOF data from the August 2018 beam time has been analyzed, the data sets cover all momentum and polarity settings. An overview of the analysis effort is presented in Table 5.7.

#	x_c (mm)	$(dp/p)_c$	dL_1 (mm)	p_μ (MeV/c)	p_π (MeV/c)	$(dp/p)_\mu$	$(dp/p)_\pi$
				$p_0 = -117$ (MeV/c)			
1	−70	+1%	-3.14 ± 2.02	119.20 ± 0.33	119.11 ± 0.40	1.0%	0.9%
2	−35	+0.5%	-2.34 ± 1.40	117.92 ± 0.55	117.93 ± 0.36	−0.1%	−0.1%
3	0	0%	2.05 ± 2.01	118.00 ± 0.70	118.04 ± 0.44	0.0%	0.0%
4	35	−0.5%	-1.62 ± 4.01	117.17 ± 0.57	116.79 ± 0.29	−0.7%	−1.1%
				$p_0 = -161$ (MeV/c)			
5	−35	+0.5%	32.96 ± 1.17	169.35 ± 0.88	169.69 ± 0.37	5.7%	6.0%
6	0	0%	-1.96 ± 1.39	160.19 ± 0.70	160.13 ± 0.25	0.0%	0.0%
7	35	−0.5%	-7.99 ± 2.15	163.07 ± 0.72	163.09 ± 0.40	1.8%	1.9%
				$p_0 = +161$ (MeV/c)			
8	−35	+0.5%	2.94 ± 2.34	161.27 ± 0.57	161.68 ± 0.19	0.5%	0.6%
9	0	0%	0.34 ± 2.69	160.39 ± 0.54	160.66 ± 0.16	0.0%	0.0%
10	35	−0.5%	-4.84 ± 3.66	160.08 ± 0.45	159.77 ± 0.21	−0.2%	−0.6%

Table 5.7: Summary of the results of the analysis of nine sets of Summer 2018 time-of-flight data for various channel momenta and polarity, p_0, as well as collimator positions, x_c. We also show the momentum relative to the central momentum we select using that collimator position $(dp/p)_c$. We show the difference between the path length in the simulation and the extracted length using e TOF for $L_1 - L_0$, dL_1. The extracted momenta p_μ and p_π have been corrected for energy losses in the GEM at the IFP given in Appendix A. The momentum extraction for the μ's and π's relative to the central momentum is shown in the final two columns. Courtesy of Steffen Strauch.

In table 5.7 we show the TOF results from our analysis of the 2018 data. Settings with insufficient statistics or fits that do not converge were not included here, typically 15 combinations of BH and BM paddles contributed to one line on the table. We found several data sets were discarded as the path length extracted indicated that our timing detectors had not been accurately positioned. In some cases this mismatch was noted in the log books but not in every case. Typically position determinations from the electrons were off by 35 to 50 mm if the detectors were incorrectly positioned. Such a distance is too large to be an error in our extraction.

Typically we find that the pion momentum was extracted with an uncertainty of 0.1% to 0.3%. For muons the uncertainty is larger, generally about 0.5%, but this is dominated by statistical uncertainty. Comparing muon to pion momentum shows an agreement of 0.3%; for roughly half of the analyzed sets the agreement is 0.1%. Agreement at this level indicates that, once we have increased statistics, we should be able to reach our required uncertainty. With a TOF momentum extraction at this level of precision, MUSE is well prepared to measure the charge radius.

We also note that there is not good agreement with extracted momenta and expected momenta given the collimator setting. At the time of the measurement, it was known that there were issues with the collimator power supply and position readback. The operation of the collimator was therefore not entirely reliable. We note that good agreement between collimator position and momentum extracted is demonstrated in lines 8 and 10 in table 5.7.

5.4.3 Discussion

The TOF analysis has demonstrated that we will be able to determine muon and pion momenta to the precision necessary to run MUSE. There is still room for improvement in future measurements. Most notably removing the GEM detectors from the IFP would improve the quality of our measurements significantly. The improvement in our DAQ system noted in Sec. 3.2 will allow us to collect statistically significant data for all detector combinations in short order. Future measurements would also have the current polarities of the last two quadrupoles fixed so our beam would be properly focused and not multiple scattering off of the VETO.

In Table 5.7 approximately 15 BH and BM combinations contributed to a single entry. If we are able to instead take statistically significant data for every individual combination we could provide an estimate of systematic effects.

Going forward we are implementing a system of position sensitive electronics that will indicate in the slow controls where each detector is positioned. This will allow us to control the positions of our detectors more precisely than was done in the data collected thus far.

Chapter 6
Conclusion and Outlook

We have demonstrated that we can experimentally measure differences in the distributions of electrons, muons, and pions in the PiM1 beamline. These data, compared with simple estimates of matrix elements from TURTLE, suggest that particles from the channel have very similar average momentum, with differences no more than of order 0.1%. The differences can be described by a simple Geant4 simulation of material at the IFP to within 0.05%, as shown in Sec. 5.2.2, and our understanding of the PiM1 matrix elements from TURTLE, seen in Sec. 4.2. This good agreement between simulation and experiment allows us to conclude that particles traversing the PiM1 beam line bend uniformly through the ASM12 dipole. As dipoles select particles with the same momentum we can reasonably conclude that all particles traverse the beam line in a similar manner, once production source distributions are taken into account. Detailed descriptions of the source production mechanisms and source distributions for electrons and muons were shown in Sec. 4.1.

Furthermore, we have shown in Secs. 5.3 and 5.3.1 that beam distributions at the IFP and the PiM1 target location measured in the summer 2018 data are in reasonable agreement with the TURTLE and G4beamline simulations. Exact agreement is not expected for such simulations as each describes the beam line in a fundamentally different way. Both simulations also describe the dipoles differently, and the G4beamline description is not yet complete. It appears that the better treatment of energy loss in G4beamline compared to in TURTLE leads to better agreement with target distributions than we get with TURTLE. Apparently this effect is more important than the better description of the magnetic fields in TURTLE. These results indicate that we have a good understanding of the beam line and our data. Further improvements are expected as we fine-tune the dipole field maps and improve the data analysis procedures.

We also note that both G4beamline and TURTLE are in fair agreement with each other when comparing production source size and IFP and PiM1 target distribution sizes when comparing default configurations shown in Sec. 4.3. The good agreement of the simulations with each other and the data gives confidence that the electron beam source is small and the properties of electron and pion beams are consistent with each other.

Going forward a number of improvements are planned and several have already been implemented. Our DAQ system has been improved substantially with a decrease in read-out time and consequently an increase in rate capability. We will be implementing a system of position sensitive electronics to monitor detector position. The PiM1 magnetic channel is currently being upgraded with high performance power supplies that can control current, and consequently stabilize magnetic field strength, at the 0.01% level. The polarity of the final quadrupoles will be corrected. As part of the upgrade to the PiM1 channel, the length of the IFP exposed to air is being reduced slightly to reduce energy loss, and thereby minimize the impact of any energy loss modeling uncertainty.

In future measurements we will not place any detectors at the IFP. Generally these GEM chambers complicated the analysis and did not provide significant improvements to our data quality. This also eliminates the need to manually steer the beam as it enters PiM1. A properly focused and steered beam will improve data for all measurements.

Looking forward we will attempt to measure TOF again in the summer of 2019 with the improvements discussed in Sec. 5.4. We have thoroughly demonstrated that we can measure the momentum of the beam to within 0.1% relative uncertainty for pions and 0.25% for muons with our measurement technique. We also see an agreement of the relative momenta of 0.3% or better. Our models of the beam provide a good approximation of the data and demonstrate we have the systematics of the experiment well under control for the proton charge radius measurement that will be performed by MUSE.

With our understanding of the beam line under control, MUSE is well suited to make a high-precision measurement of the proton charge radius. We can measure precisely a charge radius from both electron-proton and muon-proton elastic scattering. As shown, using the simultaneous measurement of electron and muon scattering, many systematic effects cancel. This enables a high-precision determination of the radius difference and any differences in the lepton interactions. By comparing measurements with both beam polarities we can directly measure the two-photon effect, in both muons and electrons. Being able to measure the two-photon effect with the same experimental apparatus for both leptons allows a thorough test of the theory with reduced systematic uncertainties. This will allow us to either rule out or support enhanced two photon effect theories of the underlying radius puzzle. MUSE is well positioned to make key measurements that will shed light on the proton radius puzzle, and provide a test of lepton universality.

Bibliography

[1] Agostinelli, S., et al. 2003, Nucl. Instrum. Meth., A506, 250

[2] Antognini, A., Nez, F., Schuhmann, K., et al. 2013, Science, 339, 417

[3] Barger, V., Chiang, C.-W., Keung, W.-Y., & Marfatia, D. 2011, Phys. Rev. Lett., 106, 153001

[4] Barger, V., Chiang, C.-W., Keung, W.-Y., & Marfatia, D. 2012, Phys. Rev. Lett., 108, 081802

[5] Bennett, G. W., Bousquet, B., Brown, H. N., et al. 2006, Phys. Rev. D, 73, 072003

[6] Berg, F., Desorgher, L., Fuchs, A., et al. 2015, Physical Review Accelerators and Beams, 19, doi:10.1103/PhysRevAccelBeams.19.024701

[7] Bernauer, J. C., Achenbach, P., Ayerbe Gayoso, C., et al. 2010, Phys. Rev. Lett., 105, 242001

[8] Beyer, A., Maisenbacher, L., Matveev, A., et al. 2017, Science, 358, 79

[9] Brun, R., & Rademakers, F. 1997, Nucl. Inst. & Meth. in Phys. Res. A, 389, 81

[10] Carlson, C. E., & Vanderhaeghen, M. 2007, Annual Review of Nuclear and Particle Science, 57, 171

[11] Cockcroft, J. D., & Walton, E. T. S. 1932, Nature, 129, 242

[12] Cockcroft, J. D., & Walton, E. T. S. 1932, Nature, 129, 649

[13] Deiters, K. 2013, PiM1 Beam Line, `http://aea.web.psi.ch/beam2lines/beam_pim1.html`

[14] Fleurbaey, H., Galtier, S., Thomas, S., et al. 2018, Phys. Rev. Lett., 120, 183001

[15] French, M., Jones, L., Morrissey, Q., et al. 2001, Nucl. Inst. & Meth. in Phys. Res. A, 466, 359, 4th Int. Symp. on Development and Application of Semiconductor Tracking Detectors

[16] Gilman, R., et al. 2013, arXiv:1303.2160

[17] Gilman, R., Downie, E. J., Ron, G., et al. 2017, ArXiv e-prints, arXiv:1709.09753

[18] Griffioen, K., Carlson, C., & Maddox, S. 2016, Phys. Rev. C, 93, 065207

[19] Heidenreich, G. 2002, AIP Conference Proceedings, 642, 122

[20] Hofstadter, R. 1956, Rev. Mod. Phys., 28, 214

[21] Karplus, R., Klein, A., & Schwinger, J. 1952, Phys. Rev., 86, 288

[22] Kelly, J. 2004, Phys.Rev., C70, 068202

[23] Knecht, A. 2017, private communication

[24] Koshchii, O., & Afanasev, A. 2017, Phys. Rev. D, 96, 016005

[25] Kraus, E., Mesick, K. E., White, A., Gilman, R., & Strauch, S. 2014, Phys. Rev. C, 90, 045206

[26] Krauth, J. J., Schuhmann, K., Abdou Ahmed, M., et al. 2017, arXiv e-prints, arXiv:1706.00696

[27] Lee, G., Arrington, J. R., & Hill, R. J. 2015, Phys. Rev. D, 92, 013013

[28] Liu, Y.-S., McKeen, D., & Miller, G. A. 2016, Phys. Rev. Lett., 117, 101801

[29] Liu, Y.-S., & Miller, G. A. 2015, Phys. Rev. C, 92, 035209

[30] Liyanage, A., Kohl, M., Nazeer, J., & Patel, T. 2018, in 5th International Conference on Micro Pattern Gas Detectors (MPGD2017) Temple University, Philadelphia, USA, May 22-26, 2017

[31] Maximon, L. C., & Tjon, J. A. 2000, Phys. Rev. C, 62, 054320

[32] Mesytec. 2019, MCFD-16, `https://www.mesytec.com/products/datasheets/MCFD-16.pdf`

[33] Mesytec. 2019, MQDC-32, `https://www.mesytec.com/products/datasheets/MQDC-32.pdf`

[34] Miller, G. A. 2013, Physics Letters B, 718, 1078

[35] Mohr, P. J., Taylor, B. N., & Newell, D. B. 2012, Rev. Mod. Phys., 84, 1527

[36] Pohl, R., Gilman, R., Miller, G. A., & Pachucki, K. 2013, Annual Review of Nuclear and Particle Science, 63, 175

[37] Pohl, R., Antognini, A., Nez, F., et al. 2010, Nature, 466, 213

[38] Przyborowski, D., Fiutowski, T., Idzik, M., et al. 2016, Journal of Instrumentation, 11, P08009

[39] Roberts, T. 2018, `http://www.muonsinternal.com/muons3/G4beamline`

[40] Rosenfelder, R. 2000, Physics Letters B, 479, 381

[41] Roy, P., Corsetti, S., Dimond, M., et al. 2019, arXiv e-prints, arXiv:1907.03022

[42] Schumacher, R., & Sennhauser, U. 1987

[43] Sick, I. 2003, Physics Letters B, 576, 62

[44] Tomalak, O., & Vanderhaeghen, M. 2014, Phys. Rev. D, 90, 013006

[45] Traxler, M., Bayer, E., Kajetanowicz, M., et al. 2011, Journal of Instrumentation, 6, C12004

[46] Tsai, Y.-S. 1961, Phys. Rev., 122, 1898

[47] Tucker-Smith, D., & Yavin, I. 2011, Phys. Rev. D, 83, 101702

[48] Ugur, C., Neiser, A., Adamczewski-Musch, J., et al. 2013, in

[49] Zhan, X., Allada, K., Armstrong, D., et al. 2011, Physics Letters B, 705, 59

Appendices

Appendix A
Momentum Loss Simulations

In this Appendix we show the Geant4 simulations of how the momentum spectra of beams of different particles are changed by energy loss effects at the IFP. Note that the vertical scale of the plots is logarithmic. In all cases we start with a monochromatic pencil beam. The simulations are done both with and without GEM planes installed. The initial momentum is shown in red. The momentum distribution after passing through the IFP material is in black. The range of the plots is limited to particles likely to be able to pass through the ASM12 bending dipole and reach the target region. We show only a pencil beam with no dispersion; a full simulation with up to ± 0.05% momentum dispersion showed less than a 10^{-3} effect on the mean momentum loss.

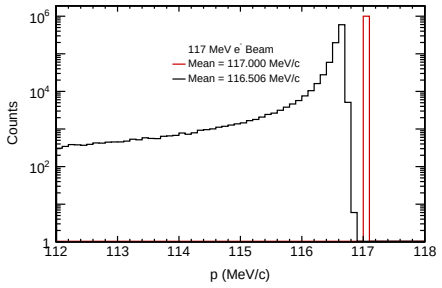

(a) e momentum loss.

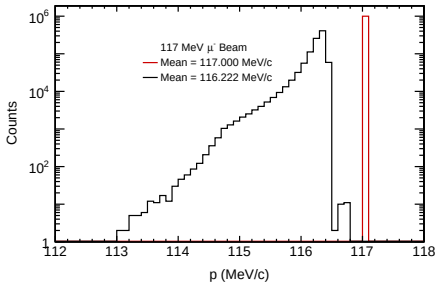

(b) μ momentum loss.

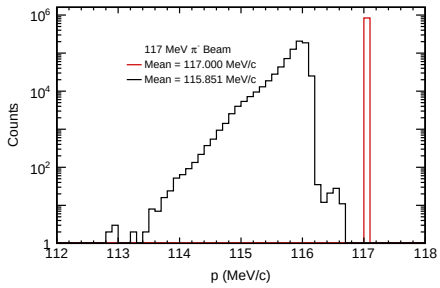

(c) π momentum loss

Figure A.1: Momentum loss using a $-117\,\mathrm{MeV/c}$ pencil beam through the IFP with GEMs.

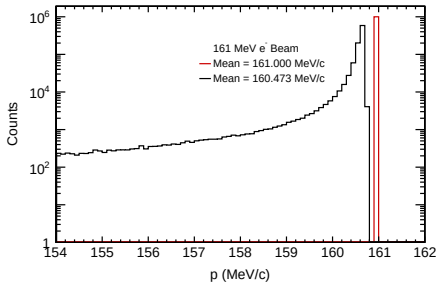

(a) e momentum loss.

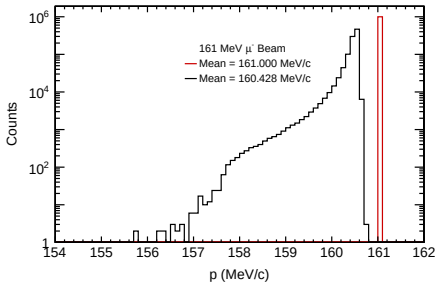

(b) μ momentum loss.

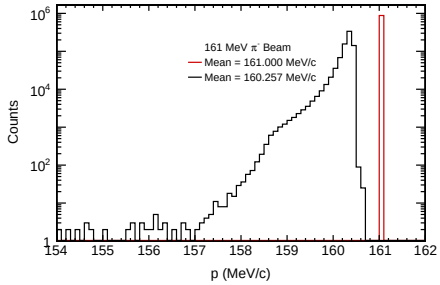

(c) π momentum loss

Figure A.2: Momentum loss using a $-161\,\mathrm{MeV/c}$ pencil beam through the IFP with GEMs.

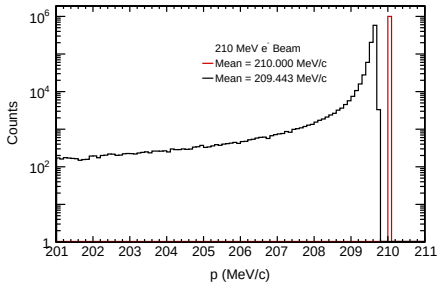

(a) e momentum loss.

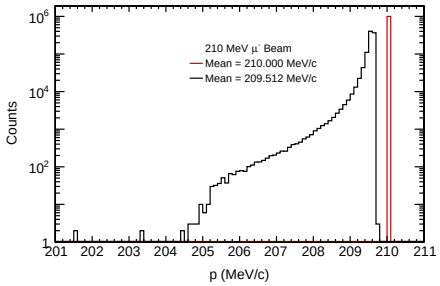

(b) μ momentum loss.

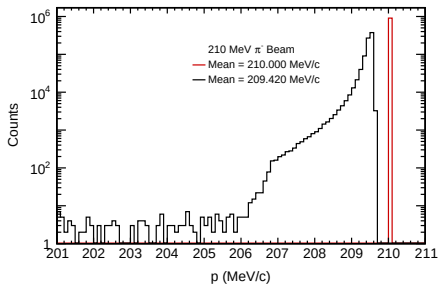

(c) π momentum loss

Figure A.3: Momentum loss using a $-210\,\mathrm{MeV/c}$ pencil beam through the IFP with GEMs.

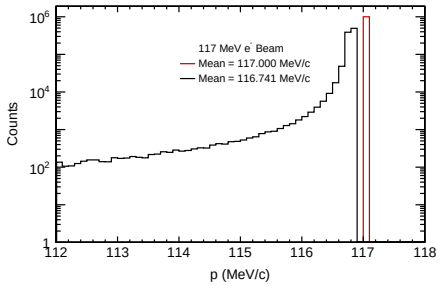

(a) e momentum loss.

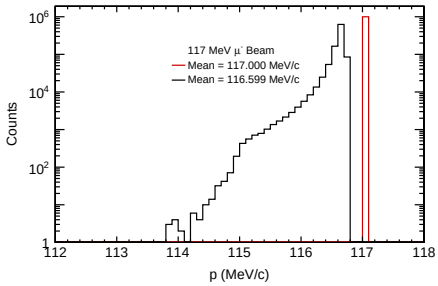

(b) μ momentum loss.

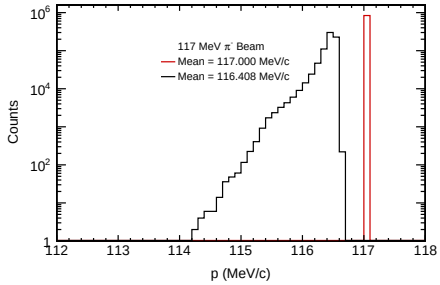

(c) π momentum loss

Figure A.4: Momentum loss using a $-117\,\mathrm{MeV/c}$ pencil beam through the IFP, without GEMs.

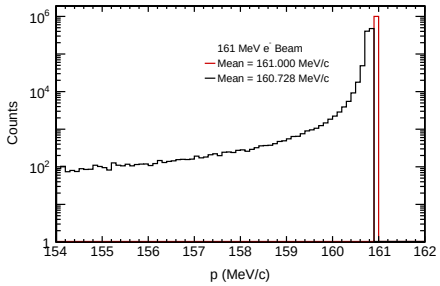

(a) e momentum loss.

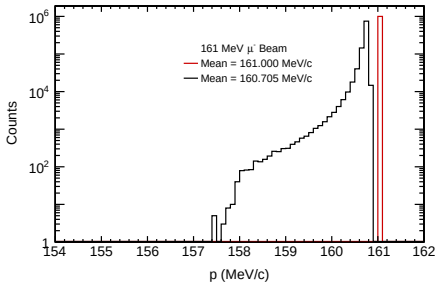

(b) μ momentum loss.

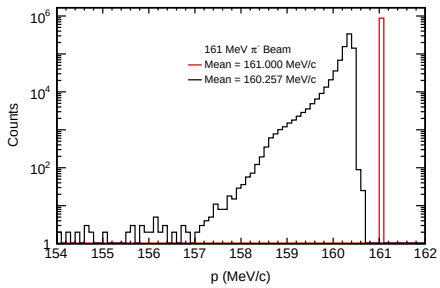

(c) π momentum loss

Figure A.5: Momentum loss using a $-161\,\mathrm{MeV/c}$ pencil beam through the IFP, without GEMs.

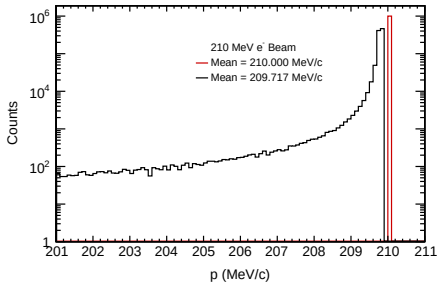

(a) e momentum loss.

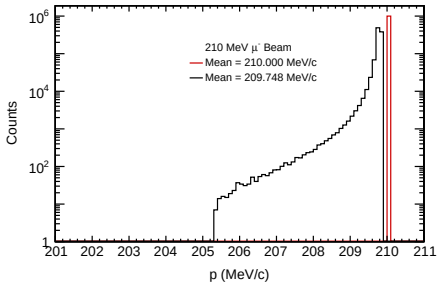

(b) μ momentum loss.

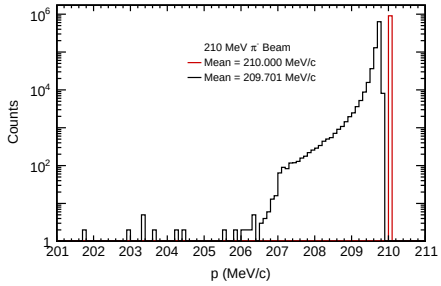

(c) π momentum loss

Figure A.6: Momentum loss using a $-210\,\mathrm{MeV/c}$ pencil beam through the IFP, without GEMs.

Appendix B
Turtle Input Deck

We use TURTLE-DECAY, but for this study we only consider parent particles. Our standard TURTLE input deck for a nearly point-like muon beam being transported by PiM1 follows. Parentheses and slashes serve to define comments. Each line begins with a code indicating what the line is defining:

- 1: defines the beam
- 3: defines drifts through a field-free region
- 4: defines bending magnets,
- 5: defines quadrupole magnets,
- 6: defines slits,
- 7: defines shifts of the beam center (used, e.g., for asymmetric slits),
- 9: defines a repeating region of code, and
- 16: defines various calculation parameters.

Details of the definitions can be found in the TURTLE manual, however there are multiple versions of the manual due to the extensive history of TURTLE. PSI maintains online descriptions not available in many manuals, which are available on its internal network through `http://pc102.psi.ch`. We have suppressed histogram definitions for brevity.

```
/MUSE 155MeVc parent muons/
(Number of Particles)
 1000000
(Aperture Constraints)
13. 10. ;
13. 110. ;
(Units Changes from Default)
```

```
15. 11. /MeVc/ 0.001 ;
15. 12.0 /MeV/ 0.001 ;
(Take homogeneous beam distribution instead of gaussian)
16. 20. ;
(Seed for random generator fixed for each run at the same value)
16. 30. 5. ;
(Parent Particle Mass)
(16. 3. 1. /e/ ;)
16. 3. 105.66 /Mu/ ;
(16. 3. 139.57 /Pi/ ;)
(Switch on Multiple Scattering - 165 = MS on, 166 = MS off = default)
16. 165. /mult/ ;
(16. 166. /mult/ ;)
(Beam Definition)
1. 0.1 30.0 0.1 80.0 0.0 1.5 155. /BEAM/ ;
(Switch on Second Order)
17. /SECO/ ;
(Design Momentum)
16. 11. 155. /P0_2/ ;
(Drift: distance between Production-Target-M and QTA11)
6. 1. 16. 3. 16. ;
3. 0.958 ;
6. 1. 16. 3. 16. ;
(QTA11)
16. 101. 7.5 ;
2. 1000. ;
5. 0.324 -0.9854 7.5 /QTA1/ ;
2. 1000. ;
(Drift)
6. 1. 16. 3. 16. ;
3. 0.131 ;
6. 1. 16. 3. 16. ;
(QTB11)
16. 101. 11.5 ;
2. 1000. ;
5. 0.475 -1.0894 11.5 /QTB1/ ;
2. 1000. ;
```

```
(Drift)
6. 1. 16. 3. 16. ;
3. 0.110 ;
6. 1. 16. 3. 16. ;
(QTB12)
16. 101. 11.5 ;
2. 1000. ;
5. 0.475 1.1965 11.5 /QTB2/ ;
2. 1000. ;
(Drifts)
6. 1. 16. 3. 16. ;
3. 0.176 ;
6. 1. 16. 3. 16. ;
3. 1.0 ;
6. 1. 16. 3. 16. ;
3. 1.0 ;
6. 1. 16. 3. 16. ;
3. 1.0 ;
6. 1. 16. 3. 16. ;
3. 1.0 ;
6. 1. 16. 3. 16. ;
(FS11 slits, in x then y. Estimate)
9. 100. ;
  6. 1.0 8. ;
  1. 14.266 12.30 5.0 0.730 980.2 0.622 2.921 0.0 /Cu/ ;
  3. .001 ;
9. 0. ;
9. 100. ;
  6. 3.0 8. ;
  1. 14.266 12.30 5.0 0.730 980.2 0.622 2.921 0.0 /Cu/ ;
  3. .001 ;
9. 0. ;
(3. 0.334 /DR5/ ;)
(Drift)
6. 1. 16. 3. 16. ;
3. 0.653 ;
6. 1. 16. 3. 16. ;
```

```
(ASM11)
6. 3. 5. ;
16. 5.0 6.0 ;
16. 7.0 0.45 ;
16. 8.0 2.8 ;
16. 12.0 0.55 /R11/ ;
16. 13.0 -0.8 /R12/ ;
2. 27.9 /WE11/ ;
4. 0.77539 4.3641 0.0 /ASM1/ ;
6. 3. 3.6 ;
4. 0.77539 4.3641 0.0 /ASM1/ ;
2. 27.9 /WE12/ ;
6. 3. 5. ;
(Drift to KSD11)
6. 1. 16. 3. 16. ;
3. 0.818 ;
6. 1. 16. 3. 16. ;
(Drift to QSL11)
6. 1. 16. 3. 16. ;
3. 0.539 ;
6. 1. 16. 3. 16. ;
(QSL11)
16. 101. 12. ;
2. 1000. ;
5. 0.59 -1.2731 12.0 /QSL1/ ;
2. 1000. ;
3. 0.112 ;
(QSL12)
16. 101. 12. ;
2. 1000. ;
5. 0.59 0.9086 12.0 /QSL2/ ;
2. 1000. ;
(Drift to DR8)
6. 1. 16. 3. 16. ;
3. 1.018 /DR8/ ;
(3. 0.689 /DR8/ ;)
6. 1. 16. 3. 16. ;
```

```
(Horizontal Beam Shift in cm before the slit - to model IFP collimator)
(7. -3.0 0.0 0.0 0.0 0.0 0.0 ;)
(Slit is open)
9. 100. ;
  6. 1.0 10. ;
  1. 14.266 12.30 5.0 0.730 980.2 0.622 2.921 0.0 /Cu/ ;
  3. .001 ;
 9. 0. ;
(Shift Beam back after slit)
(7. 3.0 0.0 0.0 0.0 0.0 0.0 ;)
(Carbon Absorber)
(16. 160. ;)
(9. 5. ;)
(  6. 50.0 50.0 ;)
  (1. 3.564 9.70 49.62 0.660 525.95 0.053 0.241 0.0 /C_Pi/ ;)
  (1  3.277 9.54 49.62 0.660 525.95 0.046 0.217 0.0 /C_Mu/ ;)
(  3. .001 ;)
( 9. 0. ;)
(16. 161 ;)
(Dump Distribution to FOR070.DAT file)
(16. 181.0 70.0 0. ;)
(Drifts)
6. 1. 16. 3. 16. ;
3. 0.412 ;
6. 1. 16. 3. 16. ;
(QLS13)
16. 101. 12. ;
2. 1000. ;
5. 0.59 0.9086 12.0 /QSL3/ ;
2. 1000. ;
(Drift)
6. 1. 16. 3. 16. ;
3. 0.112 ;
6. 1. 16. 3. 16. ;
(QSL14)
16. 101. 12. ;
2. 1000. ;
```

```
5. 0.59 -1.2732 12.0 /QSL4/ ;
2. 1000. ;
(Drift)
6. 1. 16. 3. 16. ;
3. 1.311 ;
6. 1. 16. 3. 16. ;
(ASM12)
6. 3. 5.0 ;
16. 5.0 6.0 ;
16. 7.0 0.45 ;
16. 8.0 2.8 ;
16. 12.0 -0.8 /R21/ ;
16. 13.0 0.55 /R22/ ;
2. 27.9 /WE21/ ;
4. 0.77539 4.3641 0.0 /ASM2/ ;
6. 3. 3.6 ;
4. 0.77539 4.3641 0.0 /ASM2/ ;
2. 27.9 /WE22/ ;
6. 3. 5. ;
(Drift)
6. 1. 16. 3. 16. ;
3. 0.684 ;
6. 1. 16. 3. 16. ;
(QSL15)
16. 101. 12. ;
2. 1000. ;
5. 0.59 0.5440 12.0 /QSL5/ ;
2. 1000. ;
(Drift)
6. 1. 16. 3. 16. ;
3. 0.112 ;
6. 1. 16. 3. 16. ;
(QSL16)
16. 101. 12. ;
2. 1000. ;
5. 0.59 -0.7506 12.0 /QSL6/ ;
2. 1000. ;
```

```
(Drifts)
6. 1. 16. 3. 16. ;
3. 1.038 /DR16/ ;
6. 1. 16. 3. 16. ;
(QSL17)
16. 101. 12. ;
2. 1000. ;
5. 0.59 0.9086 12.0 /QSL7/ ;
2. 1000. ;
(Drift)
6. 1. 16. 3. 16. ;
3. 0.163 ;
6. 1. 16. 3. 16. ;
(QSL18)
16. 101. 12. ;
2. 1000. ;
5. 0.59 -1.2732 12.0 /QSL8/ ;
2. 1000. ;
(Drift)
6. 1. 16. 3. 16. ;
3. 1.536 /TARG/ ;
(Drift)
3. 2.0 ;
SENTINEL
SENTINEL
```

Appendix C
G4Beamline Input Deck

Here we provide the input file for the g4beamline simulation, which we created to compare this simulation with TURTLE. In this study, we only considered parent particles. The beam source is a nearly point-like muon beam with 155 MeV central momentum. The parameters of the beam source are read-in from an ASCII file called g4_in.txt. We have added comments to assist in understanding the code. They begin with a # sign. Note that we have introduced line breaks in some of the commands shown below so that they fit within the page. These line-breaks must be removed before compiling the code, otherwise it will fail to compile without errors. A detailed description of a typical input file is discussed in **Section** 4 of the G4beamline User's Guide (http://muonsinc.com/muons3/g4beamline/G4beamlineUsersGuide.pdf).

```
################################################################################
#   History:
#
#   Original author: L. Desorgher
#   Revised to match Turtle input deck the P Reimer (PER)
#   Revised to match Turtle by Priya, Univ. of Michigan (PRoy)
#   Dipole Fieldmaps revised to match ASM11 and ASM12 to Turtle (PER)

################################################################################


param -unset firstEvent=1
param -unset nEvents=100000
param -unset lastEvent=100000
param -unset beamPart=mu+

##### Define channel momentum
param -unset pChannel=155

##### Allow the user to specify a different momentum
```

```
param -unset pOffset=1.0

##### For beamline momentum other than 155, we scale current in the magnets
param scale=$pChannel/155

param -unset map1=ASM1.g4blmap
param -unset map2=ASM2.g4blmap

##### Add ability to scale magnets sets
param -unset scaleDipole=1.000295
param -unset scaleQSL=1
param -unset scaleQT=1

##### Define output file name and type
param sepChar="_"
param file=MuSEBeam_$beamPart$sepChar$pChannel$sepChar$pOffset
param histoFile=$file.root

##### Overwelming reccomendation was qgsp_bert_hp for physics engine
param -unset physicsName=QGSP_BERT_HP
physics $physicsName

param partName=$beamPart
param tuneP=abs($pChannel)
param -unset beamAngle=22.5
param zProdTarget=-958
param startZ=$zProdTarget

##### convert kG/mm to T/m
param kGpmm_to_Tpm=100

##### Quad iron shield parameters
param RIRON=800
param killInPipe=0
param pipeColor=0,1,1,0.4
param killInIron=1
param ironColor=1,0,0,0.4
```

```
param absorbAllColor=1,1,0,0.05
param killAllColor=$absorbAllColor
param -unset killInShield=1
param shieldColor=$killAllColor
particlecolor e+=1,1,1 e-=1,1,1 mu+=0,1,1 mu-=0,1,1

##### Track cuts to keep only mu+
trackcuts keep=mu+

collective
param worldMaterial=Vacuum
param maxstep=10 deltaChord=0.5
start x=0. y=0. z=0. initialZ=$startZ

##### Adjust centerline to 22 degrees
cornerarc z=$zProdTarget angle=$beamAngle centerRadius=10

##### Read-in the beam source from ASCII file
beam ASCII file=g4_in.txt

##### Define virtual detector plane
param MuSEDetColor=1,0,1,1
param MuSEDetLength=15
param MuSEDetRadius=500
virtualdetector MuSEDet radius=$MuSEDetRadius length=$MuSEDetLength color=$MuSEDetColor

##### Define QSL quadrupole magnets with rounded + aperture
param LQSL=590
param RQSL=120
genericquad QSL fieldLength=$LQSL coilHalfWidth=50 coilRadius=150 poleTipRadius=125
ironRadius=$RIRON ironLength=$LQSL kill=$killInIron ironColor=$ironColor
##### Remove the line-break between poleTipRadius and ironRadius before compiling

##### Define shielding tube
tubs SHIELD innerRadius=$RIRON*1.1 outerRadius=$RIRON*1.2 kill=$killInShield
color=$shieldColor
##### Remove the line-break between kill and color before compiling
```

```
##### Read-in field for dipoles
fieldmap ASM1 file=$map1
fieldmap ASM2 file=$map2

####################
#  Beam elements
####################

place SHIELD z=$startZ-100 length=10 innerRadius=0 outerRadius=$RIRON*1.1
rename=SheildStart
##### Remove the line-break between outerRadius and rename before compiling

##### Place virtual detector at Production Target location
place MuSEDet z=$startZ+$MuSEDetLength rename=Det0

##### Place virtual detector at start of quad QTA11
place MuSEDet z=-$MuSEDetLength rename=Det0a

##### Define QTA11 parameters
param LDRIFT1=0
param PDRIFT1=$LDRIFT1/2

##### Length magnet in mm
param LQTA1=324

##### Radius aperture in mm
param RQTA1=75.0

##### QTA11 defocuses mu+ in X. So, gradient should be negative
param BQTA1=-0.9854*$scale*$scaleQT
param GradQTA1=$BQTA1/$RQTA1*$kGpmm_to_Tpm

##### Define QTA11 quadrupole magnet
param RIRON=500
genericquad QTA11 fieldLength=$LQTA1 apertureRadius=$RQTA1 gradient=$GradQTA1
ironRadius=$RIRON ironLength=$LQTA1 kill=$killInIron ironColor=$ironColor
```

```
##### Remove the line-break between gradient and ironRadius before compiling

##### Place QTA11 at 162 mm wrt. ProdTarget @ -958 mm. 162+958 mm = 1120 mm
param PQTA1=$LDRIFT1+0.5*$LQTA1
place QTA11 z=$PQTA1

##### Place virtual detector between QTA11 and QTB11
param LDRIFT2=131
place MuSEDet z=$PQTA1+0.5*$LQTA1+0.5*$LDRIFT2+0.5*$MuSEDetLength rename=DetAQTA1

##### Define QTB11 parameters
param LDRIFT2=131
param PDRIFT21=$PQTA1+0.5*$LQTA1+0.5*$LDRIFT2
param LQTB=475
param RQTB=115.0

##### Define field gradient for QTB1. It defocuses mu+ in X
param BQTB1=-1.0894*$scale*$scaleQT
param GradQTB1=$BQTB1/$RQTB*$kGpmm_to_Tpm

##### Define QTB11 quadrupole magnet
genericquad QTB11 gradient=$GradQTB1 fieldLength=$LQTB coilHalfWidth=50 coilRadius=150
poleTipRadius=125 ironRadius=$RIRON ironLength=$LQTB kill=$killInIron ironColor=$ironColor
##### Remove the line-break between coilRadius and poleTipRadius before compiling

##### Place QTB11 at 692.5 mm wrt. ProdTarget @ -958 mm. 692.5+958 mm = 1650.5 mm
param PQTB1=$PDRIFT21+0.5*$LDRIFT2+0.5*$LQTB
place QTB11 z=$PQTB1

##### Place virtual detector between QTB11 and QTB12
param LDRIFT20=110
place MuSEDet z=$PQTB1+0.5*$LQTB+0.5*$LDRIFT20+0.5*$MuSEDetLength rename=DetAQTB1

##### Define QTB12 parameters
param LDRIFT20=110
param PDRIFT22=$PQTB1+0.5*$LQTB+0.5*$LDRIFT20
```

```
##### Define field gradient for QTB12. It focuses mu+ in X
param BQTB2=1.1965*$scale*$scaleQT
param GradBQTB2=$BQTB2/$RQTB*$kGpmm_to_Tpm

##### Define QTB12 quadrupole magnet
genericquad QTB12 gradient=$GradBQTB2 fieldLength=$LQTB coilHalfWidth=50 coilRadius=150
poleTipRadius=125 ironRadius=$RIRON ironLength=$LQTB kill=$killInIron ironColor=$ironColor
##### Remove the line-break between coilRadius and poleTipRadius before compiling

##### Place QTB12 at 1277.5 mm wrt ProdTarget at -958 mm. 1277.5 + 958 mm = 2235.5 mm
param PQTB2=$PDRIFT22+0.5*$LDRIFT20+0.5*$LQTB
place QTB12 z=$PQTB2

##### Place virtual detector after QTB12, close to its end
place MuSEDet z=$PQTB2+0.5*$LQTB+0.5*$MuSEDetLength+500 rename=DetAQTB2

param LDRIFT3=3586
param PDRIFT3=$PQTB2+0.5*$LQTB+0.5*$LDRIFT3
param LDRIFT4=1334
param PDRIFT4=$PDRIFT3+0.5*$LDRIFT3+0.5*$LDRIFT4

place SHIELD rename=SHEILD_A z=$PDRIFT4/2-250 length=$PDRIFT4+2500

##### Place virtual detector before start of dipole ASM11
place MuSEDet z=6384.0-10-0.5*$MuSEDetLength-2 rename=Det1

#*****************************************************************
# Change beam angle to 75 deg and place next set of beam elements
#*****************************************************************

##### Define bending radius, arc, angle parameters
param ASMAngleDeg=75.
param ASMAngleRad=$ASMAngleDeg*pi/180.
param L_center_line_ASM=2.*775.39-20
param ASMRadius=$L_center_line_ASM/$ASMAngleRad

##### Place cornerarc to bend the beamline
```

```
cornerarc z=$PDRIFT4+0.5*$LDRIFT4 angle=$ASMAngleDeg/2. centerRadius=$ASMRadius
radiusCut=$ASMRadius-160
##### Remove the line-break between centerRadius and radiusCut before compiling

param PASM1=$PDRIFT4+0.5*$LDRIFT4+0.5*$L_center_line_ASM
place SHIELD length=950 z=$PASM1 innerRadius=3*$RIRON outerRadius=3.1*$RIRON
initialPhi=-60 finalPhi=60
##### Remove the line-break between outerRadius and initialPhi before compiling

##### Define ASM11 dipole current and place the dipole
### The map is set to 1Tesla so current/intensity gives strength of dipole in Tesla
param BASM1=-0.591271616286*155.0/210.0*$scale*$scaleDipole
place ASM1 z=$PASM1 current=$BASM1
cornerarc z=$PASM1 angle=$ASMAngleDeg/2. centerRadius=$ASMRadius
radiusCut=$ASMRadius-160
##### Remove the line-break between centerRadius and radiusCut before compiling

place SHIELD rename=sheild_bend z=$PDRIFT4+$L_center_line_ASM length=4000
innerRadius=2.0*$RIRON outerRadius=2.1*$RIRON initialPhi=65 finalPhi=295
##### Remove the line-break between length and innerRadius before compiling

param LDRIFT5=1357
param PDRIFT5=$PASM1+0.5*$L_center_line_ASM+0.5*$LDRIFT5
param beginCenter=$PASM1+0.5*$L_center_line_ASM

##### Place virtual detector after ASM11, close to its end
place MuSEDet z=6384.01+$L_center_line_ASM+10+0.5*$MuSEDetLength+100 rename=Det2

##### Define QSL11 parameters
param BQSL11=-1.2731*$scale*$scaleQSL
param GradBQSL11=$BQSL11/$RQSL*$kGpmm_to_Tpm

##### Place QSL11 at 9586.8 mm wrt ProdTarget @ -958 mm. 9586.8+958 mm=10544.8 mm
param PQSL11=$PDRIFT5+0.5*$LDRIFT5+0.5*$LQSL
place QSL rename=QSL11 gradient=$GradBQSL11 z=$PQSL11

##### Define QSL12 parameters
```

```
param LDRIFT6=112
param PDRIFT6=$PQSL11+0.5*$LQSL+0.5*$LDRIFT6
param BQSL12=0.9086*$scale*$scaleQSL
param GradBQSL12=$BQSL12/$RQSL*$kGpmm_to_Tpm

##### Place QSL12 at 10288 mm wrt ProdTarget @ -958 mm. 10288+958mm=11246 mm
param PQSL12=$PDRIFT6+0.5*$LDRIFT6+0.5*$LQSL
place QSL rename=QSL12 gradient=$GradBQSL12 z=$PQSL12

param LDRIFT7=1018-0.5*$MuSEDetLength
param PDRIFT7=$PQSL12+0.5*$LQSL+0.5*$LDRIFT7

##### Place virtual detector at IFP i.e. 11650 mm wrt. ProdTarget @ -958 mm.
place MuSEDet z=11650 rename=Det3

##### Define QSL13 parameters
param LDRIFT8=512
param PDRIFT8=$PDRIFT7+0.5*$MuSEDetLength+0.5*$LDRIFT7
param BQSL13=0.9086*$scale*$scaleQSL
param GradBQSL13=$BQSL13/$RQSL*$kGpmm_to_Tpm

##### Place QSL13 at 12408 mm wrt ProdTarget @ -958 mm. 12408+958mm=13366 mm
param PQSL13=$PDRIFT8+$LDRIFT8+0.5*$LQSL
place QSL rename=QSL13 gradient=$GradBQSL13 z=$PQSL13



##### Define QSL14 parameters
param LDRIFT9=112
param PDRIFT9=$PQSL13+0.5*$LQSL+0.5*$LDRIFT9
param BQSL14=-1.2732*$scale*$scaleQSL
param GradBQSL14=$BQSL14/$RQSL*$kGpmm_to_Tpm

##### Place QSL14 at 13110 mm wrt. ProdTarget @ -958 mm. 13110+958 mm=14068 mm
param PQSL14=$PDRIFT9+0.5*$LDRIFT9+0.5*$LQSL
place QSL rename=QSL14 gradient=$GradBQSL14 z=$PQSL14

param LDRIFT10=1311
```

```
param PDRIFT10=$PQSL14+0.5*$LQSL+0.5*$LDRIFT10

##### Place virtual detector at start of dipole ASM1
param PASM2=$PDRIFT10+0.5*$LDRIFT10+0.5*$L_center_line_ASM
place MuSEDet z=$PASM2-775.39-10-0.5*$MuSEDetLength-2 rename=Det4

#*********************************************************************
# Change beam angle and place next set of beam elements
#*********************************************************************
param endCenter=$PDRIFT10+0.5*$LDRIFT10

place SHIELD rename=SHIELD_B z=($endCenter+$beginCenter)/2.0
length=$endCenter-$beginCenter
##### Remove the line-break between z and length before compiling

##### Place cornerarc to bend the beamline
cornerarc z=$PDRIFT10+0.5*$LDRIFT10 angle=$ASMAngleDeg/2.
centerRadius=$ASMRadius radiusCut=$ASMRadius-160
##### Remove the line-break between angle and centerRadius before compiling

##### Place dipole magnet ASM12
### The map is set to 1T so current/intensity gives strength of dipole in T
param BASM2=-0.591271616286*155.0/210.0*$scale*$scaleDipole
place ASM2 z=$PASM2 current=$BASM2
cornerarc z=$PASM2 angle=$ASMAngleDeg/2. centerRadius=$ASMRadius
radiusCut=$ASMRadius-160
##### Remove the line-break between centerRadius and radiusCut before compiling

##### Place virtual detector at end of ASM12
place MuSEDet z=$PASM2-775.39+$L_center_line_ASM+10+0.5*$MuSEDetLength+2
rename=Det5
##### Remove the line-break between z and rename before compiling

##### Define QSL15 parameters
param LDRIFT11=684
param BQSL15=0.5440*$scale*$scaleQSL
param GradBQSL15=$BQSL15/$RQSL*$kGpmm_to_Tpm
```

```
##### Place QSL15 at 17246.6 mm wrt. ProdTarget @ -958 mm. 17246.6+958mm=18204.6 mm
param PQSL15=$PASM2+0.5*$L_center_line_ASM+$LDRIFT11+0.5*$LQSL
place QSL rename=QSL15 gradient=$GradBQSL15 z=$PQSL15

##### Define QSL16 parameters
param BQSL16=-0.7506*$scale*$scaleQSL
param GradBQSL16=$BQSL16/$RQSL*$kGpmm_to_Tpm
param LDRIFT12=112

##### Place QSL16 at 17948.6 mm wrt. ProdTarget @ -958 mm). 17948.6+958mm=18906.6 mm
param PQSL16=$PQSL15+$LQSL+$LDRIFT12
place QSL rename=QSL16 gradient=$GradBQSL16 z=$PQSL16

##### Define QSL17 parameters
param BQSL17=0.9086*$scale*$scaleQSL
param GradBQSL17=$BQSL17/$RQSL*$kGpmm_to_Tpm
param LDRIFT13=1038

##### Place QSL17 at 19576.6 mm wrt ProdTarget @ -958 mm. 19576.6+958 mm=20534.6 mm
param PQSL17=$PQSL16+$LQSL+$LDRIFT13
place QSL rename=QSL17 gradient=$GradBQSL17 z=$PQSL17

##### Define QSL18 parameters
param BQSL18=-1.2732*$scale*$scaleQSL
param GradBQSL18=$BQSL18/$RQSL*$kGpmm_to_Tpm
param LDRIFT14=163

##### Place QSL18 at 20329.6 mm wrt ProdTarget @ -958 mm. 20329.6+958 mm=21287.6 mm
param PQSL18=$PQSL17+$LQSL+$LDRIFT14
place QSL rename=QSL18 gradient=$GradBQSL18 z=$PQSL18

##### Place virtual detector at PiM1Target
param targetLocation=22159.5
place MuSEDet z=$targetLocation rename=DetTar

##### Place virtual detector at beam hodoscope before PiM1Target.
```

```
place MuSEDet z=$targetLocation-1000 rename=DetBH
place SHIELD rename=SHIELD_TAR z=$targetLocation innerRadius=2*$MuSEDetRadius
outerRadius=2.1*$MuSEDetRadius length=5000
##### Remove the line-break between innerRadius and outerRadius before compiling

##### Place virtual detectors (beam counters) after PiM1Target.
place MuSEDet z=$targetLocation+1500 rename=DetBC1

place MuSEDet z=$targetLocation+2500 rename=DetBC2

##### Write the output file
ntuple partOut detectors=Det* require=DetTar
```

Appendix D
TOF simulation

This detailed write up of the simulation and momentum extraction procedure was originally written by Steffen Strauch and is reproduced here for completeness. Some details are changed to emphasize the parts relevant to this work.

D.1 Simulation Timing

The TOF in the simulation is defined as the time difference between a particle interaction with any paddle in the BH and an interaction with any bar in the BM. Both primary and decay particles are recorded in order to properly include background. As an example we see in Fig. D.1 a simulated electron time-of-flight distributions for the L_1 setup.

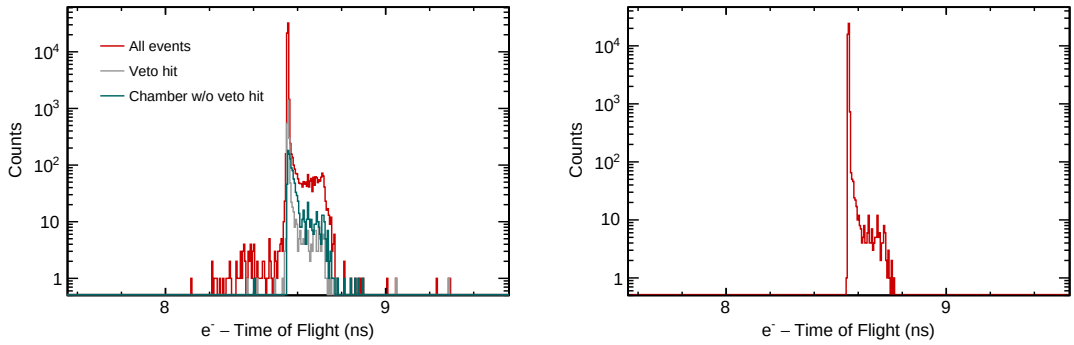

Figure D.1: Simulated electron time-of-flight distributions for the L_1 setup and a nominal channel momentum of 161 MeV/c. TOF is measured from beam hodoscope paddle C7 to beam-monitor paddle 1. ***Left:*** All simulated events (red), the events that interacted with the veto detector (gray), and the events that interacted with the scattering-chamber without leaving a signal in the veto detector (green). ***Right:*** The same distribution after applying the detector-exclusivity and veto-detector cuts. Courtesy of Steffen Strauch.

The nominal channel momentum is 161 MeV/c, and the TOF is measured from beam hodoscope paddle C7 to beam-monitor paddle 1. The red histogram in the left panel shows all simulated events, with the major peak corresponding to the e TOF. The shoulders to either side of the main peak come from background

processes. More precisely events to the right of the main peak come from background in the BM which cause the TOF measurement to stop *later* than if an electron traveled straight down the beam line. Events to the left of main peak come from background events in the BH detector which cause the TOF measurement to start *earlier* than a primary electron. These early processes would correspond to a speed greater than that of c if they were primary particles.

These background events generally come from Bremsstrahlung production followed by Compton scattering, or by δ production in a neighboring bar. The background process to the right of the main electron peak is larger than the background to the left of the peak because the BM detector is physically thicker than the BH detector. An increased thickness allows photons to travel several cm before converting, thus stopping the measurement later than a direct electron.

The gray histogram in Fig. D.1 are all events that hit the VETO detector. The VETO detector is centered around the entrance of the MUSE scattering chamber. Any particle interacting with this detector is not traveling in a straight path down the beam line and is removed from the analysis. We see in the green histogram the events that hit the scattering chamber without causing a signal in the VETO. These events are also discarded. It is important to note that the small difference between the green and gray histograms indicates it is sufficient to cut all events that hit the VETO detector in the analysis in order to suppress the background of particles not traveling straight down the beam line.

Almost all background can be removed by requiring no hits in the VETO detector, and only one hit in each timing detector. This "exclusivity cut" is shown in the right panel of Fig. D.1. This right panel is representative of a typical distribution used in the analysis of the electron TOF data.

Figures D.2 and D.3 show, a simulated muon and pion TOF distribution respectively for the L_1 setup. The dominant TOF peak of the primary particles is wider than in the case of electrons, presumably due to

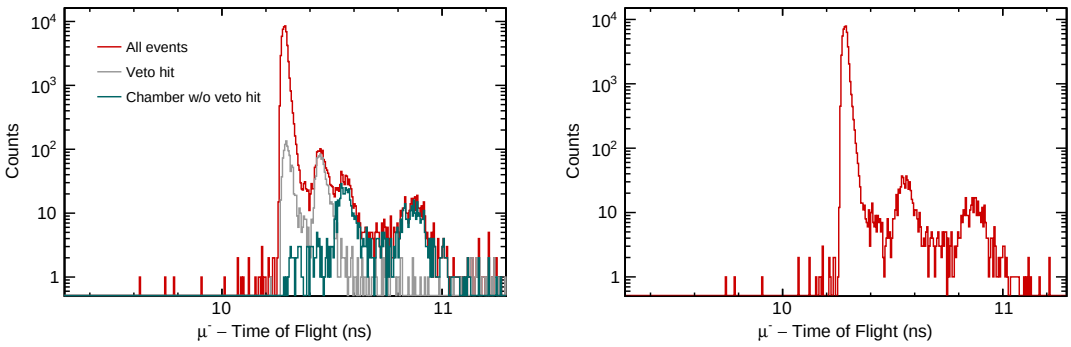

Figure D.2: Same as Fig. D.1 but for muons.

variations in the muon speeds and a lower average speed due to their higher mass. The left panel shows background from muon interactions with the veto detector and scattering chamber. The multiple peaks in the gray and green distributions come from muon decays in flight to electrons at large angles.

Finally, Fig. D.3 shows a simulated pion TOF distribution. The distribution features a broad background from pion decays with the decay muon arriving at the beam monitor. The spectrum otherwise shows qualitatively similar features to the muon distribution.

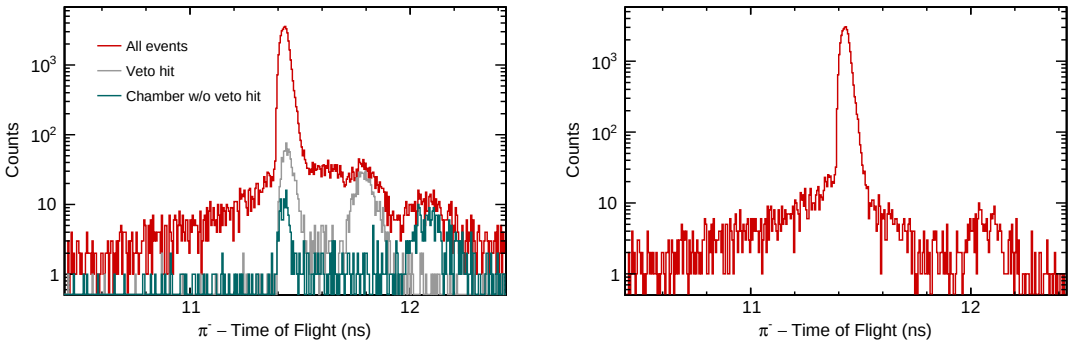

Figure D.3: Same as Fig. D.1 but for pions.

D.2 Simulation Path Length

The path length was determined in the simulation as the distance between the particle hit positions in the initial and final timing detectors, respectively. Fig. D.4 shows the simulated distribution of electron path-lengths in the L_1 setup and with a channel momentum of 161 MeV/c. The start of the red histogram at the left side of the figure corresponds to the minimum distance between the center of each detector ($\Delta L = 2564.4$ mm), it is marked with a dashed line. The dashed line ≈ 0.5 mm to the right of the minimum distance corresponds to the average path length, $\langle L \rangle$, measured in the simulation. The distribution tails off to the right corresponding to the maximum possible distance an electron can travel between one BH paddle and one BM bar without hitting the VETO or scattering chamber. For comparison with data the mean value of the path length is used. The TOF differences are the quantities that enter into the analysis of the simulation and correspondingly path length differences are the relevant quantity here. The difference between mean path length and minimum path length is insignificant.

D.3 Simulation Average speed

We show in Fig. D.5 an example of π TOF determined from the simulation. We fit the distribution with a gaussian and use the peak to estimate the average particle speed. This is similar to the mean value of the histogram if you find the histogram mean near the central peak. Using either value gives consistent results for the momentum. Whichever value we use we also use for extracting the experimentally determined TOF in order to have a similar analysis procedure for both simulation and data. Using such a central value of the peak also reduces the impact of background events in the TOF determination.

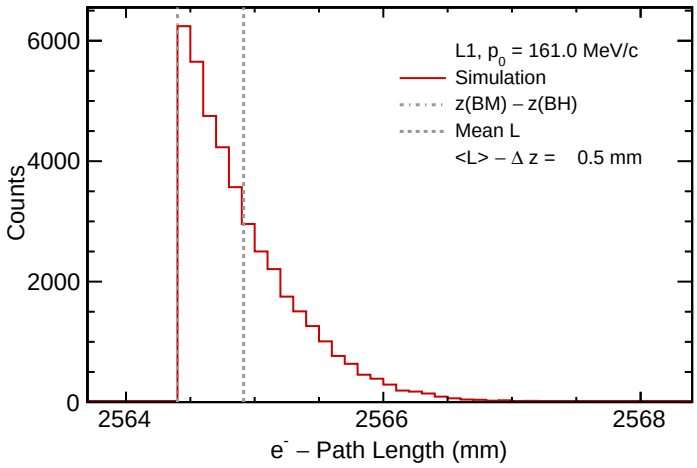

Figure D.4: Example of a simulated path-length distribution for electrons in the L_1 setup and with a channel-momentum of 161 MeV/c. The beam-hodoscope plane C was used for this simulation. Courtesy of Steffen Strauch.

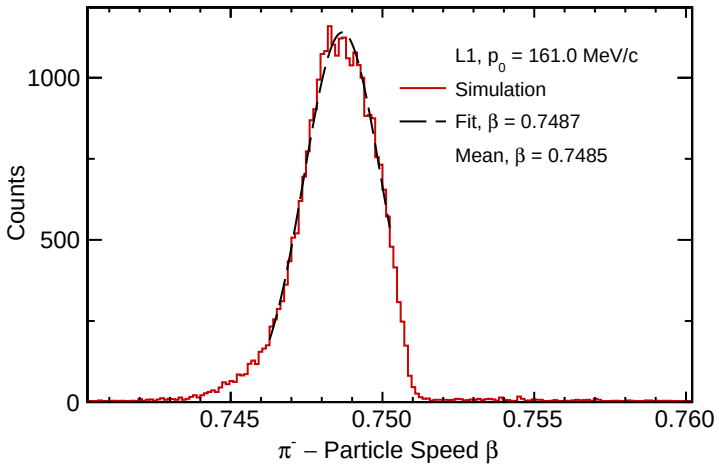

Figure D.5: Example of a simulated speed distribution for pions in the L_1 setup and with a channel-momentum of 161 MeV/c. The beam-hodoscope plane C was used for this simulation. Courtesy of Steffen Strauch.

A simple approximation would be to extract the μ and π TOF by taking the ratio of their time differences with respect to the e time difference as shown below. This works to first order as the e's have a velocity indistinguishable from that of light at all MUSE momenta due to their low mass.

$$\beta^{\mu,\pi} = c\frac{t_i^{\mu,\pi} - t_0^{\mu,\pi}}{t_i^e - t_0^e}. \tag{D.1}$$

D.4 Determination of the actual flight-path differences

The difference of the measured TOF of electrons for two settings is related to the path-length differences of the settings,

$$(t_i^{\rm exp} - \tau) - (t_0^{\rm exp} - \tau) = (L_i^{\rm exp} - L_0^{\rm exp})\,\frac{1}{c}\;;$$

with t_i being the time for a setup L_i and t_0 is the time for the reference setup L_0, and τ being the unknown, constant cable and electronic offset. Similarly for the simulated TOF,

$$t_i^{\rm sim} - t_0^{\rm sim} = \left(L_i^{\rm sim} - L_0^{\rm sim}\right)\frac{1}{c}\;.$$

With $\Delta L_i = L_i - L_0$,

$$\Delta t_i = \left(t_i^{\rm exp} - t_i^{\rm sim}\right) - \left(t_0^{\rm exp} - t_0^{\rm sim}\right) = \left(\Delta L_i^{\rm exp} - \Delta L_i^{\rm sim}\right)\frac{1}{c}.$$

The time differences between the simulated time and measured time for a given detector position are mostly equal to the time offset τ by construction. The difference of these differences, $\Delta t_i = (t_i^{\rm sim} - t_i^{\rm exp}) - (t_0^{\rm sim} - t_0^{\rm exp})$, is generally small. Any deviations from 0 occur due to variations in the μ and π momentum and in the path length assumed in the simulation and the actual path length. If the simulation describes the experiment fully, $\Delta t_i = 0$ for all settings; any differences from 0 is a measure of the quality of the simulation. The value of Δt_i^e, the e TOF is equal to the difference in path length between the experiment and simulation. Again this relation arises as e's have a velocity indistinguishable from that of c for MUSE.

$$\Delta L_i^{\rm exp} - \Delta L_i^{\rm sim} = c\Delta t_i^e\;. \tag{D.2}$$

We have extracted the experimental path-length differences mostly to study systematic effects, for example, the reproducibility of moving the MUSE timing detectors.

D.5 Determination of average particle speeds

The timing mismatch between measured and simulated muon and pion TOF depends on the average speeds β_i of particles for the flight paths L_i given by electrons.

$$c\Delta t_i^{\mu,\pi} = \left(\frac{L_i^{\rm exp}}{\beta_i^{\rm exp}} - \frac{L_0^{\rm exp}}{\beta_0^{\rm exp}}\right) - \left(\frac{L_i^{\rm sim}}{\beta_i^{\rm sim}} - \frac{L_0^{\rm sim}}{\beta_0^{\rm sim}}\right) \tag{D.3}$$

$$= \frac{\Delta L_i^{\rm exp}}{\beta_i^{\rm exp}}\left[1 + \epsilon^{\rm exp}\right] - \frac{\Delta L_i^{\rm sim}}{\beta_i^{\rm sim}}\left[1 + \epsilon^{\rm sim}\right] \tag{D.4}$$

The terms ϵ are given by, $\frac{\Delta L_i}{\beta_i}\left[1 + \frac{L_0}{\Delta L_i}\left\{1 - \frac{\beta_i}{\beta_0}\right\}\right]$ and are at most .005 for the worst case of low-momentum pions. They represent the mismatch between a given path length and its speed. They are approximately equal in our simulations indicating good agreement between simulated and actual path lengths. Ignoring these terms result in an undetectable modification of the time mismatch Δt by a factor $1 - \epsilon$. Given the small value of the terms and the knowledge that they are nearly equal and enter as a difference into our analysis we can use the following approximation:

$$c\Delta t_i^{\mu,\pi} \approx \frac{\Delta L_i^{\rm exp}}{\beta_i^{\rm exp}} - \frac{\Delta L_i^{\rm sim}}{\beta_i^{\rm sim}}. \tag{D.5}$$

This approximation allows us to solve for the experimental particle speeds:

$$\beta_i^{\rm exp} = \frac{\Delta L_i^{\rm exp}}{c\Delta t^{\mu,\pi} + \frac{\Delta L_i^{\rm sim}}{\beta_i^{\rm sim}}} \tag{D.6}$$

$$= \beta_i^{\rm sim} \frac{\Delta L_i^{\rm sim} + c\Delta t_i^e}{\Delta L_i^{\rm sim} + c\beta_i^{\rm sim}\Delta t_i^{\mu,\pi}}. \tag{D.7}$$

Equation (D.7) was used in this analysis with the fitted time mismatches Δt_i and the path length and speed results of the simulation. With the approximation that speed differences between various setups are small, $\beta_i \approx \beta_0$, Eq. (D.7) reduces to Eq. (D.1). While this approximation was not made in the analysis, it shows that the experimental determination of the μ and π speeds is a *relative* time measurement to the e measurements and a comparison with the speed of light.

D.6 Determination of the incident particle momentum

To a good approximation, the average particle momentum can be determined from the average particle speeds $\beta_i^{\rm exp}$. The speed and momentum are related by

$$p = \frac{m_0\beta c^2}{\sqrt{1-\beta^2}}. \tag{D.8}$$

This momentum determination does not give us the initial momentum however, as the particle slows down due to energy loss as it interacts with material in the beam line. MUSE must know the incident momentum of particles in order to know the beam line momentum. To obtain the initial momentum, the particle must have its energy loss corrected along its path. We determine ΔT from the results of our simulation as the difference of the kinetic energy of the incident particle and the kinetic energy of the particle with average speed β_i,

$$\Delta T_i^{\rm sim} = T_0^{\rm sim} - T^{\rm sim}(\beta_i^{\rm sim}) \tag{D.9}$$

The initial particle momentum is then given by the experimentally determined kinetic energy of the particle and the energy-loss correction from the simulation:

$$p_0^{\rm exp} = \sqrt{(T_0^{\rm exp} + m)^2 - m^2} \tag{D.10}$$

with

$$T_0^{\rm exp} = T_i^{\rm exp}(\beta^{\rm exp}) + \Delta T_i^{\rm sim}. \tag{D.11}$$

Typical values of β, ΔT, L_i, and ΔL_i are shown in Table D.1

Setup	L_i (mm)	ΔL_i (mm)	β_π^{117}	β_π^{210}	ΔT_π^{117} (MeV)	ΔT_π^{210} (MeV)
L_0	1884.4	0	0.6240	0.8294	3.53	2.27
L_1	2544.4	660	0.6246	0.8295	3.38	2.22
L_2	2879.4	995	0.6230	0.8292	3.66	2.42
L_3	3539.4	1655	0.6234	0.8293	3.61	2.29

Table D.1: Path-length L_i and path-length-difference ΔL_i relative to the L_0 setting for various configurations of the time-of-flight measurements along with simulation results of average pion speeds and energy losses at 117 and 210 MeV/c channel momentum, respectively. The path-length is given from the beam-hodoscope plane D to the beam monitor. The path-lengths from plane C are 20 mm longer. Courtesy of Steffen Strauch.